Unconventional Propulsive Empennage - Future or Fiction?

Stability & control analysis and the effect of scaling of the DUUC

K. J. M. Hameeteman September 2017

Technische Universiteit Delft

DUUC 0.1
TUDelft

TUDelft Delft University of Technology

Challenge the future

UNCONVENTIONAL PROPULSIVE EMPENNAGE - FUTURE OR FICTION?

STABILITY & CONTROL ANALYSIS AND THE EFFECT OF SCALING OF THE DUUC

by

K. J. M. Hameeteman

in partial fulfillment of the requirements for the degree of

Master of Science
in Aerospace Engineering

at the Delft University of Technology,
to be defended publicly on Monday October 2, 2017 at 03:00 PM.

Supervisor:	ir. R. E. C. van Dijk	TU Delft / ParaPy
Thesis committee:	Prof. dr. ir. L. L. M. Veldhuis,	TU Delft
	Dr. ir. M. Voskuijl,	TU Delft
	Dr. R. P. Dwight,	TU Delft

An electronic version of this thesis is available at `http://repository.tudelft.nl/`.

Thesis Registration Number: 161#17#MT#FPP

Delft
University of
Technology

PREFACE

Throughout my final year as a Master student at the Delft University of Technology, there are a number of people that I met who deserve some credit. Due to a shortage of faculty staff members before I started my MSc research, I had been looking for over three months for a challenging project that would fit my field of interests. Eventually, the TU Delft asked my supervisor Reinier van Dijk to assist graduates and he accepted the job while not even being employed at the university. Reinier is a busy man but our meetings were always very effective and he guided me by providing honest feedback. I would also like to thank Leo Veldhuis, Mark Voskuijl, and Richard Dwight for being part of my assessment committee.

Furthermore I would like to thank my parents, brother and his girlfriend for showing interest in my work and supporting me throughout the process by means of advising whenever I needed it. Last but definitely not least, I want to express my appreciation to my friends with whom I spent many many hours of brainstorming and discussing, which helped me a lot in putting together this thesis.

K. J. M. Hameeteman
Delft, September 2017

Cover image is a snapshot of the video introducing the DUUC, available on YouTube: `https://www.youtube.com/watch?v=VDbJBkcQBPI`

ABSTRACT

Flight testing is an activity that exists since the beginning of flight, and is still seen as an essential part of the aircraft development process. While numerical simulation has been improved significantly over the last decade, flight testing remains attractive in the exploration and evaluation of the flight envelope, especially in the region where numerical simulation lacks prediction accuracy. Free-flying model testing is a potential technique, which is recognized by some of the largest research institutes. Using such relatively cheap scale models aids in the determination of the flight behavior of full-scale aircraft in an early stage in the design process. Furthermore it takes less time to develop a scale model and is also safer to fly.

A 5.5% scale model of the Boeing 737-700 is created by the TU Delft as a first step towards investigating the potential of dynamically scaled flight testing. This Delft University Unconventional Concept (DUUC) has a conventional tube-wing configuration and features ducted fan engines mounted aft on the fuselage, which replace the conventional empennage. A horizontal and vertical jet vane is placed in the duct, which guide the propeller slipstream and thereby control the attitude of the aircraft. Successful flights have already been performed with this model, which proves the propulsive empennage concept. However, the stability and control behavior has only been assessed at a low level. Flow characteristics entailed by the ducted fan are accounted for by means of approximate functions and empirical relations instead of looking at the physical interaction between the components within the duct. This study focusses on the processing of said interaction by performing a CFD study of which the results are used in the longitudinal equations of motion of the DUUC. This way, certain motion can be simulated from which the effect of the unconventional empennage on the stability and control can be assessed.

In order to study the aerodynamics of the propulsive empennage and subsequently its stability, a CAD model is developed using PARAPY. This is a knowledge based engineering platform written in the Python language and allows for parametrization of the model such that geometric alterations can easily be implemented. Previous studies within the TU Delft have lead to a multi-model generator written in PARAPY. The fuselage and wing generation modules that were developed can readily be applied in the generation of the DUUC model. The propulsive empennage module is created by the author of this thesis, consisting of several sub-parts: (1) outer duct that forms a shielding around the propeller, (2) the pylon that connects the duct to the fuselage, (3) a center body to which the (4) propeller and (5) control vanes are attached.

The full aircraft model has been used in a series of CFD simulations with ANSYS FLUENT. Inviscid steady calculations are performed using a pressure-based solver with a SIMPLE pressure-velocity coupling scheme. The propeller is modeled as an actuator disk whereby the thrust is defined by specifying a pressure jump across the thin surface. The thrust produced by the ducted fan is based on the turboprop installed on the ATR72-600 aircraft, which has similar dimensions compared to the Boeing 737-700. Both the full-scale DUUC as well as the 5.5% scale model are subjected to this aerodynamic analysis. Minor discrepancies were found between the two models, which is a result of the *artificial viscosity* that is implemented in the Euler scheme to smoothen strong gradients in the solution (numerical dissipation).

Due to the location of the engine, the thrust line is located above the center of gravity which contributes to a stabilizing effect. The effect of several parameters on the stability and control has been analysed, such as the center of gravity location, mass and inertia, and geometric scaling factor. The slight difference in aerodynamic performance between the full-scale and subscale models, means that the trimmed solution for steady horizontal flight is also slightly different with a maximum error of 2.5 degrees in elevator deflection. More drag is obtained as the aircraft scale goes down, resulting in a higher required thrust to achieve force balance in a trimmed flight condition. Furthermore it is found that by scaling the aircraft down according to Froude scaling theory, the response becomes much faster. This response can in turn be scaled back, which proved to be a very useful estimate of the full-scale simulation.

CONTENTS

List of Figures **xi**

List of Tables **xiii**

Nomenclature **xv**

1 Introduction **1**

2 Background and Scope of Research **3**
- 2.1 Dynamically Scaled Flight Testing. 3
  - 2.1.1 State-of-the-art Research in Dynamic Scaled Model Testing 3
  - 2.1.2 Similitude Requirements. 5
- 2.2 Research Scope 6
  - 2.2.1 DUUC Model 6
  - 2.2.2 Research Question and Objectives 6

3 Parametric Modeling of the DUUC **9**
- 3.1 Multi-Model Generator 9
  - 3.1.1 Parametric Modeling Software PARAPY. 10
  - 3.1.2 Why KBE and PARAPY in This Research? 10
- 3.2 PARAPY Model of the DUUC 11
  - 3.2.1 Fuselage Generation 11
  - 3.2.2 Wing Generation. 13
  - 3.2.3 Ducted Fan Generation 15

4 Aerodynamic Analysis **19**
- 4.1 Geometry Definition 19
- 4.2 Mesh Generation 21
  - 4.2.1 Meshing the DUUC 21
  - 4.2.2 Mesh Convergence Study 21
- 4.3 Solver Setup. 26
  - 4.3.1 Solver Type. 27
  - 4.3.2 Boundary Conditions 27
  - 4.3.3 Solution Settings 29
- 4.4 Aerodynamic Results 30
  - 4.4.1 Convergence Criteria 30
  - 4.4.2 Full-scale Aerodynamic Coefficients 31
  - 4.4.3 Subscale Aerodynamic Coefficients 35
  - 4.4.4 Effect of Thrust on Aerodynamics 40

5 Flight Mechanics Simulation **43**
- 5.1 Incorporation of the CFD Results in PHALANX. 43
- 5.2 Weight and Balance Estimation 45
  - 5.2.1 Mass Moment of Inertia 45
  - 5.2.2 Center of Gravity and Neutral Point Location 45
- 5.3 Stability & Control Methodology 46
  - 5.3.1 Trim & Linearization 47
  - 5.3.2 Longitudinal Handling Qualities 48
- 5.4 Effect of Center of Gravity Location on Flight Mechanics 49
  - 5.4.1 Effect of CG Location on the Trim Solution. 49
  - 5.4.2 Effect of CG Location on the Longitudinal Static Stability 50
  - 5.4.3 Effect of CG Location on the Longitudinal Eigenvalues 51
  - 5.4.4 Effect of CG Location on the Take-off Rotation 51

5.5 Effect of Inertia on Flight Mechanics . . . 52
  5.5.1 Effect of Inertia on the Trim Solution . . . 52
  5.5.2 Effect of Inertia on the Longitudinal Static Stability . . . 53
  5.5.3 Effect of Inertia on the Longitudinal Eigenvalues . . . 53
  5.5.4 Effect of Inertia on the Take-off Rotation . . . 54
5.6 Effect of Aircraft Scaling on Flight Mechanics . . . 55
  5.6.1 Effect of Aircraft Scaling on the Neutral Point Location . . . 55
  5.6.2 Effect of Aircraft Scaling on the Trim Solution . . . 55
  5.6.3 Effect of Aircraft Scaling on the Longitudinal Static Stability . . . 55
  5.6.4 Effect of Aircraft Scaling on the Longitudinal Eigenvalues . . . 56
  5.6.5 Effect of Aircraft Scaling on the Take-off Rotation . . . 58
5.7 Skin Friction Drag Correction Sensitivity . . . 58
5.8 Stability & Control Analysis of the DUUC . . . 60
  5.8.1 Trim solution . . . 60
  5.8.2 Longitudinal Stability . . . 61
  5.8.3 Longitudinal Eigenmodes . . . 62
  5.8.4 Maximum Instantaneous Pitch Acceleration . . . 64
  5.8.5 Pitch Control Power . . . 65
  5.8.6 Time-Response to Control Inputs . . . 66

6 Conclusions and Recommendations **69**
6.1 Conclusions . . . 69
6.2 Recommendations . . . 72

Bibliography **73**

A Images of Relevant Projects **75**

B Derivation of Scaling Factors **79**
B.1 Geometric Scaling Laws . . . 79
B.2 Inertia Scaling Laws . . . 79
  B.2.1 Fluid Density . . . 79
  B.2.2 Mass . . . 79
  B.2.3 Mass Moment of Inertia . . . 80
B.3 Froude Scaling . . . 80
  B.3.1 Velocity . . . 80
  B.3.2 Mach Number . . . 80
  B.3.3 Dynamic Pressure . . . 80
  B.3.4 Reynolds Number . . . 81
  B.3.5 Time . . . 81
  B.3.6 Lift, Drag, and Moment Coefficients . . . 81
B.4 Mach Scaling . . . 82
  B.4.1 Velocity . . . 82
  B.4.2 Dynamic Pressure . . . 82
  B.4.3 Froude Number . . . 82
  B.4.4 Reynolds Number . . . 82
  B.4.5 Time . . . 82
  B.4.6 Lift, Drag, and Moment Coefficients . . . 82
B.5 Reynolds Scaling . . . 83
  B.5.1 Velocity . . . 83
  B.5.2 Mach . . . 83
  B.5.3 Dynamic Pressure . . . 83
  B.5.4 Froude Number . . . 83
  B.5.5 Time . . . 83
  B.5.6 Lift, Drag, and Moment Coefficients . . . 84

C Cluster Setup **85**

D Meshing Terminology **87**
D.1 General 87
D.2 Mesh Quality 88
D.3 Boundary Layer Modeling. 91

E Sizes and Results of the Meshes Used in Mesh Convergence Study **93**
E.1 Full-scale 93
E.2 Subscale 94

LIST OF FIGURES

2.1 Example of dynamic (geometry + inertia) similarity of matryoshka dolls 3
2.2 Delft University Unconventional Configuration - DUUC 6

3.1 High Level Primitives approach of the MMG 9
3.2 The geometric kernel of ParaPy which makes use of Python and OpenCascade 10
3.3 Generation of the fuselage object in PARAPY 12
3.4 Steps in generating the wing part in the MMG 13
3.5 PARAPY model of the tube-wing configuration of the DUUC 14
3.6 Steps in generating the leading and trailing edge rails in the MMG 15
3.7 Definition of the parameters describing the positioning and shape of the ducted fan geometry . 16
3.8 Steps in generating the ducted fan part in PARAPY 18

4.1 ANSYS FLUENT project schematic 19
4.2 DUUC model imported in the ANSYS DesignModeler 20
4.3 Outer fluid domain around the aircraft body and inner fluid domain around the duct 20
4.4 Side view of the DUUC mesh 21
4.5 Mesh on the duct cross-section 22
4.6 Lift coefficient as function of mesh density for the full-scale simulation, showing mesh convergence 23
4.7 Pressure drag coefficient as function of mesh density for the full-scale simulation, showing mesh convergence 24
4.8 Lift coefficient as function of mesh density for the subscale simulation, showing mesh convergence 25
4.9 Pressure drag coefficient as function of mesh density for the subscale simulation, showing mesh convergence 26
4.10 Mesh quality of the full-scale DUUC mesh 27
4.11 Mesh quality of the subscale DUUC mesh 27
4.12 Boundary conditions of the fluid domain 28
4.13 Altitude performance of the F568-1 propeller 29
4.14 Convergence history of the FLUENT calculations for the DUUC at $V_\infty = 77\ m/s$, $\alpha = 3°$ and $\delta_h = 0°$ 31
4.15 Convergence history of the FLUENT calculations for the subscale DUUC at $V_\infty = 18\ m/s$, $\alpha = 3°$ and $\delta_h = 0°$ 31
4.16 Streamlines and pressure contour within the duct at $y = -5$ m for (left) $\alpha = 9°$ and (right) $\alpha = -9°$ 32
4.17 Effect of elevator deflection on the lift coefficient of each component of the full-scale DUUC . . 33
4.18 Effect of elevator deflection on the drag coefficient of each component of the full-scale DUUC . 35
4.19 Effect of elevator deflection on the moment coefficients of the wing, fuselage, and tail of the full-scale DUUC 36
4.20 Velocity contour around the horizontal vane at $\alpha = 6°$ and $\delta_h = 6°$ 37
4.21 Effect of elevator deflection on the lift coefficient of each component of the subscale DUUC . . 38
4.22 Effect of elevator deflection on the drag coefficient of each component of the subscale DUUC . 39
4.23 Effect of elevator deflection on the moment coefficients of the wing, fuselage, and tail of the subscale DUUC 40
4.24 Effect of thrust on the lift coefficient of each component 41
4.25 Effect of thrust on the drag coefficient of each component 42

5.1 Schematic view of the body and its reference axis systems in PHALANX 43
5.2 Free body diagram of the DUUC with the reference coordinate systems used in PHALANX . . . 46
5.3 Body reference frame with respect to the Earth reference frame 47
5.4 Top level structure of the flight mechanics model in PHALANX 48

5.5 Effect of the CG location on the trim solution . . . 49
5.6 Effect of the CG location on the static stability at $V = 80\ m/s$ . . . 50
5.7 Longitudinal eigenvalues for various CG locations at $V = 80\ m/s$ . . . 51
5.8 Effect of the CG location on the instantaneous pitch acceleration at $V = 80\ m/s$ . . . 52
5.9 Effect of mass and inertia on the trim solution . . . 53
5.10 Effect of mass and inertia on the static stability at $V = 80\ m/s$ . . . 53
5.11 Longitudinal eigenvalues for various mass scales at $V = 80\ m/s$ . . . 54
5.12 Effect of mass and inertia on the instantaneous pitch acceleration at $V = 80\ m/s$ . . . 54
5.13 Effect of aircraft scaling on the neutral point location . . . 55
5.14 Effect of aircraft scaling on the trim solution . . . 56
5.15 Effect of aircraft scaling on the static stability at $V_f = 80\ m/s$ and $SM = 0.10$ . . . 56
5.16 Longitudinal eigenvalues for various scale factors at $V_f = 80\ m/s$ . . . 57
5.17 Short period frequency as function of scaling factor at $V_f = 80\ m/s$ . . . 57
5.18 Phugoid frequency as function of scaling factor at $V_f = 80\ m/s$ . . . 58
5.19 Effect of aircraft scaling on the instantaneous pitch acceleration at $V_f = 80\ m/s$ . . . 58
5.20 Sensitivity of the skin friction drag correction on the trim solution . . . 59
5.21 Sensitivity of the skin friction drag correction on the trim thrust coefficient . . . 59
5.22 Longitudinal eigenvalues for various skin friction drag correction factors at $V = 80\ m/s$ with $SM = 0.10$ . . . 60
5.23 Trim solution for the full-scale DUUC with $SM = 0.10$ . . . 61
5.24 Trim solution for the 5.5% scaled DUUC with $SM = 0.10$ . . . 61
5.25 Comparison of the response to a 1 degree disturbance in AoA, between the full-scale and sub-scale DUUC at $V_f = 80\ m/s$ with $SM = 0.10$ . . . 62
5.26 Required elevator deflection for different push-over and pull-up load factors at various flight speeds with $SM = 0.10$ . . . 63
5.27 Comparison between the full-scale and subscale phugoid motion at $V_f = 80 m/s$ with $SM = 0.10$ 63
5.28 Short period response of the full-scale and subscale DUUC at $V_f = 80 m/s$ with $SM = 0.10$ . . . 64
5.29 Control Anticipation Parameter of the full-scale and subscale DUUC at $V_f = 80\ m/s$ with $SM = 0.10$ . . . 64
5.30 Take-off rotation of the full-scale and subscale DUUC at $V_f = 80\ m/s$ with $SM = 0.10$ . . . 65
5.31 Elevator control power as function of airspeed with $SM = 0.10$ . . . 65
5.32 Elevator following a 2-3-1-1 control input with an amplitude of 5° . . . 66
5.33 DUUC response to a 5 degree 2-3-1-1 elevator input at $V_f = 80\ m/s$ with $SM = 0.10$ . . . 67
5.34 DUUC response to a 2-3-1-1 single engine thrust of 1 kN input at $V_f = 80\ m/s$ with $SM = 0.10$. 68

C.1 Example input file to be invoked by ANSYS Fluent . . . 86
C.2 Example .pbs file that instructs the HPC12 to execute ANSYS Fluent . . . 86

D.1 Typical 3D mesh elements . . . 87
D.2 Structured mesh around a 2D airfoil . . . 88
D.3 Unstructured mesh around a 2D supercritical airfoil . . . 88
D.4 Hybrid mesh consisting of quadrilateral elements in the boundary layer area and triangular elements which extend the mesh into the far field . . . 88
D.5 Optimum equilateral cell geometry . . . 90
D.6 Definition of the vectors used to measure cell orthogonality . . . 90
D.7 Different layers in the turbulent boundary layer . . . 91
D.8 Different layers in the turbulent boundary layer . . . 92
D.9 Skin friction coefficient as function of Reynolds number . . . 92

LIST OF TABLES

2.1 Relevant projects in the field of dynamically scaled flight testing . . . 4
2.2 Scaling factors for Froude, Mach, and Reynolds scaling . . . 5

3.1 Input parameters for the ducted fan module . . . 17

4.1 Number of elements in the full-scale meshes that are used in the mesh convergence study . . . 22
4.2 Number of elements in the subscale meshes that are used in the mesh convergence study . . . 25
4.3 Mesh quality metrics (average) of the full-scale mesh convergence study . . . 25
4.4 Mesh quality metrics (average) of the subscale mesh convergence study . . . 27
4.5 Spatial discretization settings used in ANSYS FLUENT . . . 29
4.6 Under-relaxation factors used in ANSYS FLUENT . . . 30

5.1 Reference areas used for the calculation of each component skin friction coefficient . . . 45
5.2 Mass data and inertia estimation of the full-scale DUUC . . . 45
5.3 Center of gravity and neutral point locations of the subscale and full-scale models (see Figure 5.2 for sign convention) . . . 46

C.1 Delft University of Technology cluster specifications for the different nodes . . . 85

D.1 Mesh quality considerations . . . 89
D.2 Constant value of C used for the element quality metric . . . 90

E.1 Mesh sizing settings used for the mesh convergence study (all units are in m) . . . 93
E.2 Mesh constants used for the mesh convergence study . . . 94
E.3 Reference areas used in the mesh convergence study . . . 94
E.4 Lift coefficients for different mesh densities . . . 94
E.5 Pressure drag coefficients for different mesh densities . . . 94
E.6 Mesh sizing settings used for the mesh convergence study of the subscale model (all units are in mm) . . . 95
E.7 Lift coefficients for different mesh densities of the subscale model . . . 95
E.8 Pressure drag coefficients for different mesh densities of the subscale model . . . 95

NOMENCLATURE

ACRONYMS

AirSTAR	Airborn Subscale Transport Aircraft Reserach
AoA	Angle of Attack
BWB	Blended Wing Body
CAD	Computer-Aided Design
CAP	Control Anticipation Parameter
CFD	Computational Fluid Dynamics
CG	Center of Gravity
CST	Class-Shape Transformation
DES	Detached-Eddy Simulation
DUUC	Delft University Unconventional Concept
FM	Fuel Mass
GUI	Graphical User Interface
HLP	High Level Primitives
IEP	Innovative Evaluation Platform
JWSC	Joined Wing SensorCraft
KBE	Knowledge Based Engineering
LE	Leading Edge
LOC	Loss Of Control
LTH	Luftfahrttechnisches Handbuch
LTI	Linear Time-Invariant
MAC	Mean Aerodynamic Chord
MMG	Multi-Model Generator
MTOM	Maximum Take-Off Mass
MUTT	Multi-Utility Technology Testbed
NACRE	New Aircraft Concept REsearch
NASA	National Aeronautics and Space Administration
NLR	Nederlands Lucht- en Ruimtevaartcentrum
NOVAIR	Novel Aircraft Configurations and Scaled Flight Testing Instrumentation
OEM	Operating Empty Mass
PHALANX	Performance, Handling Qualities and Load Analysis Toolbox
PTERA	Prototype Technology Evaluation and Research Aircraft
RANS	Reynolds-Averaged Navier-Stokes
SM	Static Margin
SMARD	Scale Model Aircraft Research & Development
TE	Trailing Edge
UAV	Unmanned Aerial Vehicle
UPRT	Upset Prevention and Recovery Training
VSAERO	Vortex Separation AEROdynamics

SYMBOLS

LATIN

A	Area	$[m^2]$
a	Speed of sound	$[m/s]$
b	Wing span	$[m]$
C_D	Drag coefficient	$[-]$
C_f	Skin friction coefficient	$[-]$
C_L	Lift coefficient	$[-]$
C_M	Moment coefficient	$[-]$
C_T	Thrust coefficient	$[-]$
c	Chord length	$[m]$
cb_{loc}	Location of the control vane on the center body (0-1)	$[-]$
d	Diameter	$[m]$
FF	Form factor	$[-]$
F	Force	$[N]$
f	Fineness ratio	$[-]$
g	Gravitational acceleration	$[m/s^2]$
I	Mass moment of inertia	$[kgm^2]$
J	Advance ratio	$[-]$
l	(Characteristic) length	$[m]$
M	Mach number	$[-]$
M	Moment	$[Nm]$
m	Mass	$[kg]$
$mScale$	Mass scale factor	$[-]$
N	Geometric scaling factor	$[-]$
N	Number of mesh elements	$[-]$
n	Normal load factor	$[-]$
p	Pressure	$[N/m^2]$
p, q, r	Roll, pitch and yaw rate	$[deg/s]$
$\dot{q}$	Pitch acceleration	$[deg/s^2]$
q	Dynamic pressure	$[N/m^2]$
r	Radius	$[m]$
R_{V_s}	Speed of sound ratio between model and prototype	$[-]$
Re	Reynolds number	$[-]$
S	Surface area	$[m^2]$
SM	Static margin	$[-]$
T	Static temperature	$[K]$
T	Thrust	$[N]$
T_0	Total temperature	$[K]$
T_2	Time to double the amplitude	$[s]$
t	Time	$[s]$
t	Thickness	$[m]$
U^+	Non-dimensional velocity in boundary layer	$[-]$
u	Velocity in body x-direction	$[m/s]$
V	Velocity	$[m/s]$
W	Weight	$[N]$
w	Velocity in body z-direction	$[m/s]$
y^+	Non-dimensional wall distance	$[-]$

GREEK

α	Angle of attack	$[deg]$
μ	Dynamic viscosity	$[Ns/m^2]$
ρ	Fluid density	$[kg/m^3]$
σ	Fluid density ratio	$[-]$
θ	Pitch angle	$[deg]$
γ	Isentropic expansion factor	$[-]$
γ	Flight path angle	$[deg]$
ϕ	Cant angle	$[deg]$
δ	Vane deflection angle	$[deg]$
ν	Kinematic viscosity	$[m^2/s]$
ω	Frequency	$[rad/s]$
ζ	Damping ratio	$[-]$
λ	Eigenvalue	$[-]$
ϕ	Roll angle	$[deg]$
ψ	Yaw angle	$[deg]$
τ_w	Wall shear stress	$[N/m^2]$

1

INTRODUCTION

Flight testing is an activity that exists since the beginning of flight, and is still seen as an essential part of the aircraft development process. While numerical simulation has been improved significantly over the last decade, flight testing remains attractive in the exploration and evaluation of the flight envelope, especially in the region where numerical simulation lacks prediction accuracy. The two categories that can be distinguished are *subscale* and *full-scale* flight testing. Where scaled models are limited to static testing in wind tunnels to evaluate the aerodynamic characteristics of the aircraft, dynamic free-flying models are introduced to include the investigation of vehicle motions. Dynamically scaled models have been studied by NASA (and its predecessor NACA) for over 50 years as stated by Chambers[1]. Motivation for the use of subscale models in aircraft development programmes is mainly to reduce cost and time while improving on safety. The role of a subscale model is to predict the flight behavior of a full-scale aircraft as close as possible, without the need of an expensive large prototype. More recent studies also recognize the attractiveness of the technique. An example described by Jordan and Bailey[2] is the development of the Airborn Subscale Transport Aircraft Research (AirSTAR) testbed, which aids in the research to loss-of-control (LOC) accident prevention. Another project is the Prototype-Technology Evaluation and Research Aircraft (PTERA[3]), which is a remotely controlled modular testbed that allows for cost-effective configuration testing.

Above described attractiveness lead to the NOVAIR project (among others), in which NLR and the TU Delft collaborate in researching the potential of the Delft University Unconventional Concept (DUUC). This vehicle has a conventional tube-wing configuration, and features ducted fan engines mounted aft on the fuselage that replace the empennage. A 5.5% scale model has already been built and flown successfully, however no in-depth stability and control analysis has been performed yet.

One of the biggest challenges that comes with scaling is the discrepancy of the Reynolds number with respect to the full-scale counterpart aircraft. Due to this much lower Reynolds number, aerodynamic performance is wrongly estimated. This can for example result in an ambitious lift coefficient prediction, which in reality may never be achieved and even at a different angle of attack. Furthermore, remotely controlling of a scaled aircraft may not be straightforward because of the much faster response time and angular motions with respect to the larger aircraft. This requires sufficient piloting effort as well as a careful selection of control actuators that can deal with such rapid motions, especially in small scale aircraft.

The purpose of this report is to present the author's MSc research, regarding the stability and control behavior of the DUUC. This is studied on both subscale and full-scale levels, which forms a basis for near-future flight test planning and the potential of dynamically scaled flight testing. The longitudinal flying qualities of this aircraft are assessed using the flight mechanics toolbox PHALANX. A priory to this simulation, a parametric model of the DUUC is created in the Knowledge Based Engineering (KBE) platform PARAPY. Aerodynamic analysis is performed with the high-fidelity CFD software ANSYS FLUENT, using an inviscid Euler solver.

A brief history of dynamically scaled flight testing is given in Chapter 2 along with the research scope. A geometric model of the DUUC is created and parametrized using PARAPY as will be discussed in Chapter 3. Chapter 4 describes the aerodynamic analysis procedure and results. This data can then be incorporated in PHALANX to eventually be able to assess the flying qualities of the DUUC, as is clarified in Chapter 5. Furthermore, concluding remarks and future recommendations can be found in Chapter 6.

2

BACKGROUND AND SCOPE OF RESEARCH

In this chapter, the concept of dynamically scaled flight testing is introduced along with the similitude requirements that are involved with aircraft scaling. Furthermore a description of the DUUC is provided, which is the focus of this research. Hereafter, the research question and objectives are discussed.

2.1. DYNAMICALLY SCALED FLIGHT TESTING

In order to gain knowledge of how a full-scale aircraft would perform when it actually flies, prediction methods such as simulations and model testing (free-flight as well as wind tunnel) can be performed. These methods have continuously been improved in order to enhance the accuracy of the predictions. Aircraft models can undergo *static* and *dynamic* testing. Static models are nowadays frequently used in aerodynamic data gathering by means of analyzing the model in wind tunnels. A generally new concept of predicting the flight dynamic behavior in an early stage in the design process is the use of *dynamically scaled* flight models. The principle of a geometrically scaled model is pretty straightforward as it describes a purely linear scaling in all three dimensions. Matryoshka dolls are a traditional Russian example of this geometric scaling. However, imagine one of the inner dolls to be manufactured out of two different materials making the ratio between the top half and bottom half different than the previous doll. In this case both dolls are geometrically similar, though the distributions of mass differ. A dynamically scaled model is not only geometrically scaled, but also inertially, which means that the mass distribution is similar. Therefore it is not only necessary to create a scaled aircraft that fits in its full-scale prototype like a set of matryoshka dolls, but also to consider the internal layout of the model (Figure 2.1). Similitude requirements that ensure dynamic similarity between model and aircraft are treated in detail in Section 2.1.2.

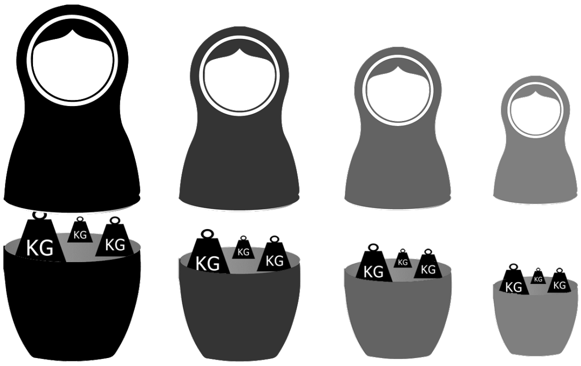

Figure 2.1: Example of dynamic (geometry + inertia) similarity of matryoshka dolls

2.1.1. STATE-OF-THE-ART RESEARCH IN DYNAMIC SCALED MODEL TESTING

Research with dynamically scaled models has been conducted by various institutions throughout the last century, of which NASA is the leading organization with approximately 90 years of experience. A historic evolution of the application of scale models is extensively described by Chambers[1]. Europe is also gaining ground in this research area the last decade as the technique becomes more and more attractive. In early 2015, the Nederlands Lucht- en Ruimtevaartcentrum (NLR) started an interesting programme called Scale Model Aircraft Research & Development (SMARD). The goal of this project is to investigate to what extent the data obtained from scaled flight tests can be mapped onto full-scale test results. NLR has conducted a brief literature study themselves to the recent and current developments in scaled flight testing. The NACRE, X-48, PTERA, AirSTAR, and Demon projects that can be seen at the top side of Table 2.1 are already mentioned by Eveleens and Bremmers[4].

Projects[†]		NACRE 	X-48 	PTERA 	AirSTAR 	Demon 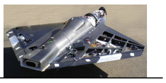
Timeframe		2005-2010	2007-2013	2013-now	2005-now	2005-2011
MTOM [kg]		145	225	100	23	90
Span [m]		4	6.1	4	2	2.5
Scale factor [%]		-	8.5	11	5.5	-
Number of flights		0	120+	several	58+	2 campaigns
Goals	Dynamically scaled	X	X	X	X	
	Modular config.	X		X		
	New a/c concepts	X	X	possible		X
	UPRT	possible	possible	X	X	possible
	Tech. demonstrator			X		X

Projects		SMARD 	Raven 	Midjet 	MUTT 	JWSC 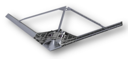
Timeframe		2015-now	2007-2008	2013-now	2009-now	2009-now
MTOM [kg]		150	10.42	9	218	93
Span [m]		4	2	1.9	8.5	5
Scale factor [%]		25	14	36	15	11.1
Number of flights		0	0	several	several	several
Goals	Dynamically scaled	X	X	X		
	Modular config.				X	X
	New a/c concepts		X		X	X
	UPRT	possible				
	Tech. demonstrator					

[†] Consult Appendix A for large images and corresponding sources

Table 2.1: Relevant projects in the field of dynamically scaled flight testing

The New Aircraft Concept REsearch (NACRE[5]) is a project in which a dynamically scaled flying testbed is used to study new aircraft concepts. This testbed is called the Innovative Evaluation Platform (IEP), which has as research focus the investigation of: high-lift devices, flight dynamics, recovery from hazardous flight conditions, noise assessment, wake vortices, and laminar flow. Boeing's BWB project, the X-48[6], is an example of how dynamically scaled flight testing can be used in radical aircraft design. With over 120 flight tests, it is probably the most extensive research in this area. A still ongoing NASA funded project is the Prototype-Technology Evaluation and Research Aircraft (PTERA[3]). It is similar to the IEP in terms of research goals. Another NASA project is the Airborne Subscale Transport Aircraft Research (AirSTAR[2]). It focuses on the improvement of safety in aviation. The last programma described by NLR is the Demon[7] demonstrator, which is a flapless UAV with a diamond-shaped wing. Besides these five projects in Table 2.1, SMARD is included as well as two interesting projects performed at the Linköping University in Sweden namely the business jet, Raven[8], and the aerobatics sports jet, Midjet[9]. Both aircraft are designed and built by students and the goal is primarily educational. While the Raven project is currently on a standstill and waiting for its return, the development of Midjet is thriving and more publications are to follow. The X-56A Multi-Utility Technology Testbed (MUTT[10]) is an aeroservoelastic high-aspect-ratio concept programme conducted by NASA. Related to this programme is the Joined Wing SensorCraft (JWSC[11]), that makes use of a similar high-aspect-ratio wing in a closed box-wing configuration.

Table 2.1 shows that most of the programmes are started throughout the first decade of the 21st century, which confirms the current interest in this field of innovation. Mutual research goals are present such as the capability to easily adjust the model by means of a *modular configuration*. Since some of the projects focus on the research on *new aircraft concepts*, it also shows the potential to aid in the design process of radical aircraft design. The opportunity of risk reduction and LOC event investigations have already been mentioned and some programmes use dynamically scaled models to this extent. They should make it easier to assess *upset prevention and recovery training* (UPRT) techniques and therefore pilots can be trained in a better way to cope with LOC events. Finally the possibility of a *technology demonstrator* is assessed.

2.1.2. SIMILITUDE REQUIREMENTS

Ideally, the aerodynamics of the scale model are similar to the ones of the full-scale aircraft in terms of coefficients. The key parameters that play a role in aerodynamic similarity are the Reynolds number (Equation (2.1)), Mach number (Equation (2.2)), and Froude number (Equation (2.3)). It is known that in practice it is impossible to achieve full similarity in aircraft scaling. Therefore one is forced to neglect certain similarity criteria, depending on the test-case. The following similitude cases are the most relevant ones for aircraft scaling:

- Froude similitude - when inertia and gravity forces are dominant
- Reynolds similitude - when inertia and viscous forces are dominant
- Mach similitude - when inertia and elastic forces are dominant

Parameter	**Symbol**	**Dimension**	**Scaling factor**		
			Froude scaling	**Mach scaling**	**Reynolds scaling**
Length	l	L	N	N	N
Froude number	Fr	–	1	$\frac{g_a}{g_m} R_{V_s}^2 \frac{1}{N}$	$\frac{g_a}{g_m} \left(\frac{\nu_m}{\nu_a}\right)^2 \frac{1}{N^3}$
Mach number	M	–	$\frac{\sqrt{\frac{g_m}{g_a} N}}{R_{V_s}}$	1	$\frac{\nu_m}{\nu_a} \frac{1}{R_{V_s}} \frac{1}{N}$
Reynolds number	Re	–	$\frac{\nu_a}{\nu_m} \sqrt{\frac{g_m}{g_a}} N^{3/2}$	$\frac{\nu_a}{\nu_m} R_{V_s} N$	1
Velocity	V	LT^{-1}	$\sqrt{\frac{g_m}{g_a} N}$	R_{V_s}	$\frac{\nu_m}{\nu_a} \frac{1}{N}$
Fluid density	ρ	ML^{-3}	σ	σ	σ
Dynamic pressure	q	$ML^{-1}T^{-2}$	$\sigma \frac{g_m}{g_a} N$	$\sigma R_{V_s}^2$	$\sigma \left(\frac{\nu_m}{\nu_a}\right)^2 \frac{1}{N^2}$
Mass	m	M	$N^3\sigma$	$N^3\sigma$	$N^3\sigma$
Moment of inertia	I	ML^2	$N^5\sigma$	$N^5\sigma$	$N^5\sigma$
Time	t	T	$\sqrt{\frac{g_a}{g_m}}\sqrt{N}$	$\frac{N}{R_{V_s}}$	$N^2 \frac{\nu_a}{\nu_m}$
Aerodynamic coefficient	C_L, C_D, C_M	–	1	$\frac{N}{R_{V_s}^2} \frac{g_m}{g_a}$	$N^3 \frac{g_m}{g_a} \left(\frac{\nu_a}{\nu_m}\right)^2$

Table 2.2: Scaling factors for Froude, Mach, and Reynolds scaling

From these three similarity cases however, only one of them can be met at the same time. For example in low speed flight, compressibility effects are not an issue and therefore the assumption of neglecting the Mach and Reynolds number effects is acceptable. Similitude in this case is achieved by means of *Froude scaling*. In case of compressible flow, similitude of compressibility effects is achieved by *Mach scaling*. In case viscous forces are dominant in the similitude criteria, *Reynolds scaling* is used. Table 2.2 summarize the scaling factors that are to be used for the different scaling methods. A complete derivation of these factors can be found in Appendix B.

For this research, *Froude scaling* is used, since the dynamic motions that will be simulated will be performed at low speed flight. Froude scaling is most commonly used in relevant scaling studies. Eveleens and Bremmers[4] state that scaling effects due to dissimilarities in Mach and Reynolds number are significantly less in comparison to Froude number dissimilarity in for example Mach scaling.

$$Re: \frac{\text{Fluid inertial force}}{\text{Fluid viscous force}} = \frac{\rho V_\infty^2 l^2}{\mu V_\infty l} = \frac{\rho V_\infty l}{\mu} \longrightarrow \mathbf{Re} = \frac{\rho V_\infty l}{\mu} \tag{2.1}$$

$$M: \frac{\text{Fluid inertial force}}{\text{Fluid pressure force}} = \frac{\rho V_\infty^2 l^2}{\rho a^2 l^2} = \frac{V_\infty^2}{a^2} \longrightarrow \mathbf{M} = \frac{V_\infty}{a} \tag{2.2}$$

$$Fr: \frac{\text{Fluid inertial force}}{\text{Fluid gravity force}} = \frac{\rho V_\infty^2 l^2}{\rho g l^3} = \frac{V_\infty^2}{g l} \longrightarrow \mathbf{Fr} = \frac{V_\infty}{\sqrt{g l}} \tag{2.3}$$

2.2. RESEARCH SCOPE

This study does not only focus on the effect of scaling and the potential of this method, but it does also give a more detailed insight in the stability and control behavior of the DUUC which has not been fully investigated yet.

2.2.1. DUUC MODEL

Within the NOVAIR project, part of Clean Sky 2, NLR and TU Delft collaborate on the study towards novel and radical aircraft configurations. TU Delft developed a scale model called the DUUC, which consists of two large ducted fan engines mounted aft on the fuselage as seen in Figure 2.2. The fuselage and wings of this scale model are based on the Boeing 737-700, since these were already available. A remarkable feature is the unconventional tail. The engines are integrated in a circular shaped wing that functions as propeller shielding (debris and noise) as well as a tail. The vertical and horizontal blue vanes that can be seen behind the propellers in Figure 2.2 are used as rudder and elevator. The main goals of this concept are (1) increased propulsive efficiency, (2) noise reduction, and (3) safety.

The first successful flight was performed on 10.08.2016, however minor investigation had been done to the stability and control characteristics of this aircraft. Since the DUUC features an unconventional tail, it will be interesting to see how well the stability and control behavior can be predicted and how certain parameters affect the stability characteristics and handling qualities.

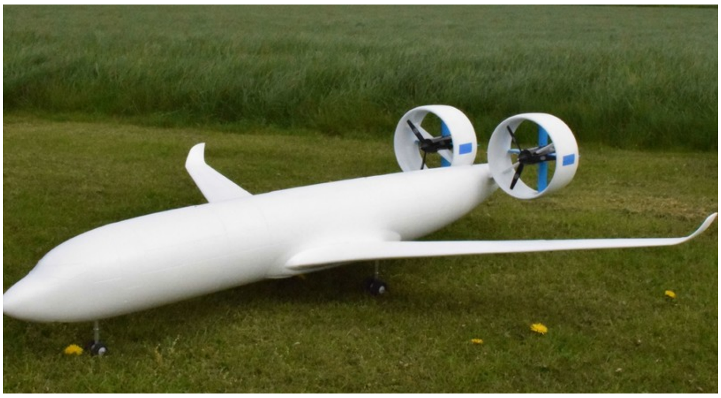

Figure 2.2: Delft University Unconventional Configuration - DUUC

2.2.2. RESEARCH QUESTION AND OBJECTIVES

The development of the scaled DUUC is not only the beginning of research towards the potential of dynamically scaled flight testing in general by the TU Delft, but it is also an unconventional concept which requires more investigation. This lead to the following research question for this thesis:

> *Can the longitudinal stability and control behavior of the DUUC at low speed flight conditions accurately be predicted, by means of dynamically scaled flight testing?*

Subquestions that are derived from this research question are:

- How well does the DUUC perform in terms of handling quality criteria?
- What is the effect of mass and inertia on the stability and control?
- What is the effect of the center of gravity location on the stability and control?
- What are the discrepancies between subscale and full-scale simulation of the DUUC?
- How should the scaled DUUC be configured/controlled in flight tests in order to simulate various full-scale motions?

The objective of the research is to analyse the stability and control of the DUUC, simulated in PHALANX on subscale and full-scale level. This requires some prior steps such as the geometric generation of the subscale and full-scale DUUC model, as well as aerodynamic analysis that is required as input for PHALANX. The following sub-goals can be established that will aid in solving above mentioned research question.

- Create a parametric model of the DUUC, such that one can easily change geometric parameters
- Create a converging CFD model for the complete aircraft (subscale and full-scale)
- Perform a mesh independence study to find an adequate mesh size
- Create a DUUC model within PHALANX and incorporate the aerodynamic results
- Study the handling qualities of the DUUC in PHALANX
- Vary the CG location, mass and inertia characteristics, and aircraft scale in PHALANX

3

PARAMETRIC MODELING OF THE DUUC

As was stated in the research approach, a model of the DUUC should be constructed that can easily be modified. This chapter will treat the parametric modeling of the DUUC. Section 3.1 elaborates upon the already existing Multi-Model Generator (MMG), which is used in this research. It will be seen that the PARAPY model of the DUUC can be split into three major components (fuselage, wing, ducted fan), of which the generation procedures are addressed in Section 3.2.

3.1. MULTI-MODEL GENERATOR

In 2002, TU Delft assisted in a project called the *Multidisciplinary Design and Optimization of Blended Wing-Bodies* by developing a Multi-Model Generator (MMG).[12] This first version of the MMG is implemented in the ICAD environment and is highly flexible and modular, which can therefore be used for many applications of parametric aircraft modeling. The tool makes use of the High Level Primitives (HLP) approach, in which the aircraft is split in various component trunk that each has its own parametric definition. In Figure 3.1 it can be seen that both conventional aircraft configurations as well as novel configurations such as the BWB can easily be modeled by only using four HLPs: wing trunk, fuselage trunk, engine parts, and connection elements.

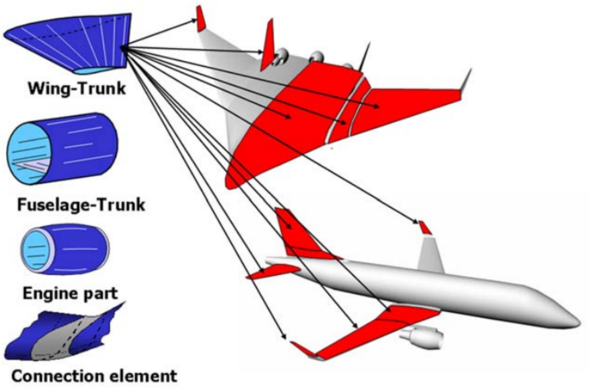

Figure 3.1: High Level Primitives approach of the MMG[13]

When the project was completed however, the ICAD environment was no longer available within the TU Delft and a different platform was needed. In 2010, it was decided to use Genworks GDL, as reasoned by three master students whom together created the new MMG.[14] A few years later, Jian Hao Wei focused his MSc research on the aerodynamic investigation of wing moveables by means of VSAERO. The GDL-based MMG however, did not properly run on an updated version of GDL and the mesher that was implemented could not be used for moveables. These reasons amongst some others described by Wei[15], resulted in the current MMG that is based on the PARAPY platform.

3.1.1. PARAMETRIC MODELING SOFTWARE PARAPY

PARAPY is written in the Python environment, which is a very intuitive and open-source programming language. Python is used in some of the biggest companies in the world. Social media and entertainment platforms such as YouTube and Google make use of Python, but it is also proven to be very effective in special effect and computer animation as mentioned in an interview (Computerworld, 2005) by Tommy Burnette from Industrial Lights & Magic: "Without it a project the size of Star Wars: Episode II would have been very difficult to pull off. From crowd rendering to batch processing to compositing, Python binds all things together" (Burnette[16], 2005). Another interesting field of application is game development. In general the following key characteristics can be linked to Python:

- Object-oriented - Implementations can be structured in an object-based fashion
- Interpreted - Execution of the program is done directly by the interpreter, without the need of compiling prior to it
- Interactive - It is possible to directly interact with the interpreter

Several drawbacks of Python, as concluded by van Dijk and Baan[17], motivated them to create PARAPY which is Python-based and has the following advantageous characteristics in comparison to the standard Python language:

- Lazy - Attributes are only evaluated when needed/demanded
- Lean - Calculations are performed once, after which the result is cached
- Dependency-tracked - Ability to keep track of the dependency of results and prior cached results
- Message-passing - Coupling of object values in the product tree

PARAPY is high-level, therefore no additional methods are required to provide for above mentioned principles. An OpenCascade based geometric kernel is also coupled in PARAPY, which allows for 3-dimensional geometric renderings that can be visualized in the GUI (Figure 3.2).

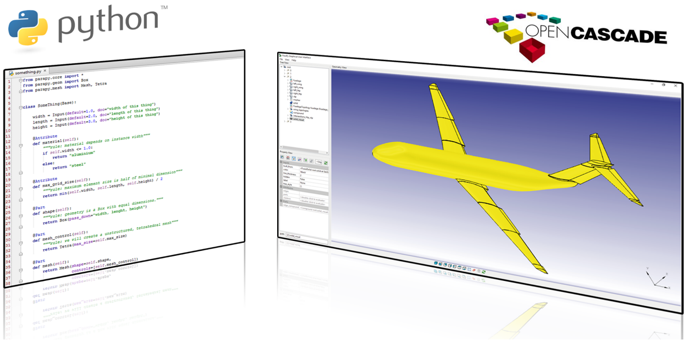

```
from parapy.core import *
from parapy.geom import Box
from parapy.mesh import Mesh, Tetra


class SomeThing(Base):

    width = Input(default=1.0, doc="width of this thing")
    length = Input(default=2.0, doc="length of this thing")
    height = Input(default=3.0, doc="height of this thing")

    @Attribute
    def material(self):
        """rule: material depends on instance width"""
        if self.width <= 1.0:
            return "aluminium"
        else:
            return "steel"

    @Attribute
    def max_grid_size(self):
        """rule: maximum element size is half of minimal dimension"""
        return min(self.width, self.length, self.height) / 2

    @Part
    def shape(self):
        """rule: geometry is a Box with equal dimensions."""
        return Box(pass_down="width, lenght, height")

    @Part
    def mesh_control(self):
        """rule: we will create a unstructured, tetrahedral mesh"""
        return Tetra(max_size=self.max_size)

    @Part
    def mesh(self):
        return Mesh(shape=self.shape,
                    controls=[self.mesh_control])
```

Figure 3.2: The geometric kernel of PARAPY which makes use of Python and OpenCascade[18]

3.1.2. WHY KBE AND PARAPY IN THIS RESEARCH?

This research focuses on the role of dynamically scaled flight testing and the potential to position this technique in an early stage in the design process. The main focus is placed on the stability and control prediction, which requires aerodynamic input as will be explained in Chapter 5. In order to be able to simulate the aerodynamics of an aircraft, a geometric model is required. It is decided to create this model (or models) in a parametric modeling environment such as PARAPY, based on the following key reasons:

Multiple scale models

Since simulation will be performed on both subscale as well as full-scale level, this requires two models of different size. With the KBE structure, it is easy to implement a scaling factor that transforms a model to the desired scale. When different scales have to be investigated, this does not require the time-consuming rebuilding of the model.

Effect of geometric changes

The effect of geometric alterations in for example the nacelle configuration on the flight mechanics of the overall vehicle may be different depending on the scale of the aircraft. In order to investigate such geometric changes, repetitive tasks have to be performed in which KBE can play a significant role to reduce time.

Repetitive mesh generation

PARAPY consists of a mesher, which can quickly generate surface meshes on (parts of) the aircraft body. This grid can be used as an input for aerodynamic solvers. It is urgent to structure the grid in such a way that it provides adequate accuracy (especially in regions of interest) and maintains convergence. In order to find such a grid, it is most likely that multiple grid generations are required. Therefore, the knowledge-base is beneficial in terms of time consumed.

3.2. PARAPY MODEL OF THE DUUC

The DUUC is presented in Section 2.2, from which it could be seen that the aircraft is a conventional tube-wing configuration. This means that the fuselage and wing trunks of the MMG can be used to form the overall shape of the aircraft. Since the current MMG does not consist of a ducted-fan or propeller class yet, it was necessary to create this module.

3.2.1. FUSELAGE GENERATION

The generation of the fuselage can be split into the following three steps:

- Rails generation
- Cross-sections generation
- Lofting

The *rails* are curves that run from the nose of the fuselage to the tail. Four rails are needed to define the fuselage shape: a top rail, belly rail, and two rails that run on each side of the body. These curves are B-splines that requires some input parameters such as the control points through which the splines have to go. Figure 3.3a shows a side and top view of the generated rails. Since a fuselage is symmetrical in the XZ-plane, one of the two side curves is a mirrored version of the other. The inputs listed below are used to generate the top and belly rails. The *X* in these input parameters should therefore be replaced by *top* and *bottom* with corresponding data.

X_extremes_points_list

This list consists of two coordinates, that represent the starting and ending points of the rail.

X_control_points_list

The control points are defined in this list, which are coordinates through which the fuselage rails should go. Note that the extreme points defined in previous input list are not included in the control point list. Due to symmetry of the fuselage, this curve is 2-dimensional. This means that all Y-values of the top and belly control points are equal to 0, and all Z-values of the side control points are equal to 0.

X_weights_list

The B-splines that form the rails are non-rational as default (i.e. all weights are equal to 1). However, weights can be applied to the control points of interest if desired.

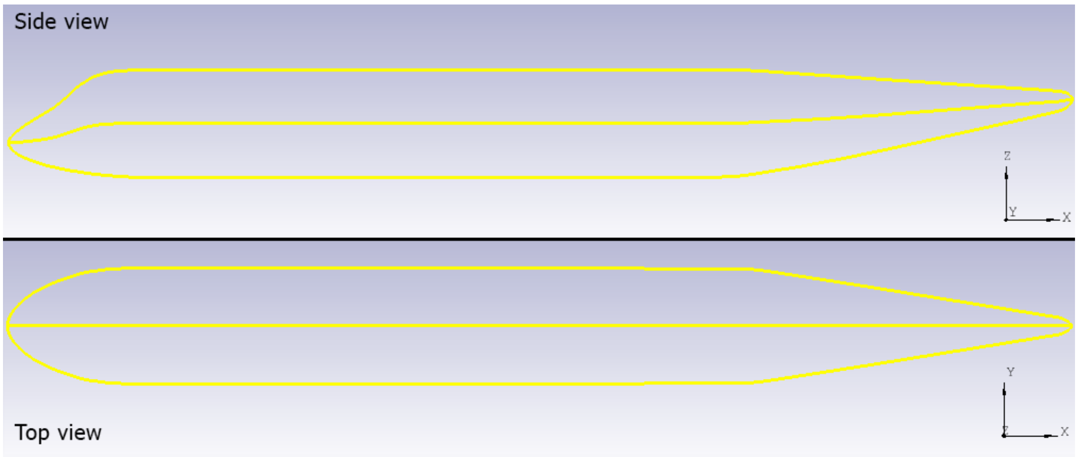
Side view
Z
Y
X
Top view
Y
Z
X

(a) Rails forming the edges of the fuselage

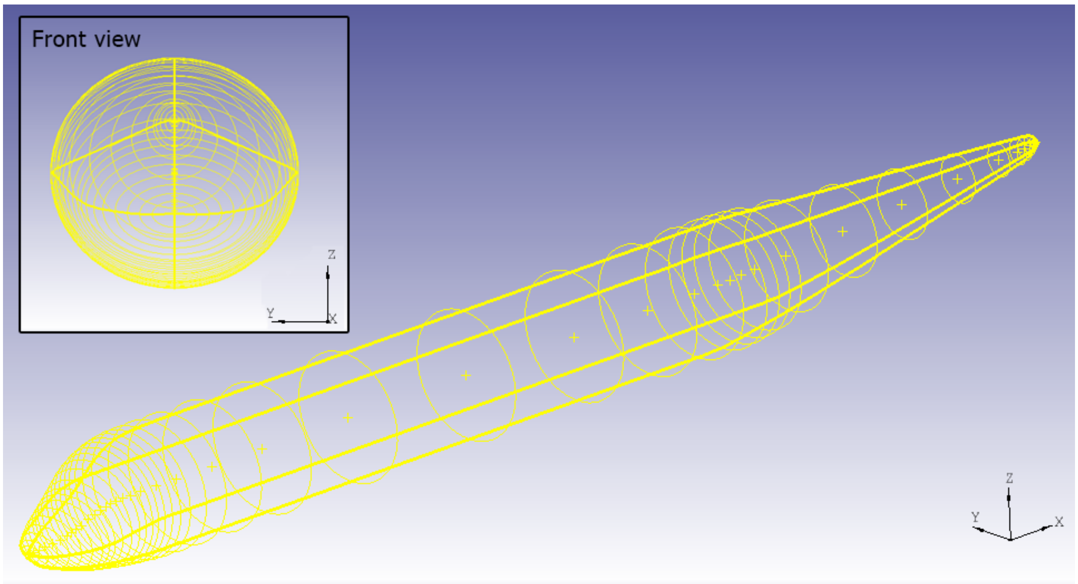
Front view
Z
Y
X
Z
Y
X

(b) Cross-sections defined by the four rails forming the outer skeleton of the fuselage

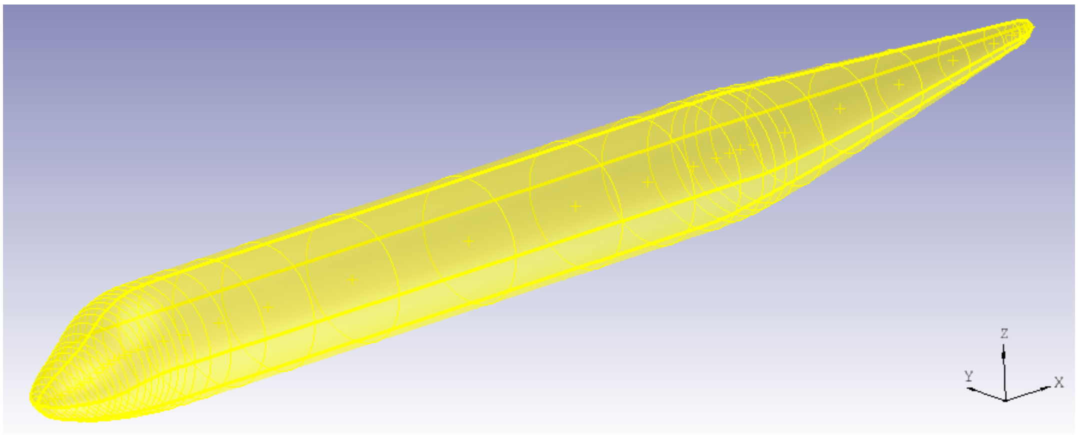

(c) Lofted surface in-between the longitudinal fuselage cross-sections

Figure 3.3: Generation of the fuselage object in ParaPy

The generation of the side curves also need the three inputs stated above, in which the curve is projected on the XY-plane as seen in the top view of Figure 3.3a (hence all Z-coordinates of the control points are equal to 0). In addition however, the side rails need information regarding the so called *dip*. This dip is required since the fuselage is usually not symmetrical in the XY-plane as can be seen from the side view in Figure 3.3a. Due to this dip, the side rails become 3-dimensional. The following two inputs are required to model this dip:

side_dip_extremes_points_list
This list is similar to the X_extremes_points_list described above, however the Z-coordinate is taken into account as well.

side_dip_control_points_list
This list is similar to the side_control_points_list described above, however this time the rail is projected on the XZ-plane.

The fuselage input file that PARAPY reads does not only contain rails information, but also CST-coefficients that are used to generate the fuselage cross-sections. The construction of these cross-section requires the previous generated fuselage rails. In each longitudinal position, a cross-section can be positioned as can be seen in Figure 3.3b. The width and height of each cross-section are measured from Boeing 737-700 blueprints. Now that the cross-sections are placed, a loft can be created in-between them. This will form the skin of the fuselage as shown in Figure 3.3c.

3.2.2. WING GENERATION

The wing component is modeled in a similar way as the fuselage, with rails that define the positioning of the cross-sections which in turn form the outer shell of the wing. The following steps can thus be seen in the generation:

- Rails generation
- Airfoils generation
- Lofting

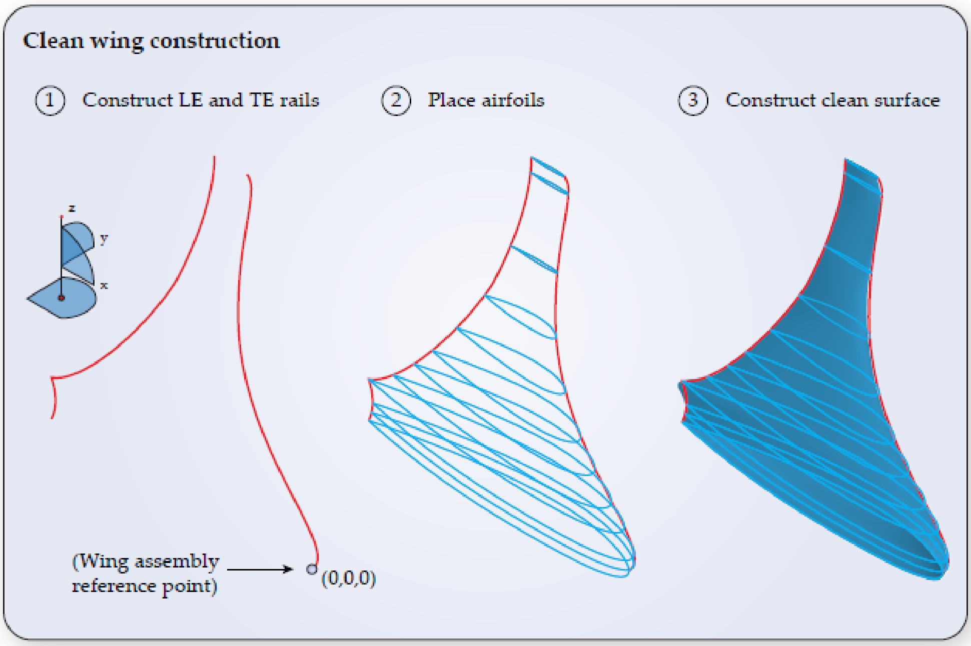
Clean wing construction
① Construct LE and TE rails
② Place airfoils
③ Construct clean surface
z
y
x
(Wing assembly reference point)
(0,0,0)

Figure 3.4: Steps in generating the wing part in the MMG[14]

This method allows for the generation of all kind of wing shapes such as a complex BWB wing, which is not simply trapezoidal. A downside however, is that editing of the wing geometry requires a change in the selection of control points which define the wing rails. This selection of control points is not as straightforward as for example specifying a sweep angle or wingspan for trapezoidal wings. Figure 3.4 shows the construction of a complex wing shape according to above listed steps.

The inputs that are required to construct the wing are divided into four groups: positioning, geometric parameters, rails information, and movables parameters. The position of the leading edge of the root is specified in the input file by means of coordinates. The *parameters* group contains information regarding the spanwise airfoil locations, kink location(s), and airfoil thickness. The *rails* that define the shape of shape of the wing are the leading edge and trailing edge rails. To these rails, twist and dihedral can be added to form the desired wing shape. These steps are shown in Figure 3.6. The five inputs for the wing rails construction are listed below:

le_point_list
This list consists of coordinates, specifying the leading edge in the XY-plane.

te_point_list
Similar coordinate list as described above, consisting of trailing edge control points in the XY-plane.

dihedral_point_list
This point list consists of coordinates in the YZ-plane, and defines the dihedral curve as seen in Figure 3.6.

twist_axis_point_list
The axis about which the wing is twisted is specified in this coordinate list. This axis does not necessarily have to be a straight line.

twist_points
Finally, the twist is applied according to this coordinate list. Similarly to the dihedral curve, the twist curve is specified in the YZ-plane as shown in Figure 3.6.

For the DUUC model, the Boeing 737-700 wing geometry is considered as reference. The wing is tapered and has a sweep angle of 25%. The PARAPY model of the wing connected to the fuselage is presented in Figure 3.5.

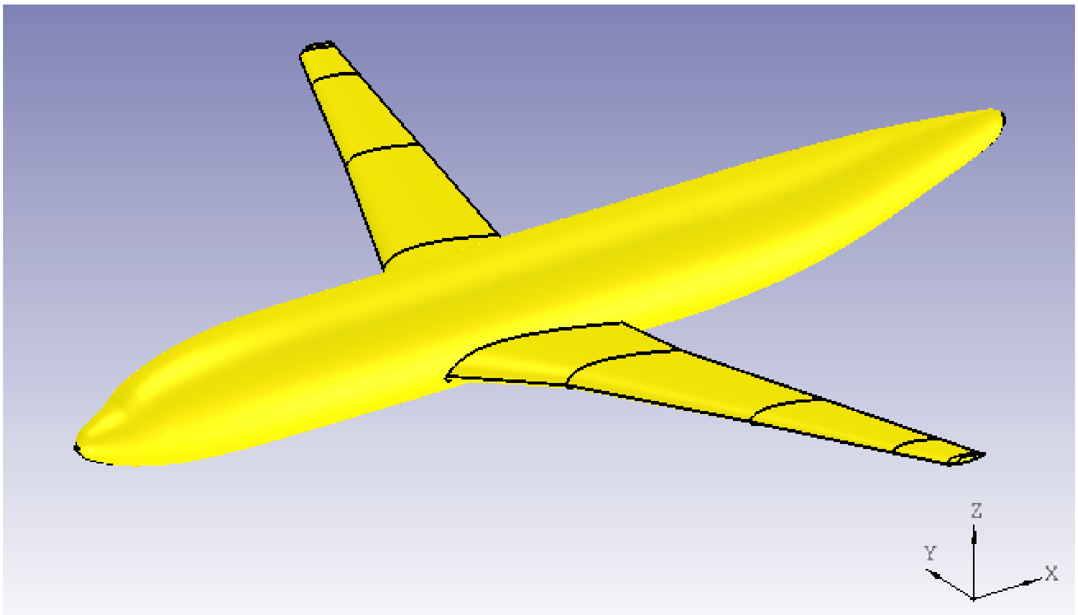

Figure 3.5: PARAPY model of the tube-wing configuration of the DUUC

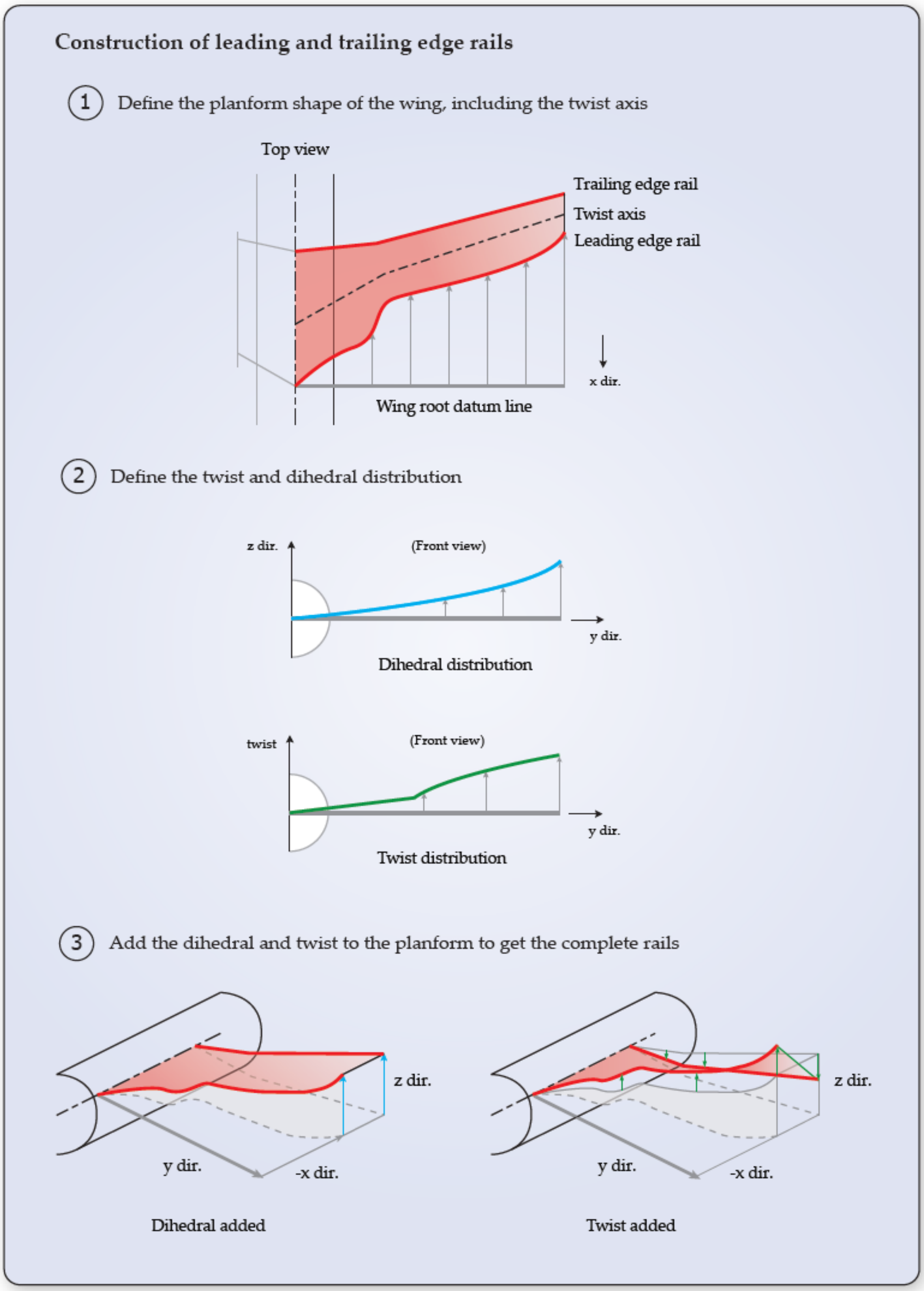
Construction of leading and trailing edge rails
1 Define the planform shape of the wing, including the twist axis
Top view
Trailing edge rail
Twist axis
Leading edge rail
x dir.
Wing root datum line
2 Define the twist and dihedral distribution
z dir.
(Front view)
y dir.
Dihedral distribution
twist
(Front view)
y dir.
Twist distribution
3 Add the dihedral and twist to the planform to get the complete rails
z dir.
y dir.
-x dir.
Dihedral added
z dir.
y dir.
-x dir.
Twist added

Figure 3.6: Steps in generating the leading and trailing edge rails in the MMG[14]

3.2.3. DUCTED FAN GENERATION

This module is created by the author and consists of the following parts: (1) outer duct that forms a shielding around the propeller, (2) the pylon that connects the duct to the fuselage, (3) a center body to which the (4) propeller and (5) control vanes are attached. The ducted fan is completely parametric, which allows for easy alteration of various dimensions. Table 3.1 gives an overview of the input parameters for each of the above stated parts. A visual representation of the parameters can be found in Figure 3.7a and Figure 3.7b. The global position of the propulsive empennage is set by x_{duct}, y_{duct}, and z_{duct}. The angle that the pylon makes with the body Y-axis, from a front view perspective is denoted as the cant angle ϕ.

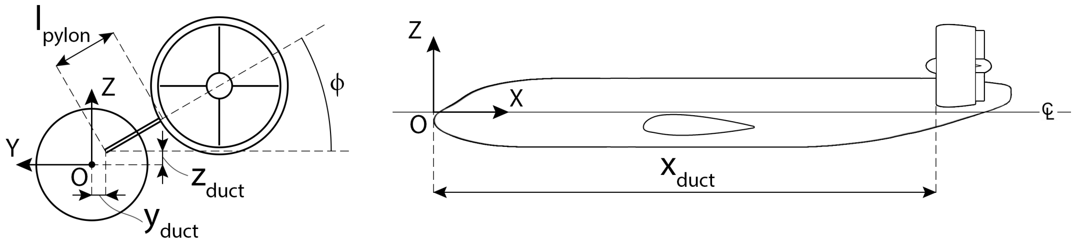
l_{pylon}
Z
Y
O
ϕ
z_{duct}
y_{duct}
Z
X
O
x_{duct}
℄

(a) Description of the position of the ducted fan: (left) front view and (right) side view

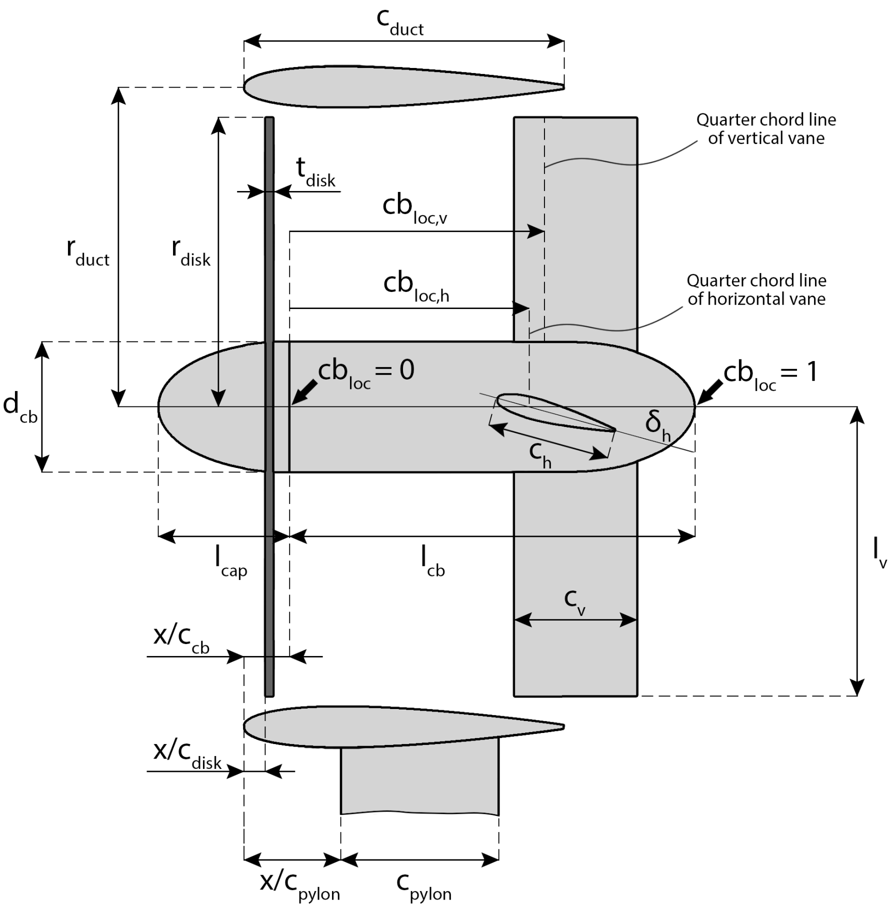
c_{duct}
Quarter chord line of vertical vane
t_{disk}
$cb_{loc,v}$
r_{duct}
r_{disk}
$cb_{loc,h}$
Quarter chord line of horizontal vane
d_{cb}
$cb_{loc} = 0$
$cb_{loc} = 1$
δ_h
c_h
l_{cap}
l_{cb}
l_v
c_v
x/c_{cb}
x/c_{disk}
x/c_{pylon}
c_{pylon}

(b) Description of the ducted fan shape

Figure 3.7: Definition of the parameters describing the positioning and shape of the ducted fan geometry

DUCT

The cross-section of the duct is an airfoil itself, which means that a coordinate file has to be imported similarly to the generation of the wing. This cross-section can then be placed at a duct radius distance away from the rotation axis, which is the Z-axis in PARAPY. The next step is to revolve the cross-section around the rotation axis to form a 3-dimensional duct shape. Finally the solid duct is oriented such that it is facing the flow as can be seen in Figure 3.8a. A NACA 0012 profile is used, which is also used in the scaled DUUC model in Figure 2.2. Besides the airfoil itself, the chord length of the airfoil and the radius of the duct are user defined inputs which can easily be altered.

Part	Parameter	Description
Ducted fan	$position$	XYZ-coordinate of the complete ducted fan engine
	ϕ	Cant angle w.r.t. the Y-axis in the YZ-plane
Duct	$airfoil$	Airfoil coordinate file
	r_{duct}	Duct radius
	c_{duct}	Duct chord length
Pylon	$airfoil$	Airfoil coordinate file
	l_{pylon}	Pylon length
	c_{pylon}	Pylon chord length
	x/c_{pylon}	Location of the pylon LE in duct chord percentage
Center body	d_{cb}	Center body diameter
	l_{cb}	Center body length
	x/c_{cb}	Location of the center body in duct chord percentage
Propeller	r_{disk}	Disk radius
	t_{disk}	Disk thickness
	l_{cap}	Propeller cap length
	x/c_{disk}	Location of the actuator disk in duct chord percentage
Control vane	$airfoil$	Airfoil coordinate file
	l_{vane}	Control vane semi-span
	c_{vane}	Control vane chord length
	cb_{loc}	Location of the vane on the center body (0 - 1)
	δ_{vane}	Control vane deflection

Table 3.1: Input parameters for the ducted fan module

PYLON

The pylon can be seen as another wing, which is straight and untapered in the case of the DUUC. However, the wing module discussed in Section 3.2.2 will not be used since this doesn't allow for simple geometric changes in for example the length or the chord length of the wing. The pylon is simply a rectangular wing, built from a root and a tip airfoil that can be changed by selecting the desired airfoil coordinate data file. A lofted surface is created in-between the two airfoils to form a solid wing, which is then placed on the specified longitudinal location on the fuselage. Figure 3.8b shows how the pylon connects the duct to the aft fuselage. The pylon does not go all the way through the duct due to convergence problems in the aerodynamic analysis.

CENTER BODY

The center body functions as shielding of electronics that drive the propeller, and is at the same time a streamlined body ensuring a smooth airflow between duct inlet and outlet. It is simply modeled as a combination of a cylinder and an ellipsoid as can be seen in Figure 3.8c. The major semi-axis of the ellipsoid is in this case set equal to the diameter of the center body. The location of this part within the duct is entered as a fraction of the duct chord length (x/c_{cb}) as seen in Figure 3.7b.

PROPELLER

Two geometries can be distinguished while looking at the propeller part in Figure 3.8d. First of all the propeller cap which is attached to the flat side of the center body, is modeled as half of an ellipsoid. The second part is the thin disk, which represents the propeller blades in the form of an actuator disk. The radius of the disk is 90% of the duct radius, in order to account for tip clearance between the blade tip and the duct. The disk is longitudinal positioned as fraction of the duct chord length.

CONTROL VANES

The last components that are part of the ducted fan module, are the horizontal and vertical control vanes. They are connected to the aft center body and function as control surfaces that guide the propeller slipstream. They are built up in a similar fashion as the pylon, hence two airfoils connected with no sweep and no taper. In the DUUC model, the vanes are attached to the duct and center body by a rod located at the quarter chord line. This rod then functions as the rotation axis, driven by actuators in the center body. Since the vanes should be able to rotate without touching other components in their vicinity, gaps are present between the vanes and the center body. These gaps are not included in the PARAPY model, to enhance aerodynamic solving. The complete ducted fan with control vanes attached can be seen in Figure 3.8e.

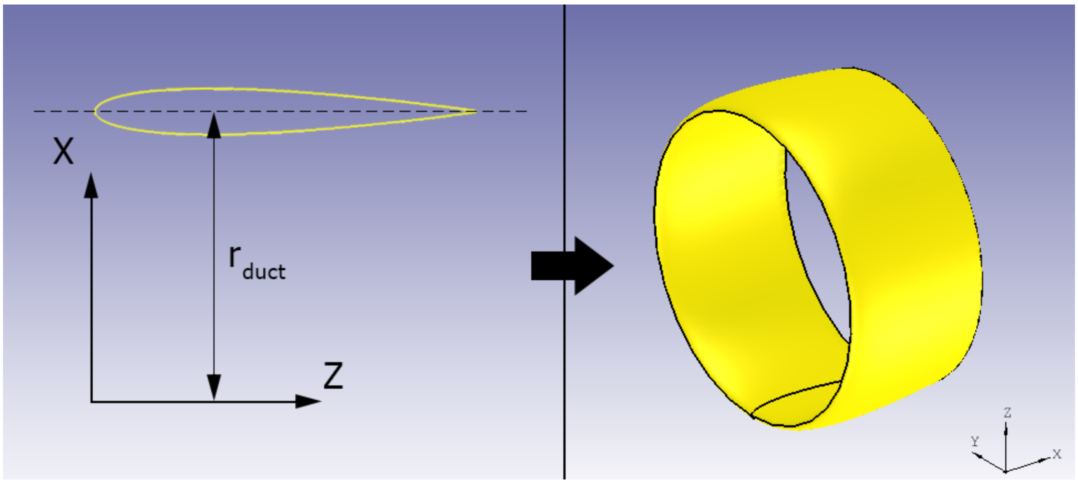

(a) Revolved duct airfoil forming a solid duct shape

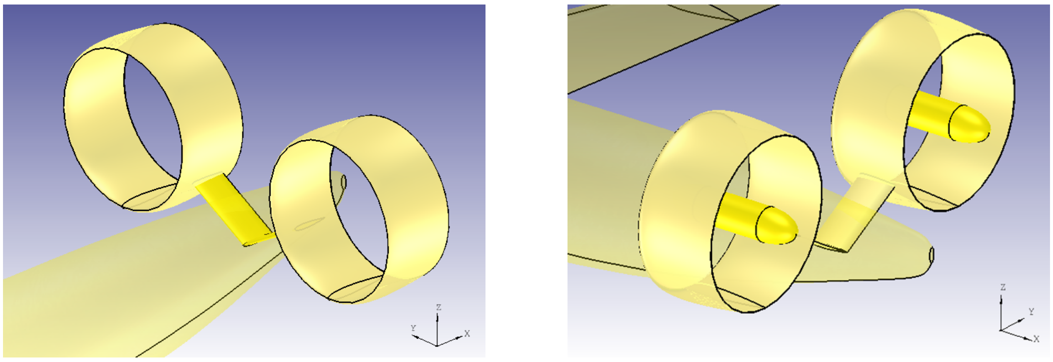

(b) Pylon connecting the duct to the aft fuselage

(c) Center body in the center of the duct

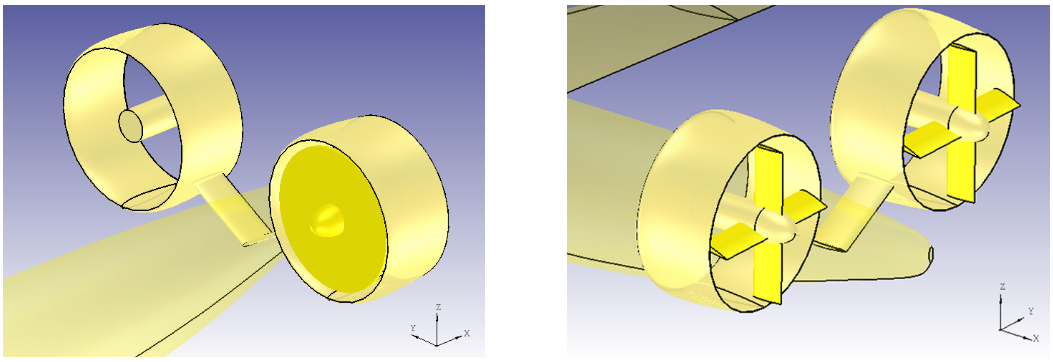

(d) Propeller cap and actuator disk

(e) Horizontal and vertical control vanes

Figure 3.8: Steps in generating the ducted fan part in PARAPY

4

Aerodynamic Analysis

The research is performed using the high fidelity CFD software ANSYS Fluent, capable of solving complex flows that arise in the propeller slipstream. The steps that are present in the CFD chain are the geometry definition, mesh generation, solver setup, and post-processing. These steps are connected within the ANSYS Workbench module as can be seen in Figure 4.1.

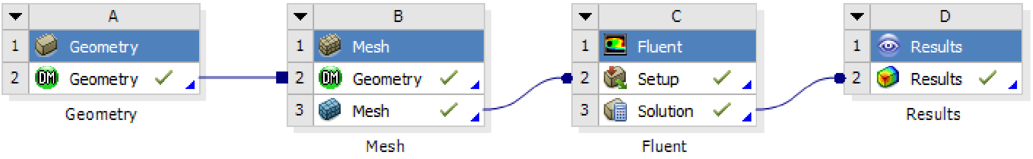

Figure 4.1: ANSYS Fluent project schematic

Above figure shows that a project starts with the definition of the geometry. In this module, the model is prepared for subsequent meshing as will be described in Section 4.1. The meshing procedure and resulting mesh is presented in Section 4.2. This mesh can then be imported by the Fluent module (Section 4.3), in which the solver setup is defined and the calculations are performed. Finally, the results are presented and discussed in Section 4.4. The TU Delft cluster is used for the large amount of computations that had to be performed, of which additional information including an example input file can be found in Appendix C.

4.1. Geometry Definition

In the geometry module (*DesignModeler*), the DUUC .stp file is imported that was created in ParaPy. The DesignModeler automatically detects the different parts that were defined in the .stp file and displays them in the tree on the left-hand side of the interface, shown in Figure 4.2. The model has to be prepared for volume meshing, which requires an enclosure around the solid body that acts as a fluid domain (in this case air). Such an enclosure can be seen in Figure 4.3, for which the dimensions in each direction can be manually specified. Flow symmetry is assumed in the XZ-plane, since the longitudinal characteristics will only be considered. Therefore the complete model (aircraft and enclosure) can be split in half, significantly reducing grid generation and computation time. Another fluid domain is required around the duct since this part needs some extra mesh refinement. Finally, some faces and edges should be tagged to ensure easy access to them in further stages such as meshing and post-processing. The following *Named Selections* are created:

Faces		**Edges**
Boundary conditions	**Solid walls**	
Inlet	Fuselage	Fuselage (top/bottom)
Outlet	Wing	Wing TE
Symmetry	Pylon	Pylon TE
Far field	Duct	Duct TE
Fan	Horizontal vane	Horizontal vane TE
	Vertical vane	Vertical vane TE
	Center body	

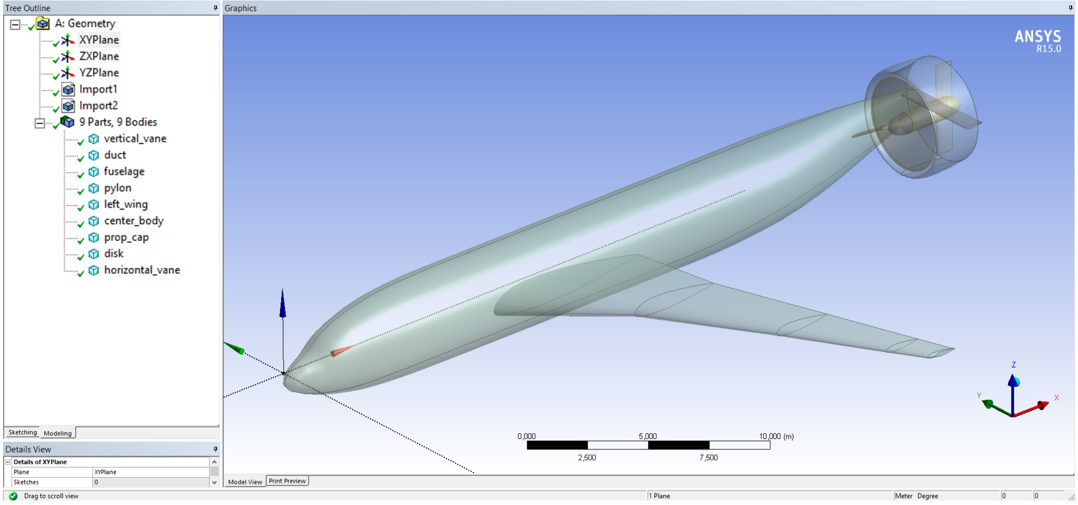
Tree Outline
A: Geometry
XYPlane
ZXPlane
YZPlane
Import1
Import2
9 Parts, 9 Bodies
vertical_vane
duct
fuselage
pylon
left_wing
center_body
prop_cap
disk
horizontal_vane
Sketching
Modeling
Details View
Details of XYPlane
Plane XYPlane
Sketches 0
Graphics
ANSYS
R15.0
0,000
5,000
10,000 (m)
2,500
7,500
Z
Y
X
Model View
Print Preview
Drag to scroll view
1 Plane
Meter Degree
0
0

Figure 4.2: DUUC model imported in the ANSYS DesignModeler

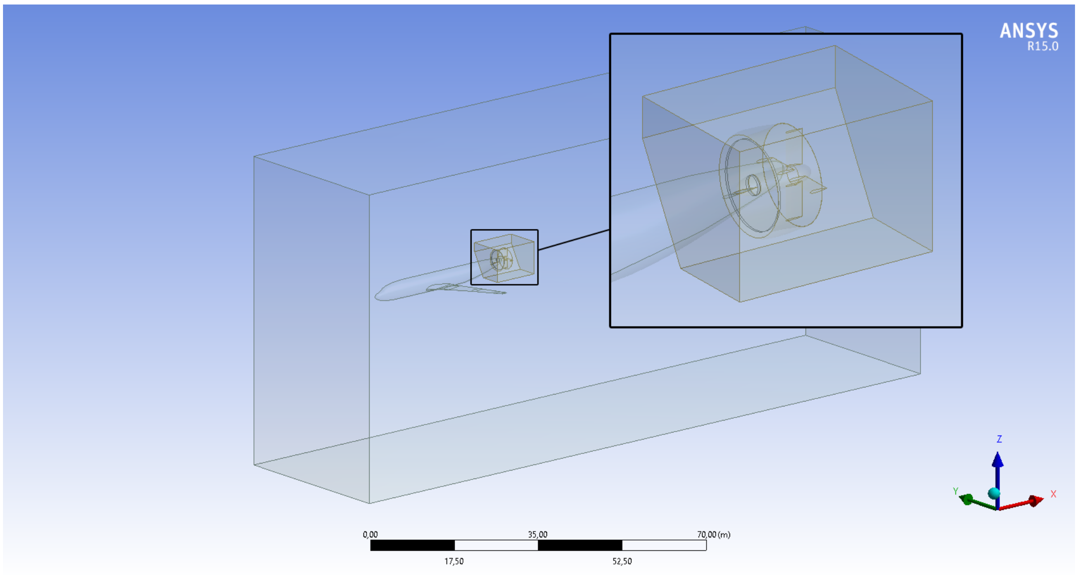
ANSYS
R15.0
Z
Y
X
0,00
35,00
70,00 (m)
17,50
52,50

Figure 4.3: Outer fluid domain around the aircraft body and inner fluid domain around the duct

4.2. MESH GENERATION

The second step in the aerodynamic analysis chain is the meshing of the model. The meshing of the fluid domain that was defined in previous section, is discussed in Section 4.2.1. A mesh convergence study is carried out, from which an adequate mesh size is obtained as will be explained in Section 4.2.2. For general meshing considerations, mesh quality metrics, and boundary layer refinement, the reader is encouraged to consult Appendix D.

4.2.1. MESHING THE DUUC

A side view of the mesh is presented in Figure 4.4 in which it can be seen that the largest part of the fluid domain consists of coarse elements of about 2 m. The elements get smaller towards the aircraft walls, with a growth rate of about 1.25. A closer look is taken at the mesh structure around and within the duct. This local refinement can be observed in Figure 4.5, with the gray elements being the outer domain and the green elements forming the inner domain. The bottom image is a zoom of one half of the duct, in which the inflation layers can be distinguished. One can also observe that the trailing edge of the airfoil section is cut. Each component that has an airfoil shape consists of edge sizings such that two elements span across the thickness of the trailing edge.

For the inflation layers a y^+ of 50 is selected, resulting in a first layer height of about 0.25 mm. A total of 20 layers are created around the components within the duct, whereas the fuselage and wing are surrounded by 10 layers with a slightly larger growth rate. Since the airflow around the fuselage and wing is not disturbed, the first layer height is also doubled with respect to the duct (hence a y^+ of 100). This significantly reduces the amount of grid cells, while keeping the refinement in the area of interest around the duct.

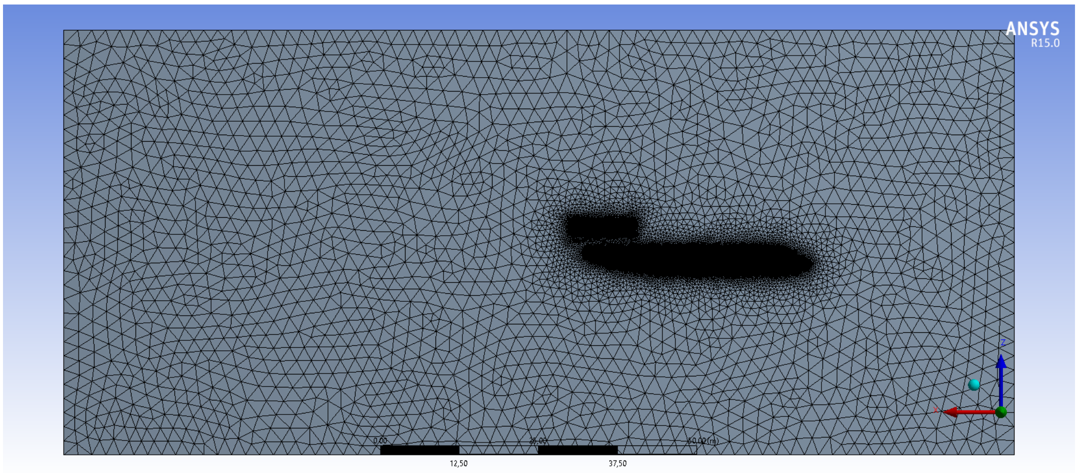

Figure 4.4: Side view of the DUUC mesh

4.2.2. MESH CONVERGENCE STUDY

A mesh independence study was performed, from which a sufficient mesh density was found where minor changes in element size does not affect the solution. This study is performed at an angle of attack and horizontal vane deflection of both zero degrees, and an airspeed of 77 m/s and 18 m/s for the respective full-scale and subscale case.

FULL-SCALE

A total of 6 meshes have been created, by varying volume and face sizing settings. A detailed description of the exact numbers that are used can be found in Appendix E, along with lift and drag data. The values of **Mesh 3** are selected as baseline. The other meshes are obtained by multiplying all the sizing values by the same factor, e.g. **Mesh 2** is 1.5 times **Mesh 3**. The obtained mesh sizes are listed in Table 4.1.

The lift coefficient on each component for the different mesh densities is shown in Figure 4.6. In this figure, the blue dots represent the results obtained with FLUENT, whereas the red curve is an asymptotic curve fit.

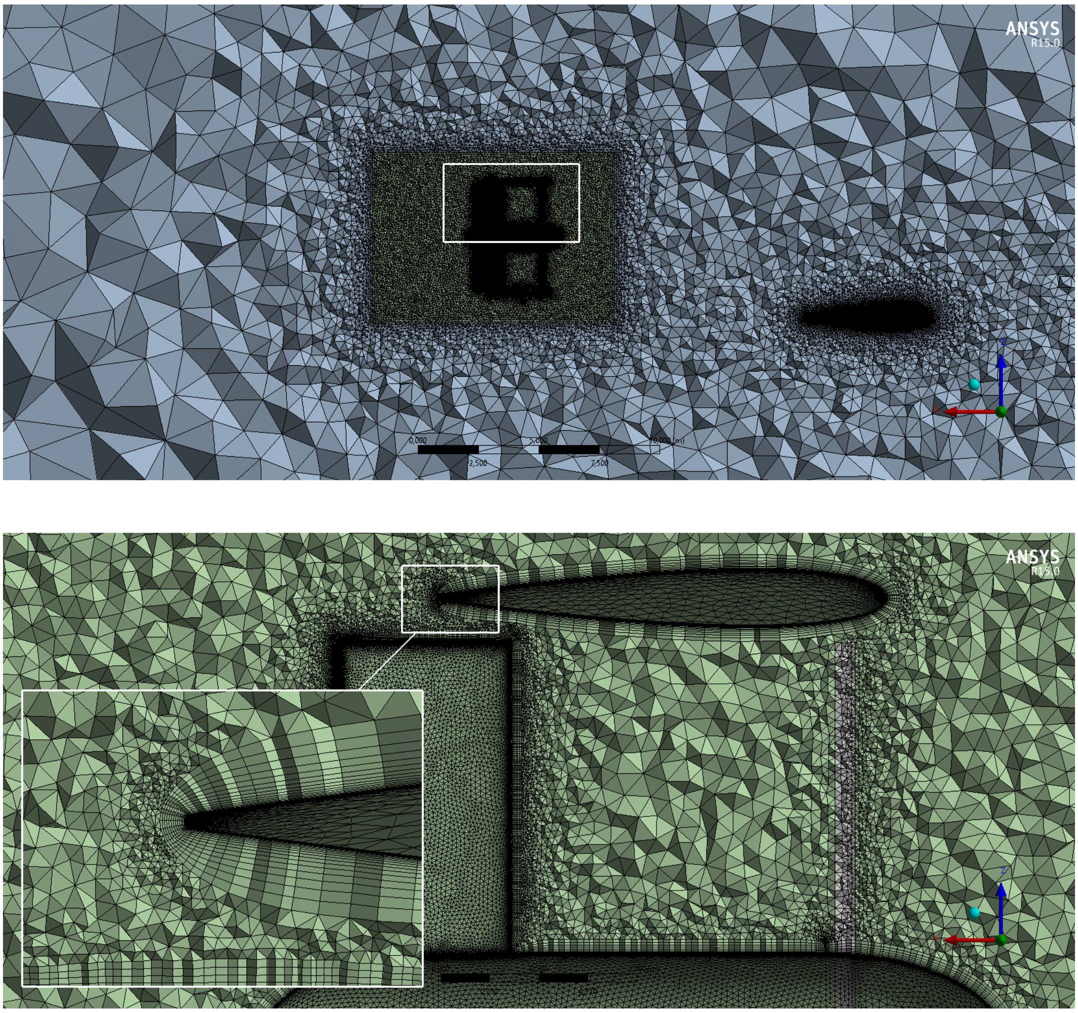

Figure 4.5: Mesh on the duct cross-section

	Mesh F1	Mesh F2	Mesh F3	Mesh F4	Mesh F5	Mesh F6
N	20,246,701	22,296,827	27,051,305	31,037,714	34,722,260	38,830,864

Table 4.1: Number of elements in the full-scale meshes that are used in the mesh convergence study

This fit is constructed using the asymptotic function in Equation (4.1), within a Matlab optimization (*fmincon*) routine to minimize the least squares error.

$$y = C + A\left(1 - e^{-k\hat{N}}\right) \tag{4.1}$$

where C is the value of y at $\hat{N} = 0$, A is the amplitude, and k is the half-life rate. The number of elements in the mesh (N) has been rewritten such that **Mesh 1** and **Mesh 6** correspond to $\hat{N} = 0$ and $\hat{N} = 1$ respectively. The linear relation in Equation (4.2) is used for this and the reason for the introduction of this variable is to aid the optimizer by a realistic initial value of the variable C, since it should be close to the coefficient at $\hat{N} = 0$.

$$\hat{N} = \frac{N - N_{\text{mesh 1}}}{N_{\text{mesh 6}} - N_{\text{mesh 1}}} \tag{4.2}$$

When the asymptotic curve fits are constructed for each lifting surface, the required mesh density can be determined. In this study, a threshold of 2% deviation from the final lift value is set. This final value is obtained by taking the limit of Equation (4.2) as $\hat{N} \to \infty$. The black dotted lines in Figure 4.6 show these bounds, from which it can be seen that the highest value of $\hat{N}$ where the asymptote enters the 2% error region is

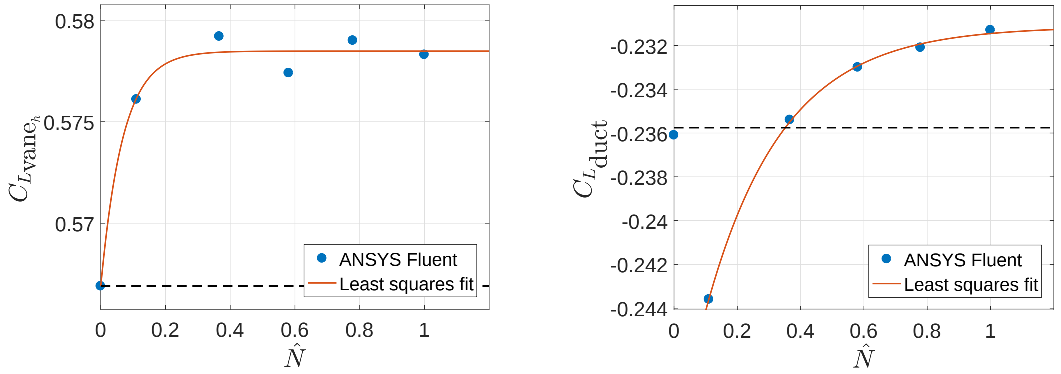

(a) Horizontal vane (b) Duct

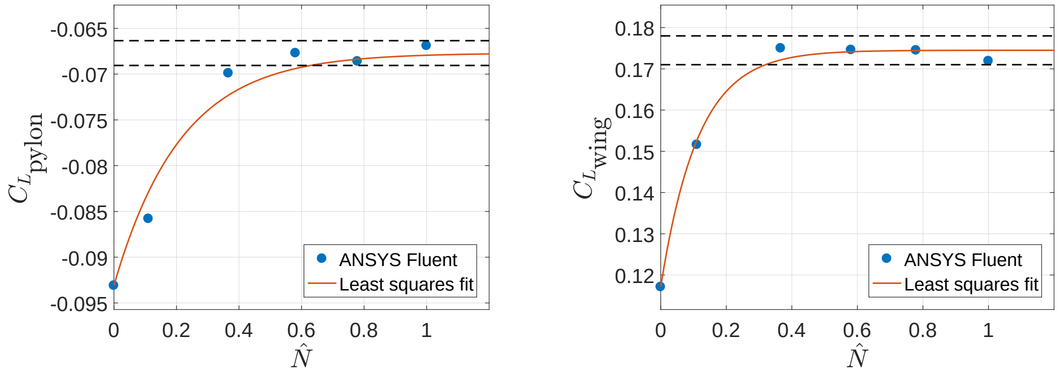

(c) Pylon (d) Wing

Figure 4.6: Lift coefficient as function of mesh density for the full-scale simulation, showing mesh convergence

determined by the pylon. This crossover point results in a value of $\hat{N} = 0.633$, from which a minimum mesh size of $N = 32,016,614$ elements is obtained.

Similarly, the pressure drag coefficients are studied for the different meshes. The wing area is selected as reference area for each component, which makes it easier to see how the component drag values relate to each other. The total drag will then be the sum of all individual contributions. The least squares curve fits can be seen in Figure 4.7, again with the 2% error bounds. From these plots it can be seen that the crossover points for almost all components are around or lower than the $\hat{N} = 0.633$ as was found for the lift coefficients. The $C_{D_{wing}}$ however, drops below the 2% threshold around $\hat{N} = 1$. In order to select a proper mesh for the CFD calculations, both the lift coefficients as well as the drag coefficient convergence plots are considered. From the lift data a minimum mesh size of $N = 32,016,614$ elements was found, and the total drag coefficient curve in Figure 4.7h shows to be accurate enough with this mesh density. Therefore **Mesh 5** is selected to be used for the remaining full-scale CFD analysis.

SUBSCALE

The subscale meshes are listed in Table 4.2. The size of the meshes that are used for the subscale grid independence study are slightly coarser w.r.t. the full-scale ones, due to the lower airspeed reducing complex flow phenomena. The lift and drag results of each mesh are again plotted, shown in Figure 4.8 and Figure 4.9. A least squares fit is derived again using the asymptotic function of Equation (4.1). From the lift results it can be seen that the horizontal vane, duct, and pylon converge quite early on at about $\hat{N} = 0.15$. The wing trend increases more gradually, resulting in a crossover point with the 2% threshold around $\hat{N} = 0.6$.

The pressure drag results show that convergence is obtained for all components at $\hat{N}$ below 0.5. Both the horizontal and vertical vanes show a very rapid decrease in drag between meshes S1 and S2, after which this quantity keeps on decreasing gradually. Their contribution to the total drag however is nearly 2 orders

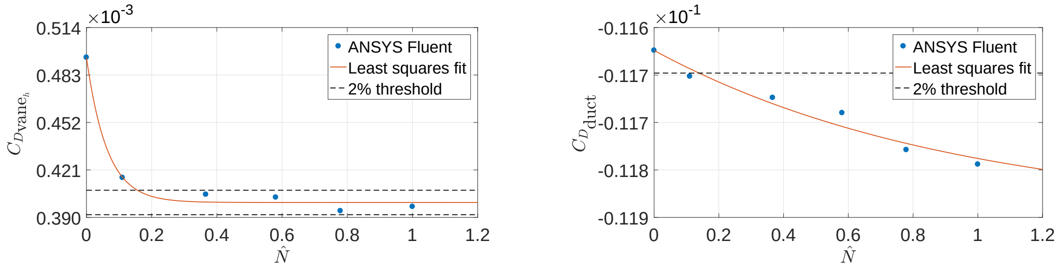

(a) Horizontal vane (b) Duct

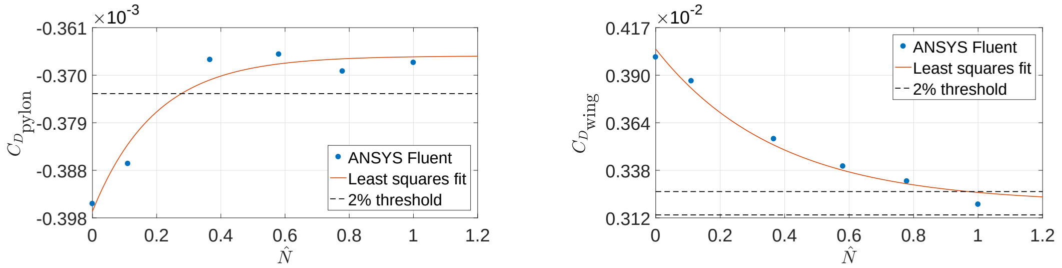

(c) Pylon (d) Wing

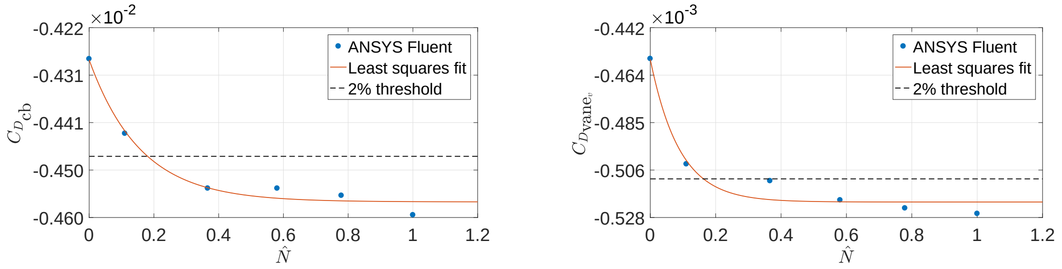

(e) Center body (f) Vertical vane

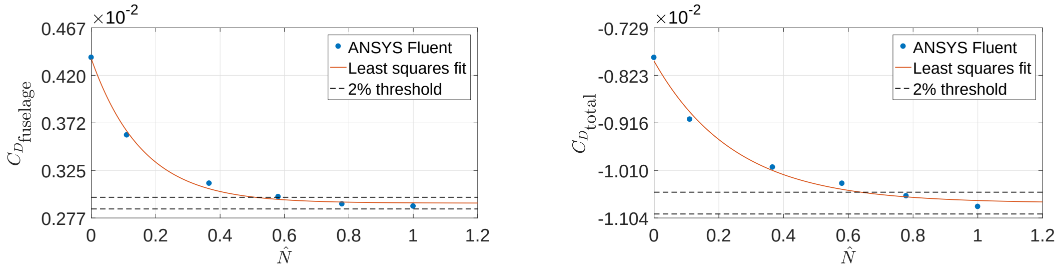

(g) Fuselage (h) Total

Figure 4.7: Pressure drag coefficient as function of mesh density for the full-scale simulation, showing mesh convergence

of magnitude smaller in comparison to the other components. The total drag depicted in Figure 4.9h falls within the 2% error margin around $\hat{N} = 0.45$. From both lift and drag results, **Mesh S5** is found to be adequate for the CFD calculations of the subscale model.

MESH QUALITY

The skewness and orthogonality quality metrics are evaluated for each mesh in the convergence study. A skewness value of 0 and an orthogonality of 1 indicates an equilateral cell (i.e. best quality). Appendix D

	Mesh S1	Mesh S2	Mesh S3	Mesh S4	Mesh S5	Mesh S6
N	13,878,272	14,735,094	15,391,603	20,456,759	26,311,589	31,670,024

Table 4.2: Number of elements in the subscale meshes that are used in the mesh convergence study

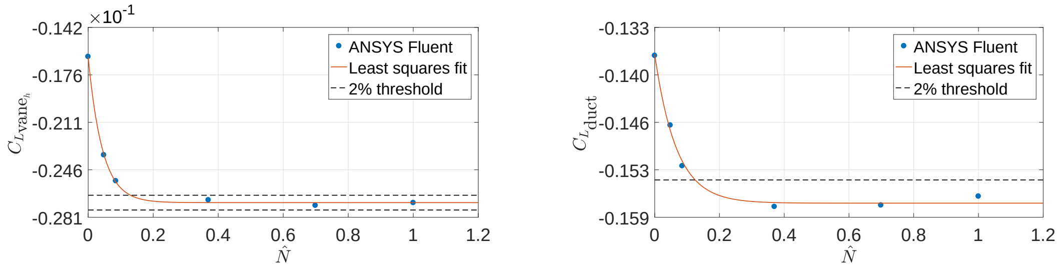

(a) Horizontal vane

(b) Duct

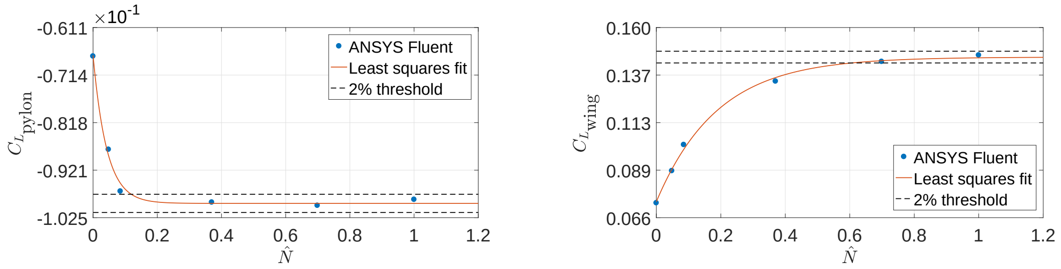

(c) Pylon

(d) Wing

Figure 4.8: Lift coefficient as function of mesh density for the subscale simulation, showing mesh convergence

describes the most important mesh quality metrics and how they are derived. The average quantity of these metrics of the full-scale meshes are computed by the ANSYS mesher and presented in Table 4.3. First of all it can be seen that as the mesh size increases (becomes finer), the skewness decreases and the orthogonality increases, hence the quality becomes better. All skewness quantities are just above 0.25, which is said to be the border between good and excellent qualities. The orthogonality values are found to be around 0.85, which corresponds to a good mesh. Figure 4.10a shows a bar plot of the skewness quality of mesh F5, from which it can be seen that the majority of the elements are indeed in the good-excellent quality regime. Two types of elements are shown in the figure: red corresponds to tetrahedron elements, whereas the green bars depict wedge elements. The skewness distribution of the wedges is similar to the tetrahedrons, however the orthogonal quality of the wedges is much better as can be seen in Figure 4.10b. This is the result of the structure composition of the inflation layers.

The subscale quality metrics are listed in Table 4.4. The quality of all 6 meshes can again be classified as good, since the skewness and orthogonality metrics are around 0.25 and 0.85 respectively. It was concluded that mesh S5 is used for the aerodynamic analysis of the subscale DUUC, for which the skewness and orthogonality metric distributions are shown in Figure 4.11a and Figure 4.11b respectively. Similar trends are obtained as the ones for the full-scale mesh.

	Mesh F1	Mesh F2	Mesh F3	Mesh F4	Mesh F5	Mesh F6
Skewness	0.295	0.287	0.272	0.262	0.256	0.251
Orthogonality	0.831	0.838	0.848	0.855	0.859	0.862

Table 4.3: Mesh quality metrics (average) of the full-scale mesh convergence study

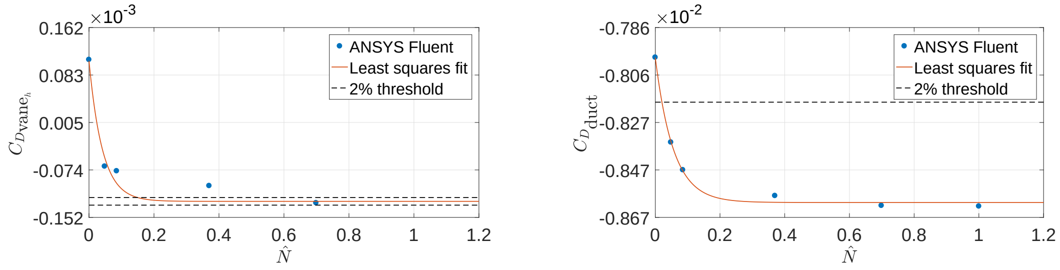

(a) Horizontal vane (b) Duct

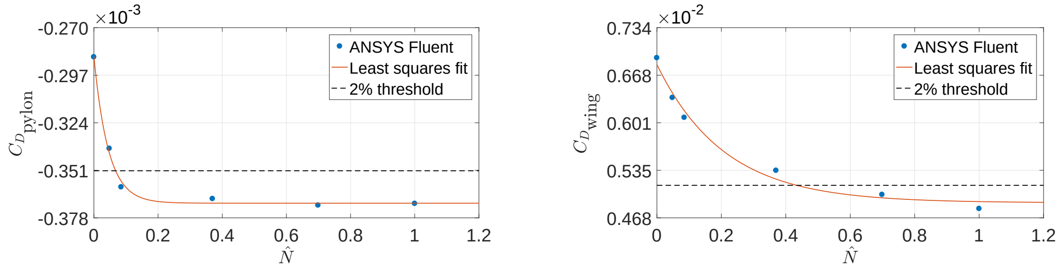

(c) Pylon (d) Wing

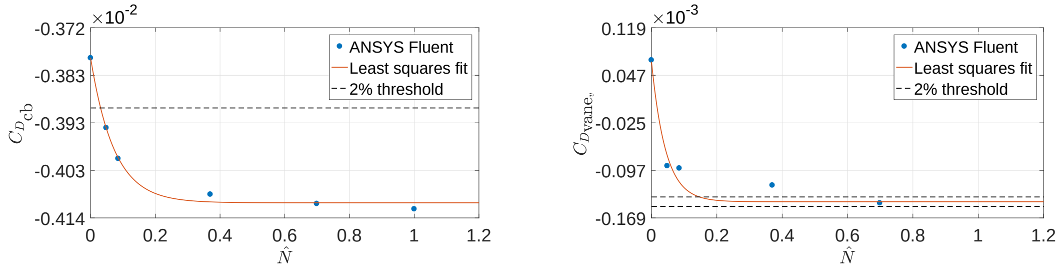

(e) Center body (f) Vertical vane

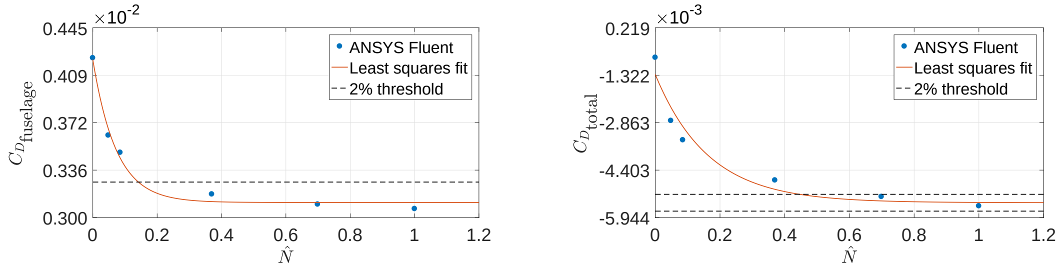

(g) Fuselage (h) Total

Figure 4.9: Pressure drag coefficient as function of mesh density for the subscale simulation, showing mesh convergence

4.3. SOLVER SETUP

An inviscid steady simulation has been performed using the Pressure-Based solver in FLUENT. Air is chosen as the fluid in the domain, with ideal-gas properties. This is done because local supervelocities in the full-scale model are higher than Mach 0.3, which means that compressibility has te be taken into account. When the ideal-gas option is selected, the energy equation is activated which is needed to incorporate the coupling between the velocity of the flow and the temperature. The material properties of the aircraft model is kept at the default aluminum.

	Mesh S1	Mesh S2	Mesh S3	Mesh S4	Mesh S5	Mesh S6
Skewness	0.280	0.277	0.274	0.260	0.251	0.246
Orthogonality	0.850	0.851	0.853	0.860	0.864	0.866

Table 4.4: Mesh quality metrics (average) of the subscale mesh convergence study

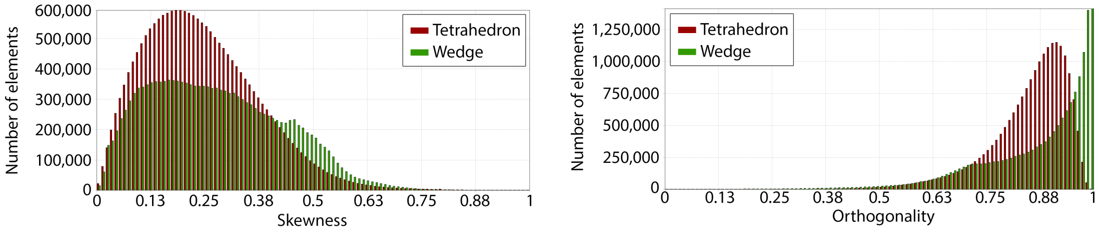

(a) Skewness metric

(b) Orthogonality metric

Figure 4.10: Mesh quality of the full-scale DUUC mesh

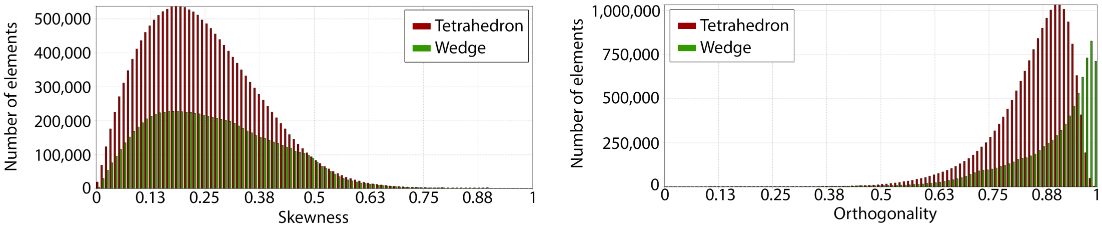

(a) Skewness metric

(b) Orthogonality metric

Figure 4.11: Mesh quality of the subscale DUUC mesh

4.3.1. SOLVER TYPE

Initially, this study was supposed to be performed using a RANS solver with an incorporated turbulence model. The results showed an oscillatory behavior in solution residuals, lift, and drag coefficients on the components around the duct. This is the cause of unsteady separation and/or vortex shedding. In order to take these effect into account, one can either try to increase the numerical dissipation of the steady RANS solution, or another way is to use a time-dependent (transient) algorithm. The first option will most likely not predict the mean flow accurately enough, since it is difficult to include geometric effects on the vortex shedding within the turbulence model. For the second option, the RANS model is changed to an unsteady 3D Navier Stokes model. For aircraft Reynolds numbers, hybrid RANS methods are typically used such as Detached Eddy Simulation (DES). Clusters in the order of thousands of cores, such as the one of TU Delft, are still too small to accurately perform DES for full aircraft.

Above reasoning led to the decision to use the Euler solver in FLUENT. The difference in aerodynamic predictions when switching from RANS to Euler does not necessarily mean that the flight mechanics will be predicted wrong. First of all, the estimated lift does not significantly change because the effective curvature that is 'seen' by the flow is not influenced a lot by the formation of the boundary layer, especially at high Reynolds numbers. Secondly, the effect of drag on the stability and control is significantly less in comparison to the effect of lift. A sensitivity study of the drag on the stability and control characteristics is performed, which can be found in Section 5.7.

4.3.2. BOUNDARY CONDITIONS

The boundary conditions of the fluid domain can be seen in Figure 4.12. The inlet and outlet zones have type pressure-inlet and pressure-outlet respectively. The far sides of the domain located at the top, bottom, and side are pressure-far-fields.

PRESSURE INLET

For the inlet, the Gauge Total Pressure has to be specified, which is the dynamic pressure that is a result of the inlet velocity. By inserting an airspeed of 77 m/s at sea level conditions in Equation (4.3), a Gauge Total

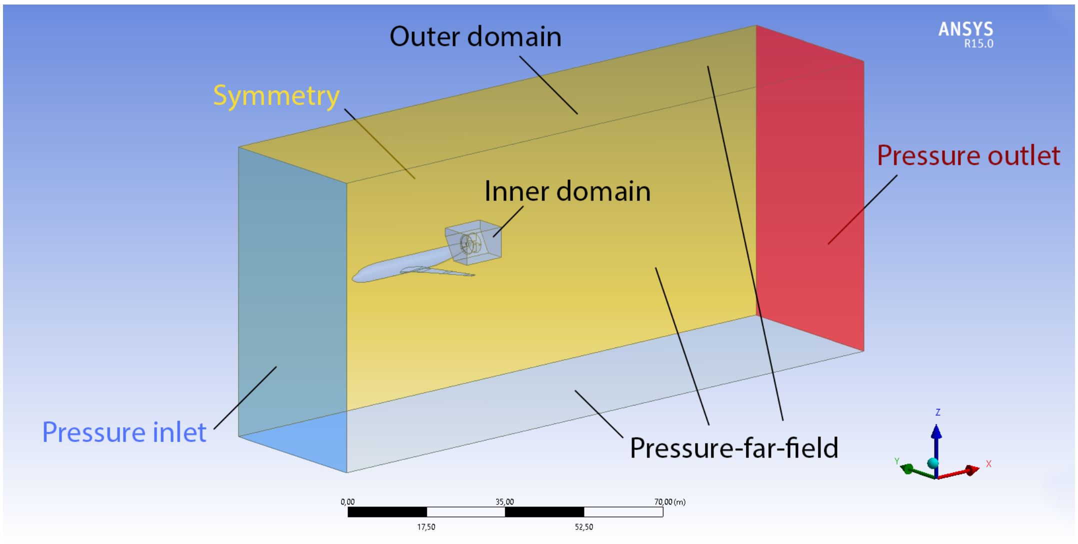

Figure 4.12: Boundary conditions of the fluid domain

Pressure of 3631.51 Pa is obtained.

$$p = {}^{1}\!/_{2}\rho V_{\infty}^{2} \tag{4.3}$$

$$T_0 = T\left(1 + \frac{\gamma - 1}{2} M^2\right) \tag{4.4}$$

Furthermore, the total temperature (T_0) at the pressure inlet has to be specified. The isentropic relation is used to determine the total temperature, which requires the static temperature (T), isentropic expansion factor (γ), and Mach number (M) as shown in Equation (4.4). A γ of 1.4 is assumed for ideal-gas conditions. The airspeed of 77 m/s corresponds to a Mach number of 0.226 at sea level ($T = 288.15\ K$). Inserting these values in Equation (4.4) results in a total temperature of 291.11 K at the inlet.

PRESSURE OUTLET

The static temperature of 288.15 K has to be specified at the pressure outlet as well. The pressure in the slipstream of the propeller is lower than its surroundings, and one can imagine that it takes some time for the energy to be dissipated. This means that the pressure at the outlet may not yet be completely uniform, and therefore the *Average Pressure Specification* is selected.

SYMMETRY PLANE

The model consists of only half of the complete aircraft, because this study will only focus on longitudinal characteristics. This means that the flow around the model can be assumed symmetrical, making the computational process a lot less time consuming. The face that splits the model in half is specified as symmetry plane in FLUENT.

PRESSURE-FAR-FIELD

The faces that form the top, bottom, and side of the domain are set as pressure-far-field. The required inputs for this type are the Mach number and the static temperature. The Mach number was already obtained for the calculations of the pressure inlet boundary condition, namely $M = 0.226$. The static temperature is set on sea level conditions where $T = 288.15\ K$.

FAN

The fan boundary condition in FLUENT requires several inputs that specify the direction of the flow, thrust profile, and swirl properties if needed. For this study, a pure axial flow pattern is assumed and therefore no swirl specification is required. The thrust produced by the actuator disk model is specified by means of a pressure jump, which are related according to Equation (4.5).

$$T = A_{AD}\Delta p \tag{4.5}$$

Where A_{AD} is the actuator disk surface area. The thrust that is produced by the fan is based on the PW127 turboprop featured by the ATR72-600. Figure 4.13 shows a performance plot of the F568-1 propeller, which is installed in the PW127 turboprop engine. The net thrust as function of advance ratio for different altitudes can be seen, from which a thrust of 22 kN per engine is obtained. By using this value in Equation (4.5), a pressure jump of 1675 Pa is found which is implemented in the fan boundary condition.

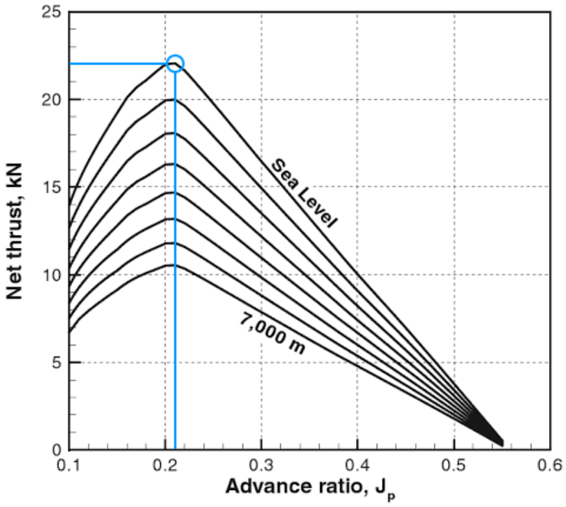

Figure 4.13: Altitude performance of the F568-1 propeller[19]

4.3.3. SOLUTION SETTINGS

A SIMPLE pressure-velocity coupling scheme is used, with discretization settings listed in Table 4.5. A second order interpolation method is selected for the density, momentum, and energy equations, since this is crucial when a tetrahedral mesh structure is used.[20] ANSYS doesn't recommend a second order scheme for the pressure term in case of porous media, jump, fans, etc. which is why a standard scheme is selected here.

Solution setting	**Selected option**
Gradient	Least Squares Cell Based
Pressure	Standard
Density	Second Order Upwind
Momentum	Second Order Upwind
Energy	Second Order Upwind

Table 4.5: Spatial discretization settings used in ANSYS FLUENT

It is important to maintain stability in the solver in order to get to a converged solution. Under-relaxation factors can be used to control this stability, as this will limit the change of the solution of a variable (ϕ) over an iteration. This limitation of the solution is presented in Equation (4.6), where α denotes the under-relaxation factor.

$$\phi = \phi_{old} + \alpha\Delta\phi \tag{4.6}$$

Ideally, one would set a limit such that large changes in ϕ are permitted because this will result in a fast convergence. However, too large changes may cause instability in the numerical scheme and eventually divergence. Such divergence occurred during the CFD analysis of the DUUC, and therefore the under-relaxation factors stated in Table 4.6 were selected.

Under-relaxation factor	**Full-scale**	**Subscale**
Pressure	0.3 (default)	0.3 (default)
Density	1 (default)	1 (default)
Body Forces	1 (default)	1 (default)
Momentum	0.7 (default)	0.7 (default)
Energy	0.7	N/A
Temperature	0.7	N/A

Table 4.6: Under-relaxation factors used in ANSYS FLUENT

Throughout the iteration process it was observed that the temperature solution resulted in extreme temperatures in a large amount of cells in the domain, which did not represent the reality and subsequently led to divergence in the solver. FLUENT has the option where limits can be specified, to control such solution extremes and prevent divergence from happening. The free-stream and inlet temperature were specified at 288.15 K and 291.11 K respectively, from which it can be concluded with quite some confidence that the temperature throughout the domain will not exceed a ± 50 K change. The minimum and maximum static temperature limits are set to 250 K and 350 K respectively.

4.4. AERODYNAMIC RESULTS

In this section, the aerodynamic results are presented that are obtained from a total of 220 simulations (110 for each scale). The aerodynamic coefficients are calculated for an angle of attack sweep of $-12° < \alpha < 15°$ in steps of 3°. For each angle of attack, the elevator is deflected over a range of $-15° < \delta < 15°$ in steps of 3°.

4.4.1. CONVERGENCE CRITERIA

The standard convergence criteria that are set by FLUENT do not necessarily guarantee convergence for all flow cases. Not only should the scaled residuals drop at least three orders of magnitude, the parameters of interest should also reach a certain steady value. As an example, the calculation of the DUUC at an angle of attack of 3° with a vane deflection angle of 0° will be considered from which an adequate number of iterations is determined. The convergence history of the scaled residuals is shown in Figure 4.14a, which include the continuity, velocity components, and energy for 2000 iterations. It can be seen that the residuals drop gradually in magnitude and after about 750 iterations, each scaled residual has dropped three orders of magnitude. From this point on the continuity and velocity components seem to stay quite steady, while the energy term decreases further by another order of magnitude.

Figure 4.14b and Figure 4.14c display the lift and drag coefficients of each component for 2000 iterations. These coefficients are obtained by using the wing planform as a reference area. Also note that these curves are plotted on a logarithmic scale, therefore the absolute value(s) have been considered. This explains the sudden drops towards 0, which in fact means that the sign of the quantity changes from positive to negative or vice versa. According to the scaled residuals, convergence is achieved at around 700 iterations. However, from the lift coefficient of the duct in this case it can be seen that this quantity is still slightly decreasing. Around 1500 iterations it can be said to become steady (similar to the scaled energy residual). It is not certain that every case behaves the same in terms of convergence, and therefore a conservative of 2000 iterations has been chosen as convergence criterion. Furthermore it can be observed that oscillatory behavior in the results can occur. The lift coefficient of the center body seems to oscillate between $5e^{-4}$ and $6e^{-4}$. The final lift and drag quantities are therefore obtained by taking the average of the last 100 iterations.

The subscale simulations are done with a Froude scaled velocity of 18 m/s, which is significantly lower than the full-scale case. This velocity corresponds to a Mach number of about 0.05, at which compressibility effects do not play a role. Therefore the subscale simulations can be performed with a velocity inlet instead of a pressure inlet. Air is modeled as a constant and the energy equation is not required, which has an advantageous influence on the computation time and convergence behavior. The convergence history of the scaled residuals and aerodynamics coefficients of a subscale simulation are shown in Figure 4.15. The lift and drag coefficients of each component are already steady around 700 iterations. Around 1000 iterations, the scaled residuals start to level out and therefore 1000 iterations is chosen as convergence criterion for the subscale simulations.

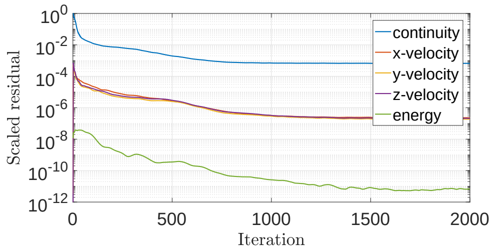

(a) Convergence history of the scaled residuals

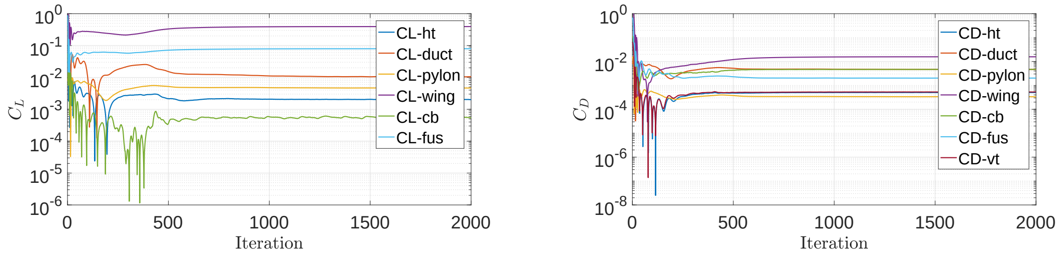

(b) Convergence history of the component lift coefficients

(c) Convergence history of the component drag coefficients

Figure 4.14: Convergence history of the FLUENT calculations for the DUUC at $V_\infty = 77\ m/s$, $\alpha = 3°$ and $\delta_h = 0°$

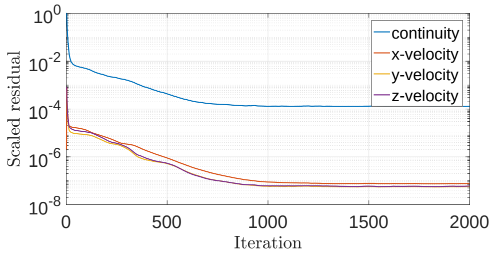

(a) Convergence history of the scaled residuals

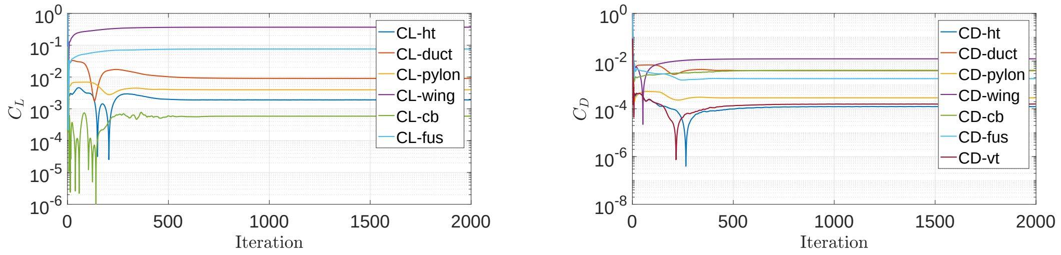

(b) Convergence history of the component lift coefficients

(c) Convergence history of the component drag coefficients

Figure 4.15: Convergence history of the FLUENT calculations for the subscale DUUC at $V_\infty = 18\ m/s$, $\alpha = 3°$ and $\delta_h = 0°$

4.4.2. FULL-SCALE AERODYNAMIC COEFFICIENTS

Within ANSYS FLUENT, forces and moments can be calculated at user specified surfaces and locations. For this study the longitudinal characteristics are of main interest and therefore the following parameters have been monitored: lift coefficient, drag coefficient, and pitching moment coefficient. Note that an Euler solver is used for the calculations and therefore the drag is represented as pressure drag instead of total. Since the moment calculated by FLUENT is based on the pressure distribution without taking into account the effect of the boundary layer formation, it will also slightly differ in reality.

LIFT COEFFICIENT

The first interesting parameter to look at is the lift coefficient on the different components of the aircraft. The reference areas that are selected for these quantities are 103.52 m^2 for the wing and complete aircraft, 11.90 m^2 for the fuselage (frontal area), and 27.70 m^2 for the tail components. The latter is found by taking the projected are of the complete empennage in ANSYS FLUENT. Figure 4.17 shows the lift polars for each component and the effect of the horizontal vane deflection (δ). First of all the lift on the horizontal vane is considered in Figure 4.18a from which it can be seen that the lift coefficient barely changes with increasing angle of attack. The reason for this due to the position of the vane inside the duct. As the angle of attack increases, the flow within the duct is trying to align with the X-axis of the duct. The effective angle of attack at the control vanes is therefore not equal to the inlet angle of attack. A slight increase in lift is observed if α is increased, which can be explained by looking at Figure 4.16. The streamlines and pressure contour are shown for $\alpha = 9°$ and $\alpha = -9°$. By looking at the stagnation point on the horizontal vane for both cases, it can clearly be seen that the streamlines are not fully aligned with the duct axis resulting in the small lift gradient. Furthermore the horizontal vane is expected to generate more lift with higher deflection angles, which is confirmed by the CFD analysis. A similar trend in lift can be seen for the center body in Figure 4.17d.

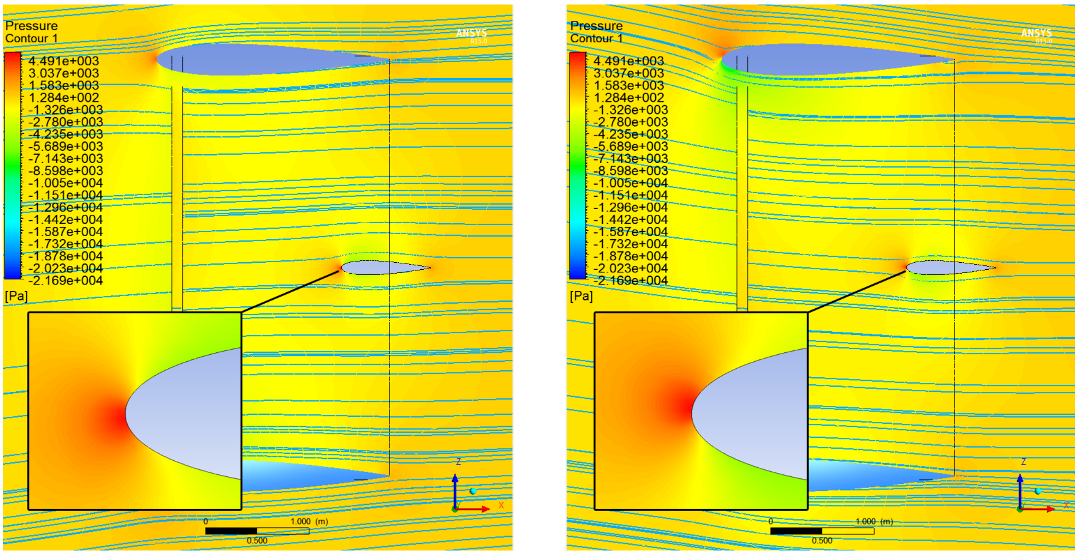
Pressure
Contour 1
4.491e+003
3.037e+003
1.583e+003
1.284e+002
-1.326e+003
-2.780e+003
-4.235e+003
-5.689e+003
-7.143e+003
-8.598e+003
-1.005e+004
-1.151e+004
-1.296e+004
-1.442e+004
-1.587e+004
-1.732e+004
-1.878e+004
-2.023e+004
-2.169e+004
[Pa]
ANSYS
0
1.000 (m)
0.500
Z
X
Pressure
Contour 1
4.491e+003
3.037e+003
1.583e+003
1.284e+002
-1.326e+003
-2.780e+003
-4.235e+003
-5.689e+003
-7.143e+003
-8.598e+003
-1.005e+004
-1.151e+004
-1.296e+004
-1.442e+004
-1.587e+004
-1.732e+004
-1.878e+004
-2.023e+004
-2.169e+004
[Pa]
ANSYS
0
1.000 (m)
0.500
Z
X

Figure 4.16: Streamlines and pressure contour within the duct at $y = -5$ m for (left) $\alpha = 9°$ and (right) $\alpha = -9°$

The lift coefficient of the vertical vane is shown in Figure 4.17b. Note that this regards the force perpendicular to the velocity vector, and not the normal force coefficient that corresponds to the yaw moment. The horizontal vane deflection has minor effect on this coefficient, since it changes the flow field on the left side as well as the right side of the vertical vane (i.e. symmetric flow case). A slight increase in C_L with increasing angle of attack can be seen again, which has the same cause as seen for the horizontal vane.

The duct, pylon, wing, and fuselage are subjected to the free stream with minor disturbances. This means that a typical lift polar is obtained as can be seen in Figure 4.17c, Figure 4.17e, Figure 4.17f, and Figure 4.17g. The horizontal vane deflection clearly has no effect on the fuselage and wing. A small effect is observed on the duct and pylon however. An increase in vane deflection results in a decrease in lift produced by the duct. The supervelocities at the upper surface of the horizontal vane increase as the vane is deflected downward. At the same time, the supervelocities at the lower surface decrease. This means that the difference in pressure between upper region and lower region within the duct becomes larger. The upper region experiences lower pressure, resulting in a larger negative lift force on the upper half of the duct. The higher pressure in the lower region within the duct on the other hand, results in a smaller positive lift force on the bottom half of the duct. Hence, an increase in vane deflection angle leads to a decrease in lift produced by the duct (Figure 4.17c). An opposite trend is seen in Figure 4.17e; higher vane deflection corresponds to more lift on the pylon.

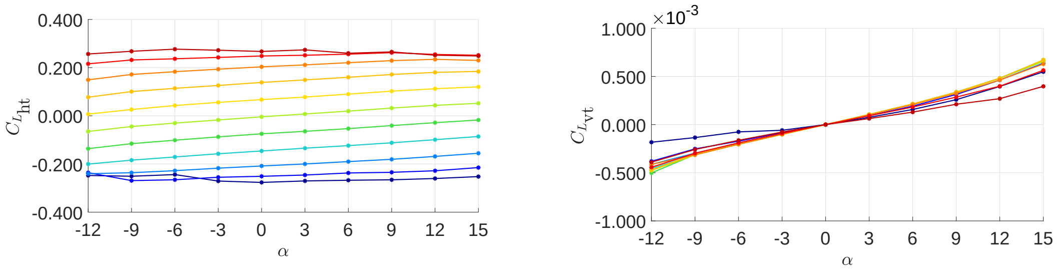

(a) Horizontal vane

(b) Vertical vane

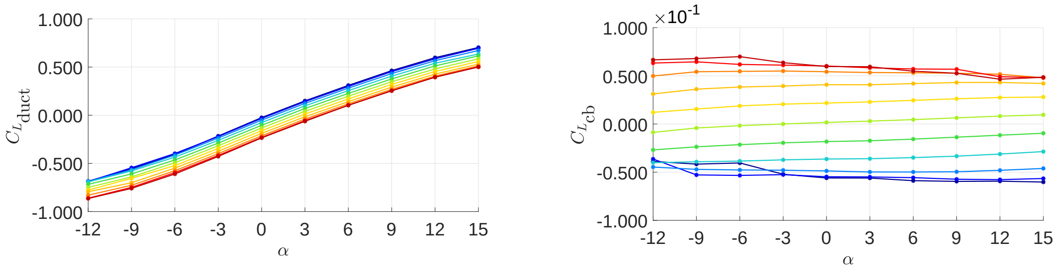

(c) Duct

(d) Center body

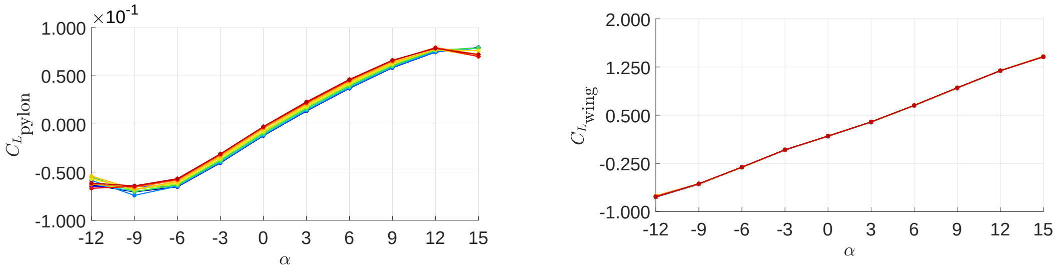

(e) Pylon

(f) Wing

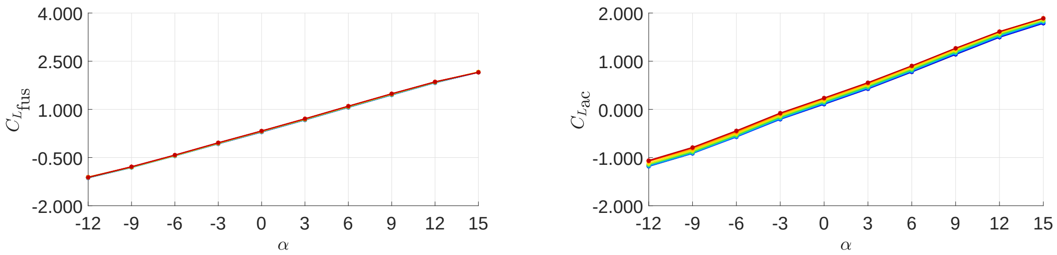

(g) Fuselage

(h) Complete aircraft

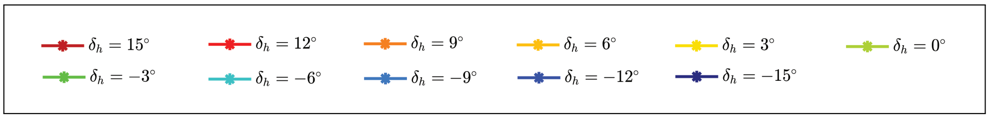

Figure 4.17: Effect of elevator deflection on the lift coefficient of each component of the full-scale DUUC

DRAG COEFFICIENT

The results for the full-scale aircraft's drag coefficients will be discussed now. The drag polars for each component are presented in Figure 4.18. The horizontal vane will again be discussed first. The two key conclusions that can be drawn by looking at Figure 4.18a, are that as the vane deflection increases, the drag curve slope increases, and the angle of attack where minimum drag is obtained decreases. The drag coefficient is only a function of the pressure drag in this study, which means that a larger projected surface area that is 'seen' by the flow corresponds to a higher pressure drag. This can then also be linked to the shift in angle of attack at minimum drag, since this is the configuration when the vane is aligned with the incoming airflow. The direction of the flow within the duct is still depending on the free stream angle of attack as was concluded from Figure 4.16. Therefore if the angle of attack increases, the vane has to be deflected more upward in order to align the flow and thus obtain the minimum drag. Furthermore it can be seen that at $\delta = 0°$ and $\alpha = 0°$, the drag coefficient is approximately 0 as well. The drag polars of the center body (Figure 4.18d) show a similar trend.

The drag coefficient of the vertical vane is very small over the complete range of angle of attack, shown in Figure 4.18b. Moreover, the drag doesn't change significantly with increasing α. Note that although the curves are located in the negative drag region, the skin friction drag contribution will cause the curves to shift into the positive drag region.

The drag polars of the duct show a drag coefficient trend typical for lifting surfaces. The angle of attack for minimum drag shift between 0° and 3° depending on the vane deflection as can be seen in Figure 4.18c. Furthermore it can be seen that at negative angles it would be better in terms of minimal duct drag to fly with more negative elevator deflections and the other way around for positive angles of attack. Furthermore it can be seen that negative drag values are obtained for low angles of attack. Experimental research on ducted propellers shows that the duct can indeed generate a thrust force as a reaction on the propeller.[21] The drag curves obtained for the pylon have a similar trend, shown in Figure 4.18e.

The elevator deflection has no effect on the drag of the wing, which was also found for the lift coefficient. In Figure 4.18f a minimum drag coefficient of about 0.003 can be observed at $-3°$ angle of attack. When looking at the drag polar of the fuselage in Figure 4.18g, a similar parabolic curve is observed. The minimum drag for this component corresponds to $\alpha = 0°$ and the elevator deflection has little to no influence on this parameter.

A total drag coefficient is found by summation of the individual contributions, which is allowed because the wing area is selected as reference area for each component. This total drag is plotted in Figure 4.18h. The shape looks like the parabolic trends found for the duct, wing, pylon, and fuselage for each elevator deflection. In the negative angle of attack regime, a lower (more negative) vane deflection results in higher drag, whereas in the positive angle of attack regime the reverse can be observed. This can be linked back to the trends that were seen for the drag coefficients of the horizontal vane and the center body.

MOMENT COEFFICIENT

The third parameter which plays a role in the stability and controllability of aircraft is the moment coefficient. This quantity is a combination of the aerodynamic forces multiplied by the arm between the center of pressure of these forces and the point where the moment is desired to be measured, which is usually at the quarter chord MAC location. The pitching moment coefficient of the DUUC for different angle of attack and elevator deflections is shown in Figure 4.19, divided into a tail, wing, and fuselage group. The reference y-axes that are defined within FLUENT are located at the quarter chord lengths of the mean aerodynamic chords of the tail and wing for the respective plots in Figure 4.19a and Figure 4.19b. The reference rotation-axis for the fuselage is defined in the center of the fuselage.

The moment coefficient polars of the tail show a positive slope with increasing angle of attack. Experimental data on various aspect ratio ducts show that this slope decreases as the aspect ratio increases.[22] Depending on the horizontal vane deflection, the curves can be located in the positive as well as in the negative half of the plot. The cause of this is simply due to the lift produced by the vane changing direction, as was seen in Figure 4.17a.

Both positive and negative moment coefficient gradients can be seen for the wing. A negative (nose-down) moment is obtained for every angle of attack, which means that the center of pressure of the wing is always behind the aerodynamic center. The center of gravity of the complete aircraft is located at around 18% MAC and therefore the wing will also generate a nose-down moment around the c.g. for the complete α range, which is desired for stability.

A linear relation is observed when looking at the pitching moment coefficient of the fuselage, around its center point. The aerodynamic center of the fuselage is located in front of the center point, which explains the increase in moment as the angle of attack increases.

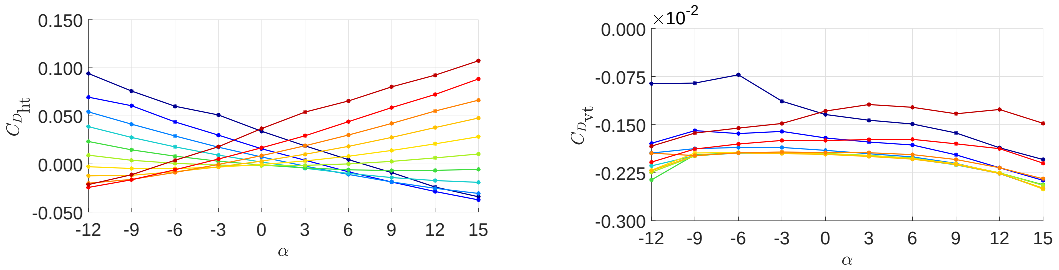

(a) Horizontal vane

(b) Vertical vane

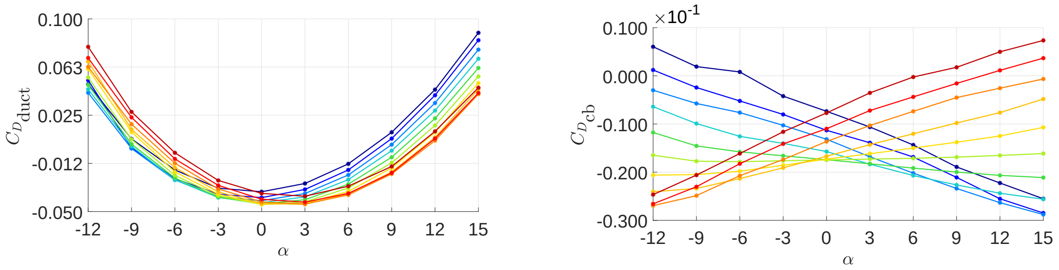

(c) Duct

(d) Center body

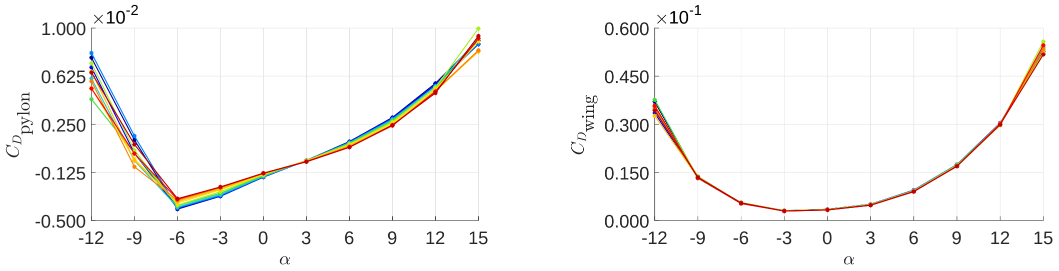

(e) Pylon

(f) Wing

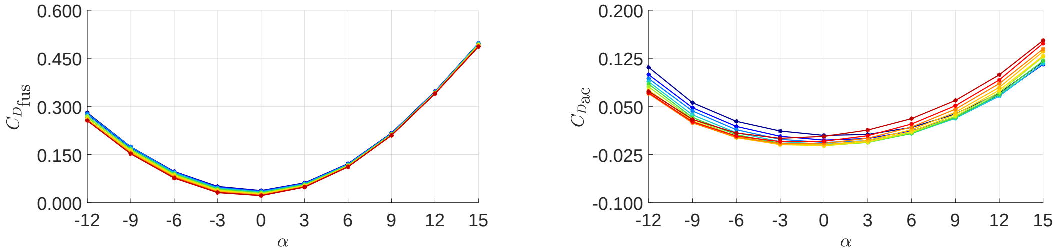

(g) Fuselage

(h) Complete aircraft

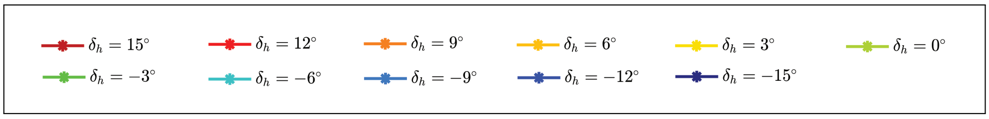

Figure 4.18: Effect of elevator deflection on the drag coefficient of each component of the full-scale DUUC

4.4.3. SUBSCALE AERODYNAMIC COEFFICIENTS

The lift, pressure drag, and moment coefficients of the subscale CFD simulations are presented below.

LIFT COEFFICIENT

Figure 4.21 shows the lift curves of each component of the subscale DUUC aircraft. At first glance it can already be concluded that the lift polars have a similar trend as was seen in the full-scale aircraft. On each component however, a slightly lower lift coefficient is obtained in comparison to the full-scale components.

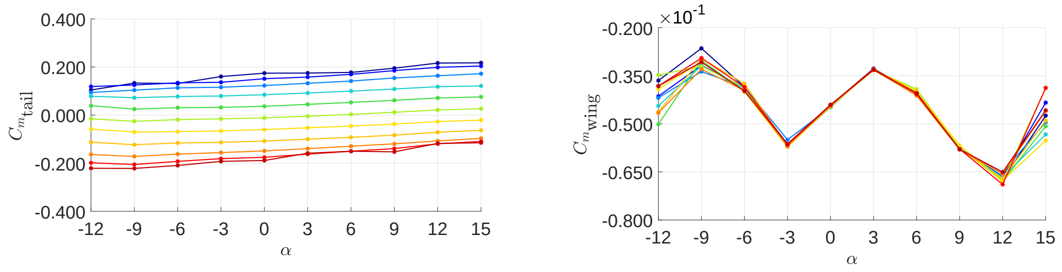

(a) Tail

(b) Wing

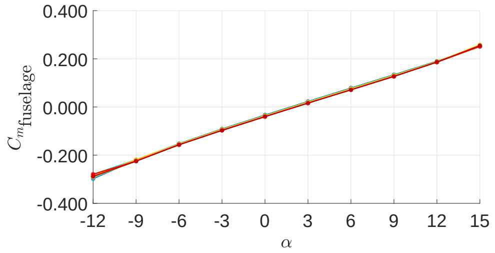

(c) Fuselage

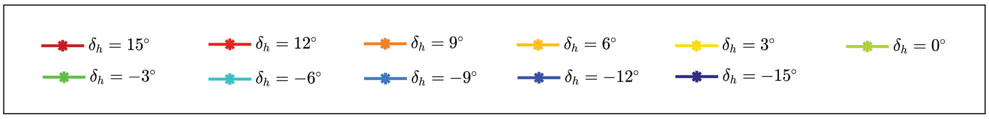

Figure 4.19: Effect of elevator deflection on the moment coefficients of the wing, fuselage, and tail of the full-scale DUUC

This can also be seen when comparing the complete aircraft lift coefficients of Figure 4.17h and Figure 4.21h. For the full-scale lift polar the range of C_L values is found to be between -1.18 and 1.89 (depending on vane deflection), while the subscale aerodynamic results show a range between -0.92 and 1.38. This means that the subscale model estimates the lift coefficient of the full-scale aircraft wrong by about 25%. Due to this difference in magnitude, a different lift curve slope is obtained. The full-scale C_{L_α} is 6.3 rad^{-1} whereas a slope of 5.6 rad^{-1} is found for the subscale aircraft.

In principle, the aerodynamics of the subscale and the full-scale DUUC ought to be the same since the models are inviscid (infinite Reynolds number). The Reynolds number effect that would have been present if the boundary layer is formed can therefore not be designated as the cause for the differences. Part of this difference is there due to the compressibility effect of the full-scale model, which results in a larger lift quantity. However, the biggest cause of the differences is that the solution found with the Euler scheme in FLUENT is not a truly inviscid solution. Numerical perturbations are typically damped in CFD solvers by means of numerical dissipation (i.e. smoothing of strong gradients within the solution). This is especially of importance for the unphysical perturbations of wall bounded flows. Therefore, a so called *artificial viscosity* term is implemented in the numerical scheme.[23] This means that although this study is performed using an inviscid solver, viscous effects are partly taken into account and is still related to the Reynolds number.

A 2D velocity contour plot of the flow field around the horizontal vane has been inspected on both full-scale and subscale levels. Both are compared in Figure 4.20 at a distance of -5 m (-0.275 m on subscale level) away from the symmetry plane. In the full-scale case a very thin region can be spotted aft of the airfoil which very much looks like a boundary layer. By looking at Figure 4.20b however, this phenomenon is much more pronounced and can even be interpreted as laminar separation. A truly inviscid solution would never capture separated flow, "However, the 'numerical viscosity' inherent in inviscid computations sometimes allow such flows to be computed" (Prahbu[24], 2002). One should interpret such a result cautious as it does often not represent physical separation. As a consequence of the numerical laminar separation, the free-stream will experience a reduced effective curvature. This in turn causes a reduction in lift produced by the airfoil. Above mentioned phenomenon is also observed around the other lifting surfaces and is therefore the main reason of the discrepancies between subscale and full-scale lift coefficients.

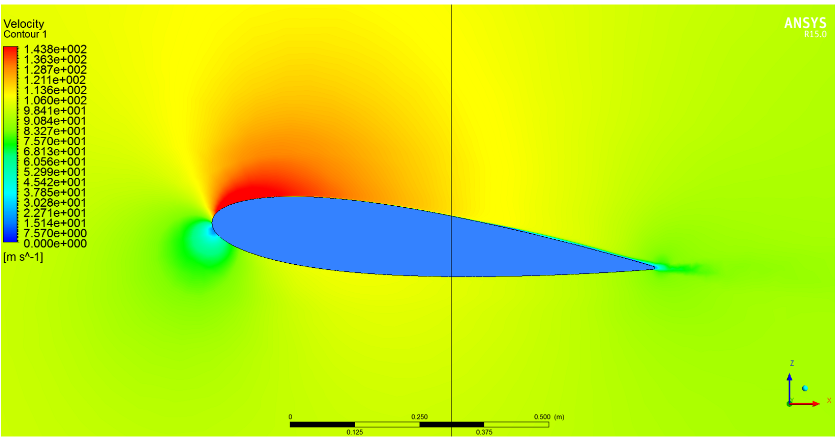

(a) Full-scale ($y = -5\ m$)

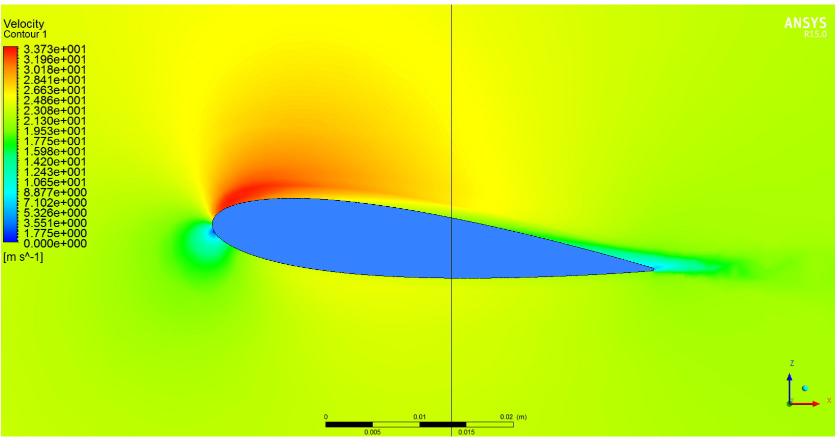

(b) Subscale ($y = -0.275\ m$)

Figure 4.20: Velocity contour around the horizontal vane at $\alpha = 6^\circ$ and $\delta_h = 6^\circ$

DRAG COEFFICIENT

The drag coefficients of the subscale DUUC as function of angle of attack and horizontal vane deflection angle are presented in Figure 4.22. Again the trends of all polars are similar to the ones obtained in the full-scale drag results of Figure 4.18. For example, the drag polars of the duct in Figure 4.22c show a similar shift of the angle of attack at which the minimum drag coefficient is obtained between 0° and 3°. Another observation that can be made is that the magnitude of the subscale drag coefficients is slightly larger in comparison to the full-scale data. The drag contribution of the wing is the main cause of this. Especially at large positive and negative angles of attack, the subscale $C_{D_{\text{wing}}}$ is found to be significantly larger.

MOMENT COEFFICIENT

Since the lift and drag coefficients of the aircraft components were found to match quite well between subscale and full-scale models, the moment coefficient trends are also expected to be similar. In Figure 4.23 these moment coefficients can be inspected. The tail and fuselage moment curves are very similar to the full-scale results in terms of magnitude and slope. The difference in moment coefficient between Figure 4.19b and Figure 4.23b is especially present at angles of attack higher than 6°, where the subscale wing switches from a negative to a positive moment around the quarter chord MAC. As mentioned earlier, the drag coefficients of the wing also differed at high angles of attack. Since the moment coefficient of the subscale wing keeps increasing, the center of pressure is located above the specified moment axis which results in a nose-up pitching moment.

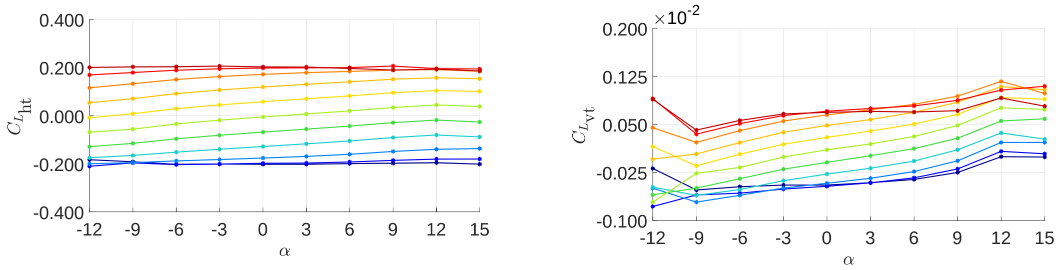

(a) Horizontal vane

(b) Vertical vane

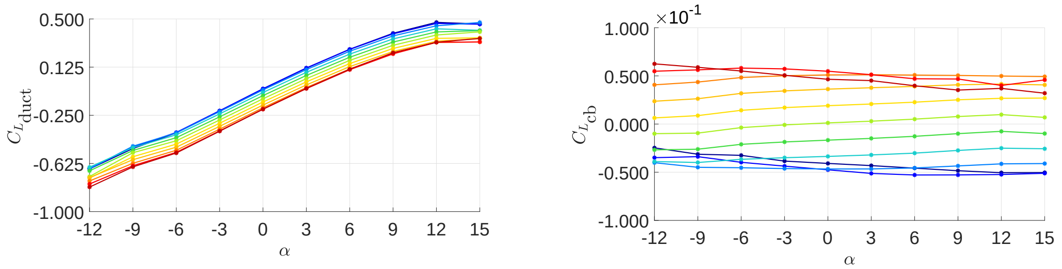

(c) Duct

(d) Center body

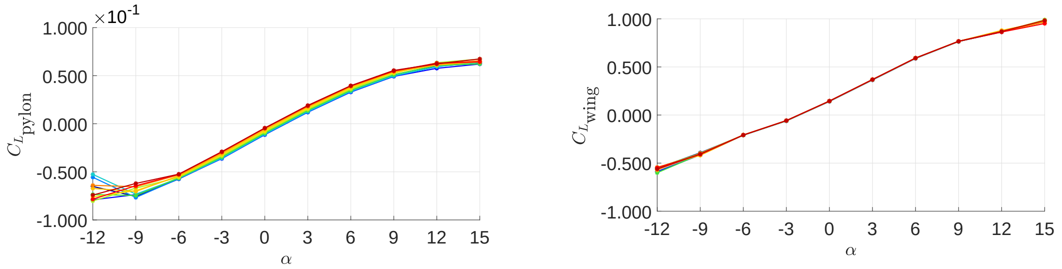

(e) Pylon

(f) Wing

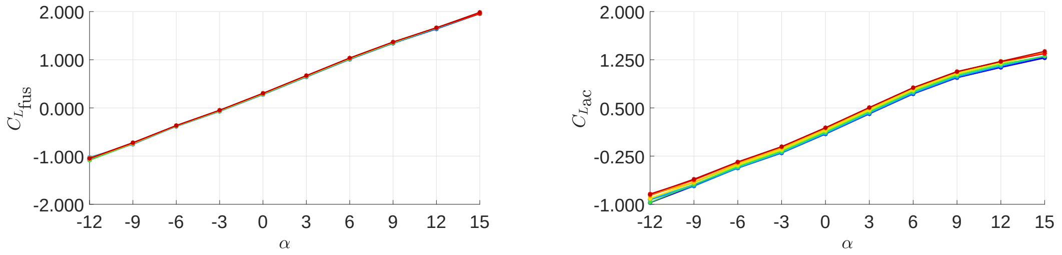

(g) Fuselage

(h) Complete aircraft

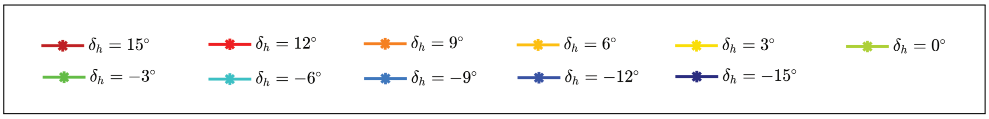

Figure 4.21: Effect of elevator deflection on the lift coefficient of each component of the subscale DUUC

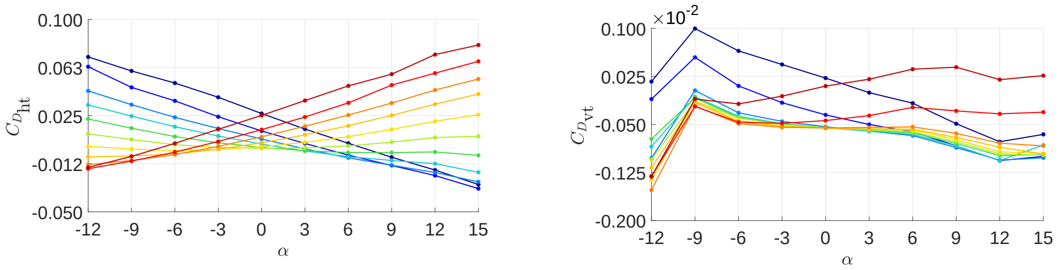

(a) Horizontal vane

(b) Vertical vane

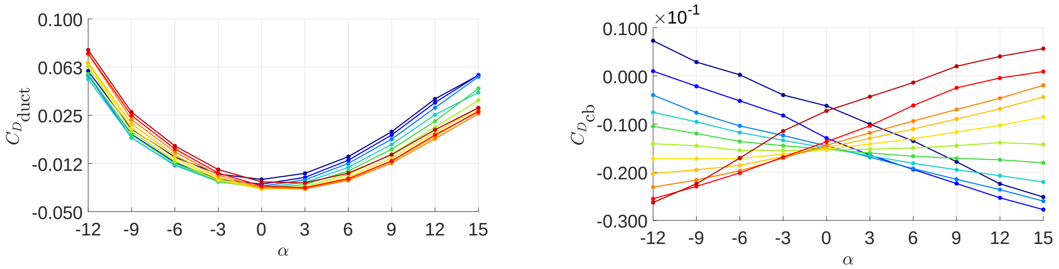

(c) Duct

(d) Center body

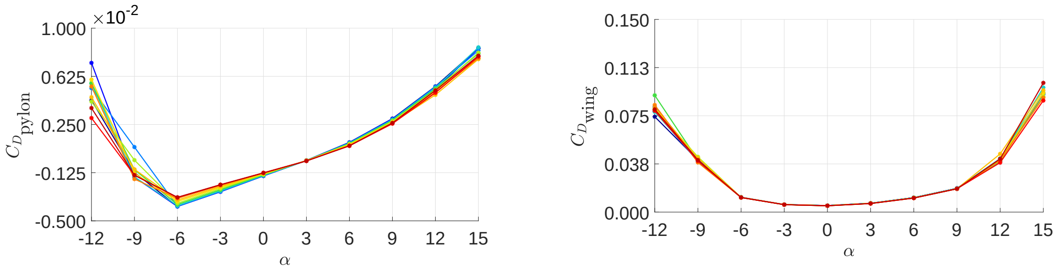

(e) Pylon

(f) Wing

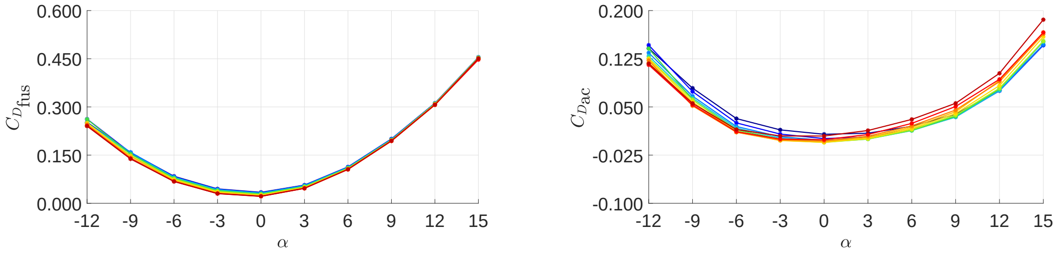

(g) Fuselage

(h) Complete aircraft

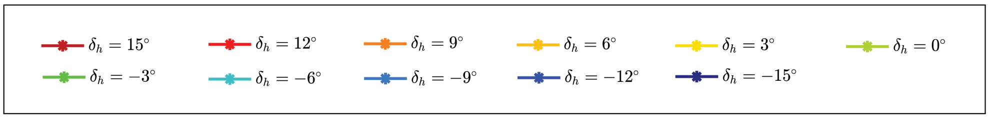

Figure 4.22: Effect of elevator deflection on the drag coefficient of each component of the subscale DUUC

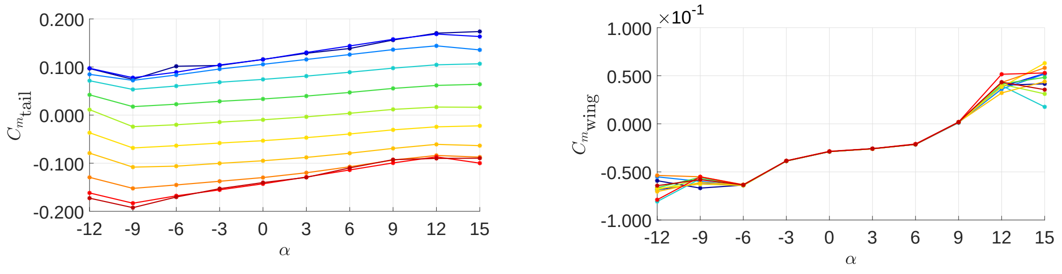

(a) Tail

(b) Wing

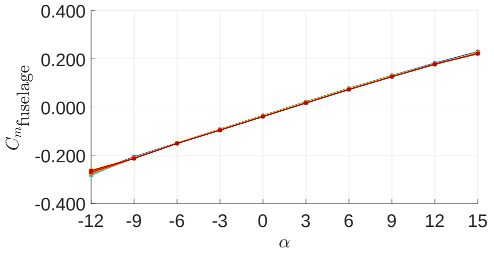

(c) Fuselage

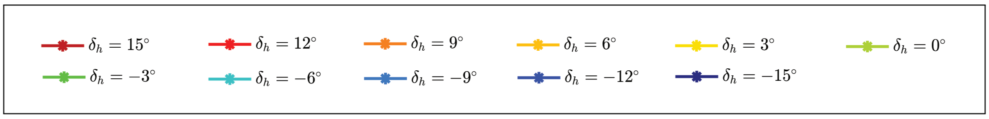

Figure 4.23: Effect of elevator deflection on the moment coefficients of the wing, fuselage, and tail of the subscale DUUC

4.4.4. EFFECT OF THRUST ON AERODYNAMICS

Within PHALANX, the aircraft will be trimmed for certain flight conditions which are set such as the flight velocity and desired pitch angle and pitch rate. The thrust that is required for the trim condition can vary, which in turn has an effect on the aerodynamics of the DUUC. Four thrust settings are analyzed with FLUENT: 0 kN, 7 kN, 15 kN, and 22 kN of which the latter results were shown earlier. The lift coefficient of the full-scale DUUC for this variety of thrust settings is presented in Figure 4.24. The largest effect can be seen on the horizontal vane and center body, which are located directly behind the actuator disk that sets the thrust by a certain pressure jump (and hence velocity increase). Both components show the same trend, namely an increase in lift is seen when the horizontal vane is deflected downward, whilst a decrease in lift is obtained when the vane is deflected upward. From these figures it can be concluded that the elevator effectiveness increases when the thrust and hence velocity increases. Moreover it is observed that the thrust setting has a minor effect on the lift produced by the duct and pylon, and no effect on the wing and fuselage. Therefore, minor change in lift coefficient of the complete aircraft due to thrust is seen (Figure 4.24h).

Figure 4.25 shows the drag coefficient of the components as function of angle of attack, thrust, and elevator deflection. A significant effect of the thrust can be seen on the vanes, the duct, and the center body. As the thrust increases, the drag on the horizontal vane becomes larger in absolute magnitude. The vertical vane, duct, and center body show a decrease in drag as the thrust increases.

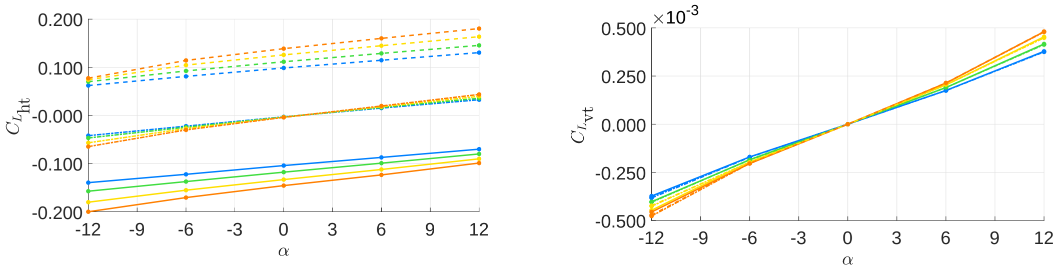

(a) Horizontal vane

(b) Vertical vane

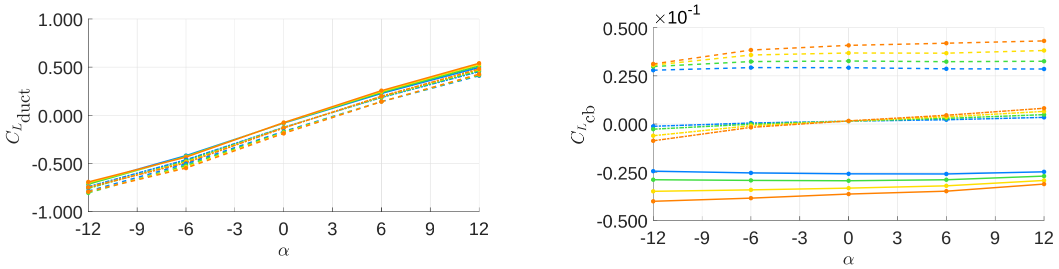

(c) Duct

(d) Center body

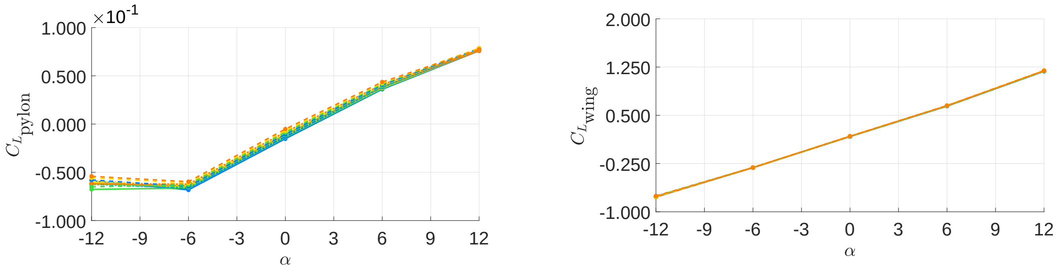

(e) Pylon

(f) Wing

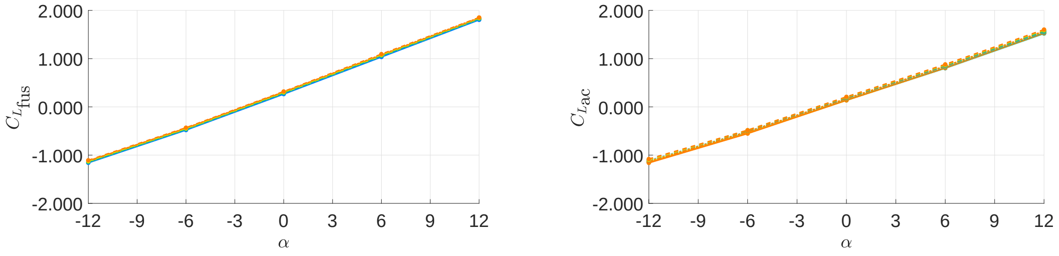

(g) Fuselage

(h) Complete aircraft

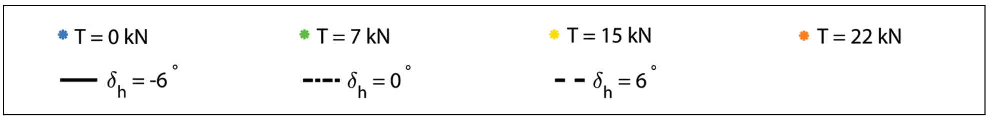

Figure 4.24: Effect of thrust on the lift coefficient of each component

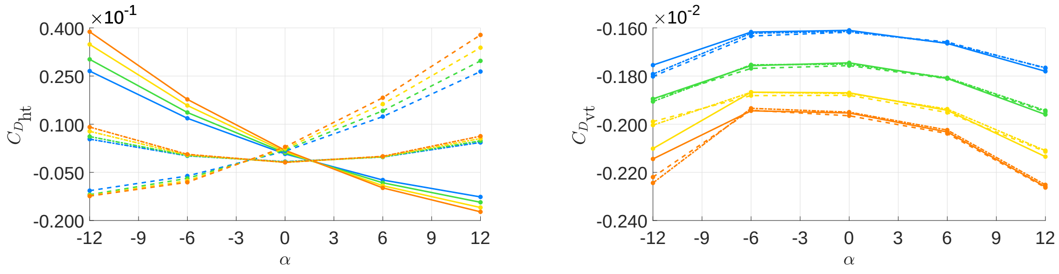

(a) Horizontal vane (b) Vertical vane

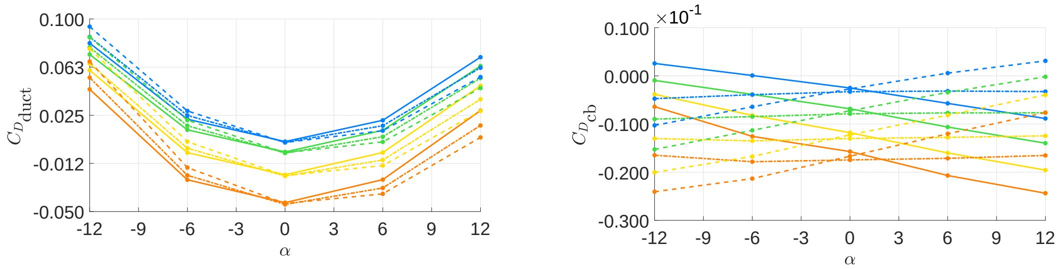

(c) Duct (d) Center body

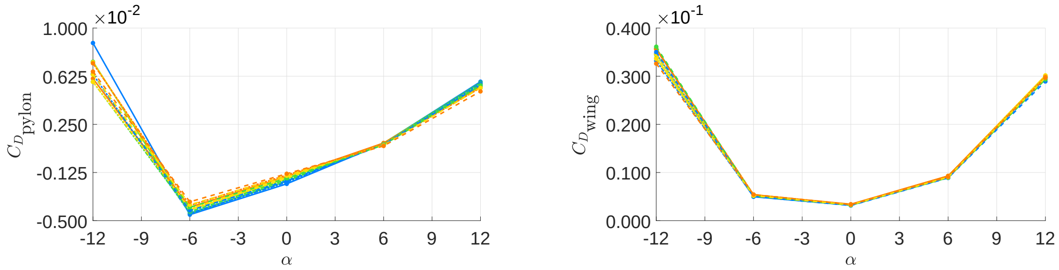

(e) Pylon (f) Wing

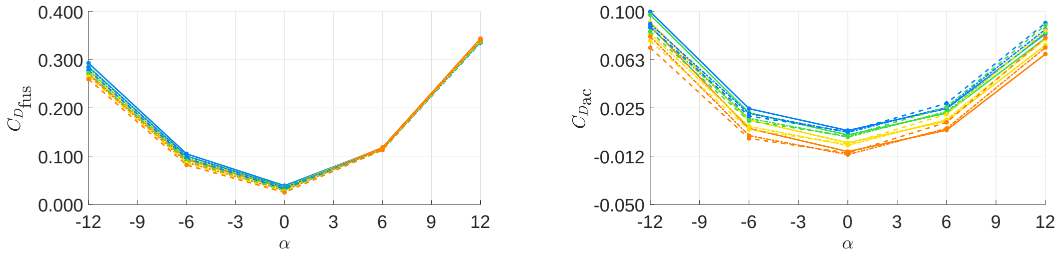

(g) Fuselage (h) Complete aircraft

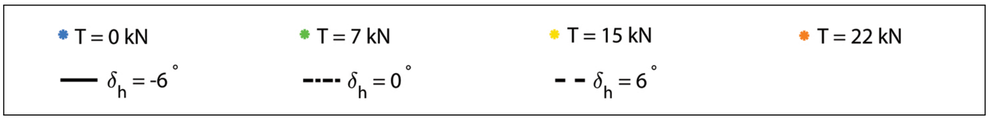

Figure 4.25: Effect of thrust on the drag coefficient of each component

5

FLIGHT MECHANICS SIMULATION

The final step in this research is to simulate the motions of the DUUC on both full-scale and subscale level. Several handling qualities are assessed with the flight mechanics toolbox PHALANX. This program is written in Matlab and Simulink, and uses the Simscape package to model the physical system. In Section 5.1 the structure of the model within PHALANX will be discussed. A weight and balance analysis is performed in Section 5.2 from which the inertia characteristics and key positions such as the center of gravity and neutral point are estimated. After this step, the DUUC can be trimmed and its flight mechanics can be evaluated, which will be explained in Section 5.3. The remainder of this chapter studies the effect of several parameters on the flying qualities of the DUUC. In Section 5.4 the center of gravity location is varied, Section 5.5 discusses the effect of mass and inertia, and finally aircraft scaling is analyzed in Section 5.6.

5.1. INCORPORATION OF THE CFD RESULTS IN PHALANX

PHALANX is built up in a modular fashion, which makes it easy to adapt the programme and incorporate different kind of aircraft. The DUUC model is created by starting from a simple existing BWB model, which is modeled in PHALANX as a body with one reference frame located in its center of gravity. If a certain pitch rate around the center of gravity is to be simulated however, one can imagine the local incidence angle on the nose to be difference than the one on the tail due to the upward or downward motion. This obviously changes the aerodynamics on these locations. The BWB model accounts for this by means of dynamic stability derivatives that have been obtained from the aerodynamic analysis. Such derivatives are not available in the DUUC model since the aerodynamics are only steady-state. Time-dependent simulations would be required, however they are too time consuming. There is a work-around to solve for this lack of information, namely by implementing multiple reference in the DUUC model. These correspond to the locations around which the moments were obtained presented in Chapter 4: quarter chord positions of the wing and tail, and half-way the fuselage. A schematic of the adaptation of the BWB body to the DUUC is visualized in Figure 5.1. The *Body Sensor* in each reference frame measures the local angle of attack, which is then fed back to obtain the corresponding aerodynamics at that point in time.

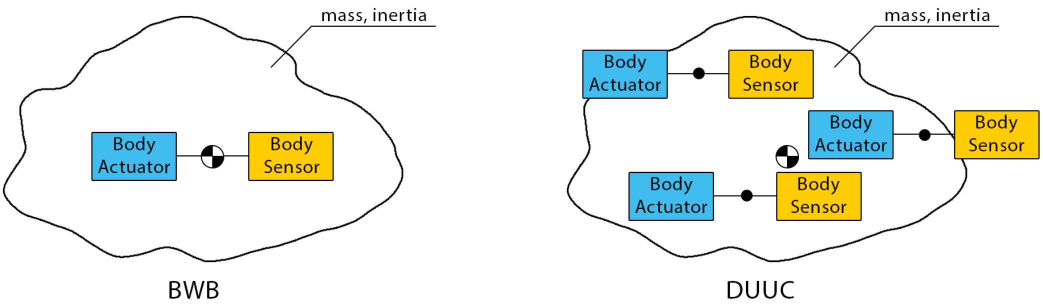

Figure 5.1: Schematic view of the body and its reference axis systems in PHALANX

Besides the aerodynamic data obtained with FLUENT, a drag correction has been implemented in the model that accounts for parasitic drag which the inviscid Euler solver does not calculate. This parasite drag is skin friction present due to the formation of the boundary layer, which can be estimated using flat-plate skin-friction drag coefficients and Raymer's *form factor* (FF) model. Raymer states that the total skin-friction is obtained by the summation of each component as shown in Equation (5.1), where c denotes the component.[25]

$$C_{D_0} = \frac{\sum(C_{f_c} FF_c S_{wet_c})}{S_{ref}} \tag{5.1}$$

The skin-friction coefficient of the components depends on the Reynolds number, the Mach number, and skin roughness (k) which is material dependent. Furthermore, the approximation differs for laminar and turbulent flows as can be seen in Equation (5.2).

$$\begin{aligned} \text{Laminar:} \qquad & C_f = \frac{1.328}{\sqrt{Re}} \\ \text{Turbulent:} \qquad & C_f = \frac{0.455}{(\log_{10} Re)^{2.58}(1+0.144M^2)^{0.65}} \end{aligned} \tag{5.2}$$

It can be assumed that about 30% of the flow is laminar, leading to the skin-friction coefficient relation defined below:

$$C_{f_c} = 0.3C_{f_{lam}} + 0.7C_{f_{tur}} \tag{5.3}$$

Finally, the skin roughness has to be taken into account which is done in the Reynolds number estimation. The lower quantity of the estimations found by Equation (5.4) should be used in Equation (5.2).

$$\begin{aligned} Re &= \frac{\rho V l}{\mu} \\ Re_{\text{cutoff}} &= \begin{cases} 38.21\left(\frac{l}{k}\right)^{1.053}, & \text{if } M \le 0.8 \\ 44.62\left(\frac{l}{k}\right)^{1.053} M^{1.16}, & \text{otherwise} \end{cases} \end{aligned} \tag{5.4}$$

where a skin roughness parameter of $k = 0.634e^{-5}\ m$ is selected, that corresponds to smooth paint.

Different form factor models can be implemented depending on the type of the component and statistical correlations. The following three models are implemented: Equation (5.5) for (swept) planar lifting surfaces, Equation (5.6) for the fuselage and center body, and Equation (5.7) for the duct.

$$FF_w = \left[1 + \frac{0.6}{(x/c)_{max}}\left(\frac{t}{c}\right) + 100\left(\frac{t}{c}\right)^4\right]\left[1.34M^{0.18}(\cos\Lambda_m)^{0.28}\right] \tag{5.5}$$

$$FF_b = 1 + \frac{60}{f^3} + \frac{f}{400} \tag{5.6}$$

$$FF_d = 1 + \frac{0.35}{f} \tag{5.7}$$

where $(x/c)_{max}$ is the chordwise location where the airfoil has its maximum thickness, Λ_m is the sweep at the maximum airfoil thickness line, and f is the fineness ratio of the body defined as:

$$f = \frac{l}{d} \tag{5.8}$$

The maximum thickness location of the airfoil $(x/c)_{max}$ in Equation (5.5) can be assumed depending on the type of airfoil: 0.3 for low-speed airfoils and 0.5 for high-speed airfoils. The form factor and skin-friction coefficient can now be inserted into Equation (5.1), along with the wetted area of each component which is directly obtained in PARAPY or the ANSYS DESIGNMODELER. The reference areas that are used are listed in Table 5.1, which are the same quantities used in the aerodynamic analysis.

Component	**Group**	**Reference area** $[m^2]$	
		Full-scale	**Subscale**
Wing	Wing	103.52	0.3131
Fuselage	Fuselage	11.90	0.0360
Horizontal vane	Tail	27.70	0.0838
Vertical vane			
Duct			
Center body			
Pylon			

Table 5.1: Reference areas used for the calculation of each component skin friction coefficient

5.2. WEIGHT AND BALANCE ESTIMATION

A crucial step in the stability and control analysis is to determine the inertia characteristics and position of the center of gravity of the DUUC. Section 5.2.1 and Section 5.2.2 explain the methods of how this data is obtained.

5.2.1. MASS MOMENT OF INERTIA

No data is available describing the DUUC's inertia characteristics. Therefore an estimation based on statistical data collected by LTH[26] is used, which is presented in Equation (5.9).

$$\begin{aligned} I_{xx} &= k_x^2 b^2 OEM \\ I_{yy} &= k_y^2 l^2 OEM \\ I_{zz} &= 0.96(I_{xx} + I_{yy}) \end{aligned} \tag{5.9}$$

where b and l are the respective span and length of the aircraft and OEM is the operating empty mass. The parameters k_x and k_y are factors that relate mass ratios to the mass moment of inertia and those are calculated with the expressions stated in Equation (5.10).

$$\begin{aligned} kx &= 0.12 + 0.084\left[\frac{FM}{OEM} - 0.66\left(\frac{MTOM}{OEM} - 1\right)\right] \\ ky &= 0.24 - 0.050\left[\frac{FM}{OEM} + 0.20\left(\frac{MTOM}{OEM} - 1\right)\right] \end{aligned} \tag{5.10}$$

Since the scale model of the DUUC is based on a B737-700 model, the inertia is calculated using geometric and mass data of this aircraft. Table 5.2 lists the masses and corresponding mass moments of inertia estimates.[27] The statistical relation in Equation (5.10) takes into account the engine location as fuselage-mounted, which explains the low value of I_{xx}.

Parameter	**Description**	**Unit**	**Value**
$MTOM$	Maximum take-off mass	kg	70,310
OEM	Operating empty mass	kg	38,150
FM	Fuel mass	kg	21,000
I_{xx}	Mass moment of inertia along the x-axis	kgm^2	635,923
I_{yy}	Mass moment of inertia along the y-axis	kgm^2	1,879,631
I_{zz}	Mass moment of inertia along the z-axis	kgm^2	2,414,932

Table 5.2: Mass data and inertia estimation of the full-scale DUUC

5.2.2. CENTER OF GRAVITY AND NEUTRAL POINT LOCATION

The center of gravity of the subscale DUUC is kept more or less at the same distance behind the wing leading edge as the B737-700, in terms of MAC percentage (18.1%). The z-coordinate of the center of gravity location is predicted by decomposing the mass of the DUUC in component contributions. Masses and positions of the fuselage, wing, and ducts are available of the subscale DUUC, from which the center of gravity is calculated using Equation (5.11).

$$z_{cg} = \frac{\sum m_c z_c}{\sum m_c} \tag{5.11}$$

where the subscript c denotes the component. A z_{cg} of -0.0468 m and -0.85 m are found respectively for the subscale and full-scale models (convention as in Figure 5.2).

The z-coordinate of the neutral point is assumed to be located on an axis parallel to the body x-axis, which goes through the center of gravity ($z_{np} = z_{cg}$). The x-coordinate is found by evaluating the moment balance on above defined axis, for two angles of attack. The point where the difference in moment between these two angles is zero is called the neutral point. The subscale and full-scale neutral points are found to be at $x = -1.0$ m and $x = -18.19$ m respectively. Table 5.3 summarizes the CG and neutral point locations of both the subscale and full-scale models.

Location	**Subscale**		**Full-scale**	
	x-coordinate	**z-coordinate**	**x-coordinate**	**z-coordinate**
Center of gravity [m]	-0.913	-0.0468	-16.6	-0.85
Neutral point [m]	-1	-0.0468	-18.19	-0.85

Table 5.3: Center of gravity and neutral point locations of the subscale and full-scale models (see Figure 5.2 for sign convention)

5.3. STABILITY & CONTROL METHODOLOGY

Stability and control is an important aspect in the design process of aircraft. In order to assess those aspects, the forces and moments that act on the system have to be considered. The aerodynamic forces are divided into the three components as described in Chapter 4: wing, tail, and fuselage. A decomposition of these forces can be found in the free body diagram in Figure 5.2. All forces and moments are pointing in the positive direction with respect to the body reference frame: x-axis pointing in the nose direction, z-axis pointing downwards, y-axis going through the right wing.

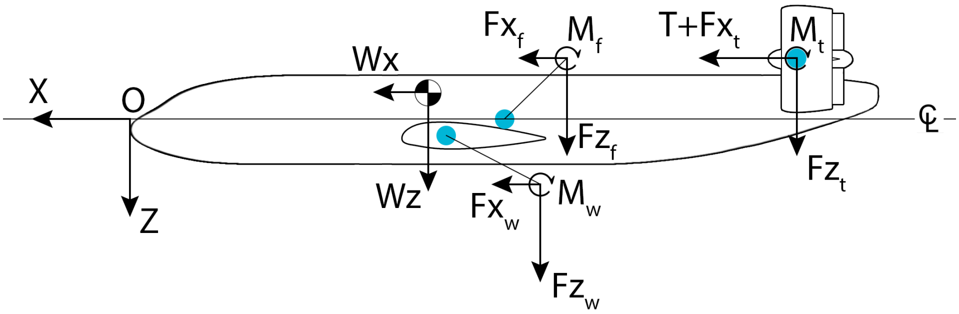

Figure 5.2: Free body diagram of the DUUC with the reference coordinate systems used in PHALANX

In Figure 5.2 it can be seen that the weight is also decomposed. This is done because the body reference frame rotates along with the aircraft but can have a different orientation as the Earth reference frame that is depicted in Figure 5.3. The four angles that are of interest in the longitudinal stability and control analysis are the angle of attack (α), the flight path angle (γ), the pitch angle (θ), and the elevator deflection (δ_h). These angles are defined positive the way they are depicted in the figure. Furthermore the z-axis is pointed upwards, which is convenient to indicate altitude. With the forces, moments, and reference frames defined, the following step is to get equilibrium in each of them by trimming the aircraft. This procedure is explained in Section 5.3.1 along with the linearization method.

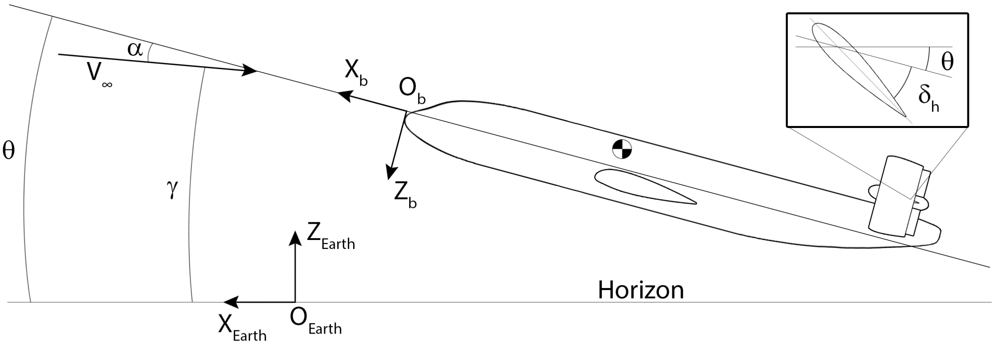

Figure 5.3: Body reference frame with respect to the Earth reference frame

5.3.1. TRIM & LINEARIZATION

A trimmed state is achieved when the forces and moments that act on the body are zero, hence the summation of the forces and moments that are displayed in Figure 5.2 should be equal to zero for the particular flight condition. Equations 5.12 to 5.14 correspond to this case.

$$\sum F_X : F_{X_{wing}} + F_{X_{tail}} + F_{X_{fuselage}} + T - W\sin\theta = 0 \tag{5.12}$$

$$\sum F_Z : F_{Z_{wing}} + F_{Z_{tail}} + F_{Z_{fuselage}} + W\cos\theta = 0 \tag{5.13}$$

$$\begin{aligned}\sum M_Y : & M_{wing} + M_{tail} + M_{fuselage} \\ & + F_{Z_{wing}}(x_{cg} - x_w) + F_{Z_{tail}}(x_{cg} - x_t) + F_{Z_{fuselage}}(x_{cg} - x_f) \\ & + F_{X_{wing}}(z_w - z_{cg}) + (T + F_{X_{tail}})(z_t - z_{cg}) + F_{X_{fuselage}}(z_f - z_{cg}) = 0\end{aligned} \tag{5.14}$$

The trimmed state depends on the forces and moments which are a function of α, δ_h, and throttle. These parameters are varied within PHALANX, and for each configuration a short simulation is performed from which the accelerations in x-direction and z-direction and the pitch rate are derived. The trim routine terminates when either a limit in the control surfaces or throttle is reached, or when the three accelerations are below a certain threshold.

From a trimmed state, the dynamic behavior can be examined by applying a certain input to the aircraft. This time-dependent simulation can be done directly on the non-linear Simulink model. However to quantify the handling qualities, a linear time-invariant (LTI) system is very helpful that can be represented in Matlab in state-space format as shown in Equation (5.15). This procedure is called linearization and is simply obtained with the Matlab command *linmod(sys)*.

$$\begin{aligned}\dot{x} &= Ax + Bu \\ y &= Cx + Du\end{aligned} \tag{5.15}$$

where A is the *state matrix*, B is the *input matrix*, C is the *output matrix*, and D is the *direct matrix*. The state-vector is denoted by x, the input-vector by u, and the output vector by y. The amount of inputs and outputs are 8 and 12 respectively, which can be directly linked to the Simulink model in Figure 5.4. The following inputs can be specified by the user: (1) xalin - lateral stick, (2) xblin - longitudinal stick, (3) xclin - directional stick, (4) xplin - throttle, (5-8) sim_inputs - above 4 inputs when a joystick is connected. The four outputs that are present in Figure 5.4 are each a vector of three parameters: (1) Euler - roll (ϕ), pitch (θ), and yaw (ψ) angle, (2) pqr - angular accelerations around the roll (p), pitch (q), and yaw (r) axes, (3) Vb - velocity components in the body reference frame, (4) Xe - position of the model w.r.t. the Earth reference frame.

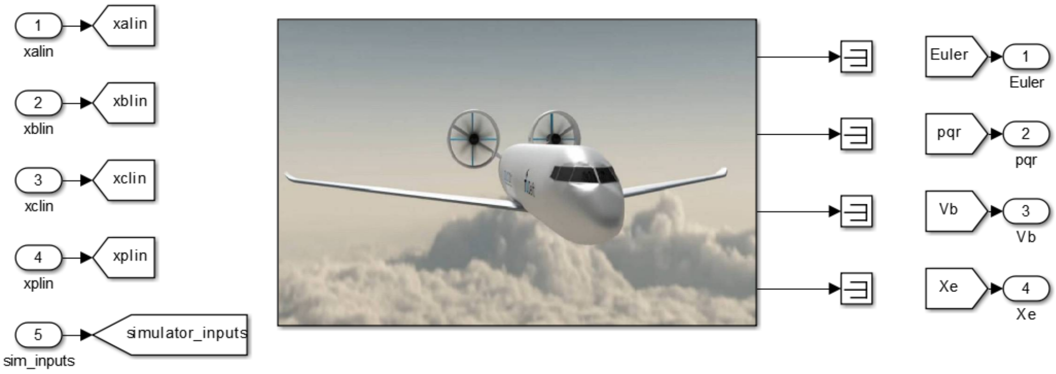

Figure 5.4: Top level structure of the flight mechanics model in PHALANX

Since the longitudinal motion is of main interest, the full order linear model of the DUUC can be reduced by eliminating the states that do not (significantly) affect this motion. Four states remain for the reduced longitudinal model, namely the pitch angle, pitch rate, and velocities in body x-, and z-direction. The following longitudinal reduced state-space system is obtained:

$$\begin{bmatrix} \ddot{x} \\ \ddot{z} \\ \dot{\theta} \\ \dot{q} \end{bmatrix} = \begin{bmatrix} A_{11} & A_{12} & A_{13} & A_{14} \\ A_{21} & A_{22} & A_{23} & A_{24} \\ 0 & 0 & 0 & 1 \\ A_{41} & A_{42} & A_{43} & A_{44} \end{bmatrix} \begin{bmatrix} \dot{x} \\ \dot{z} \\ \theta \\ q \end{bmatrix} + \begin{bmatrix} B_1 \\ B_2 \\ 0 \\ B_4 \end{bmatrix} \delta_h \tag{5.16}$$

$$\begin{bmatrix} u \\ w \\ \theta \\ q \end{bmatrix} = \begin{bmatrix} C_{11} & C_{12} & C_{13} & 0 \\ C_{21} & C_{22} & C_{23} & 0 \\ 0 & 0 & 1 & 0 \\ 0 & 0 & 0 & 1 \end{bmatrix} \begin{bmatrix} \dot{x} \\ \dot{z} \\ \theta \\ q \end{bmatrix} + \begin{bmatrix} 0 \\ 0 \\ 0 \\ 0 \end{bmatrix} \delta_h \tag{5.17}$$

Note that the pitch angle and pitch rate in the output vector are equal to their respective states, whereas the u and w velocities are not the same as the velocity components of the body $\dot{x}$ and $\dot{z}$ (in the Earth reference frame, see Figure 5.3).

5.3.2. LONGITUDINAL HANDLING QUALITIES

When a step input is applied on the horizontal vane, the aircraft will experience a disturbed motion that is built up from two periodic motions, namely the short period and the phugoid. The latter motion corresponds to the long period oscillation. These motions can be assessed by looking at their eigenvalues. The natural frequencies and damping ratios of each pole of a dynamic system can be obtained by using the *damp(sys)* command in Matlab. The eigenvalues of the system are obtained by setting the denominator of the pitch transfer function equal to zero. These eigenvalues consist of a real and an imaginary part that correspond to the damping ratio and natural frequency as shown in Equation (5.18).

$$\lambda_{1,2} = -\zeta\omega_n \pm i\omega_n\sqrt{1-\zeta^2} \tag{5.18}$$

The frequency and damping ratio of each eigenvalue can be found with Equation (5.19) and Equation (5.20).

$$\omega_n = |\lambda| = \sqrt{Re(\lambda)^2 + Im(\lambda)^2} \tag{5.19}$$

$$\zeta = \frac{-Re(\lambda)}{|\lambda|} \tag{5.20}$$

5.4. EFFECT OF CENTER OF GRAVITY LOCATION ON FLIGHT MECHANICS

Changing the position of the center of gravity can have a beneficial as well as an adverse effect on the stability and control of an aircraft. In general, the CG is located in front of the neutral point to ensure sufficient stability. However, too much stability leads to less controllability and should also be avoided. The relation between the CG and neutral point is called the static margin (SM), as shown in Equation (5.21). The convention is chosen such that a positive static margin means positive stability.

$$SM = \frac{x_{np} - x_{cg}}{\bar{c}} \tag{5.21}$$

The static margin with which previous results were obtained is about 0.40, which is very large with respect to a typical SM of 0.05-0.10.[25] In this section the effect will be discussed of reducing this margin to a more conventional one, or even to a negative value (unstable). For this analysis, a flight speed of 80 m/s is selected which corresponds to a realistic approach speed of the full-scale DUUC.

5.4.1. EFFECT OF CG LOCATION ON THE TRIM SOLUTION

An analysis has been performed to the sensitivity of the trim angles to a shift in CG location, by bringing the CG closer to the neutral point in PHALANX. The initial estimate of the CG location at 18.1% MAC is set as the most forward CG position. The trim solution for this case is shown in Figure 5.5a, denoted by $SM = 0.40$. Furthermore the curves corresponding to a static margin of 25%, 10%, and 2% MAC can be inspected. It can be seen that as the SM decreases, the required elevator deflection angle to trim the vehicle decreases as well. This means that the elevator effectiveness increases and the aircraft becomes more controllable.

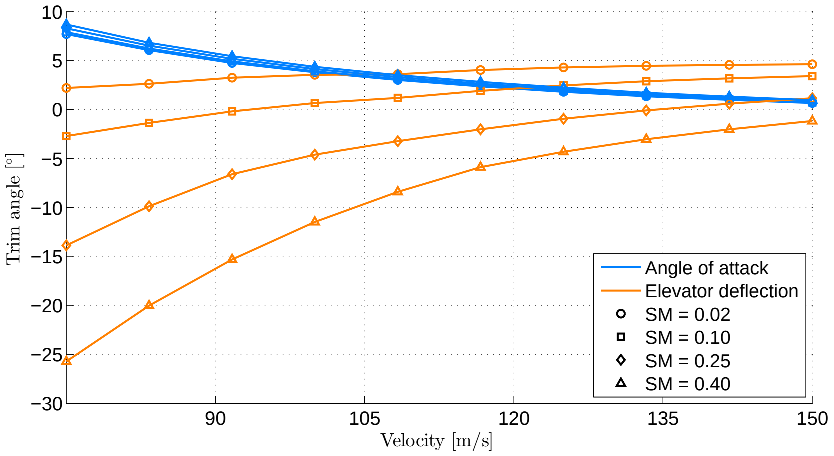

(a) Stable CG locations

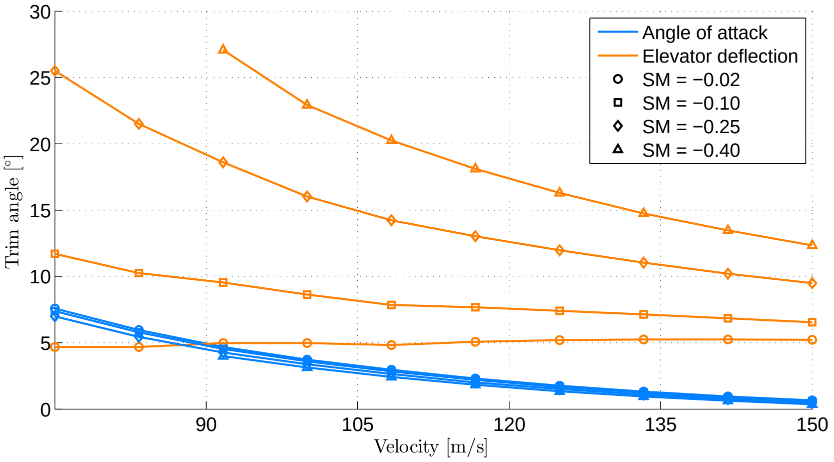

(b) Unstable CG locations

Figure 5.5: Effect of the CG location on the trim solution

A reverse trend in the elevator trim angle as function of flight speed can be seen if the CG is located at an unstable static margin. The curves corresponding to a static margin of -2%, -10%, -25%, and -40% are shown in Figure 5.5b. Furthermore it can be concluded that both stable and unstable CG locations do not influence the trim angle of attack significantly.

5.4.2. EFFECT OF CG LOCATION ON THE LONGITUDINAL STATIC STABILITY

The time response to a certain change in angle of attack has been analysed for both the stable and unstable CG locations, shown in Figure 5.6a and Figure 5.6b respectively. At the most forward CG location a very rapid response back to the original trim angle of attack can be seen. This response is so rapid that it causes an overshoot before it returns to the original angle after about 5 seconds. As the static margin decreases, the response gets slower which reduces the overshoot but at the same time means that the stabilization of the aircraft requires more time. As the neutrally stable CG location is neared, the aircraft returns gradually to its trimmed state as can be seen in the curves corresponding to $SM = 2\%$ and $SM = -2\%$. If the CG is located even further aft, the initial response seems stable for the first 1-2 seconds. However, this initial stabilizing effect is followed up very quickly by divergence. This can be a very dangerous situation for the pilot, since he initially senses a stable response.

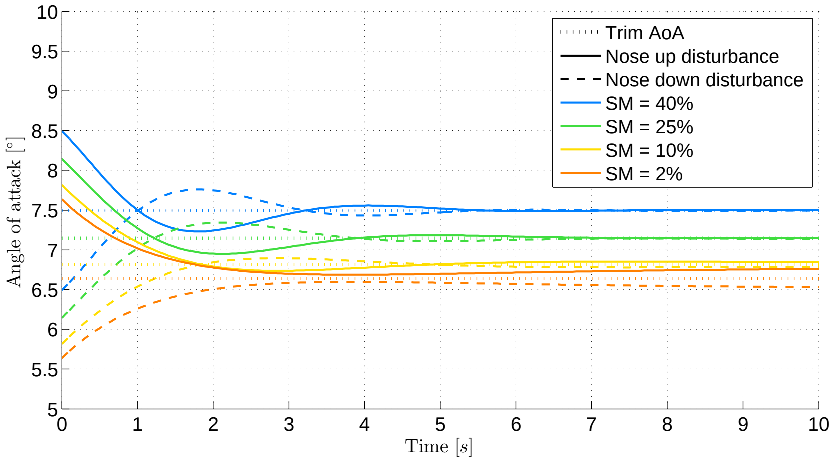

(a) Stable CG locations

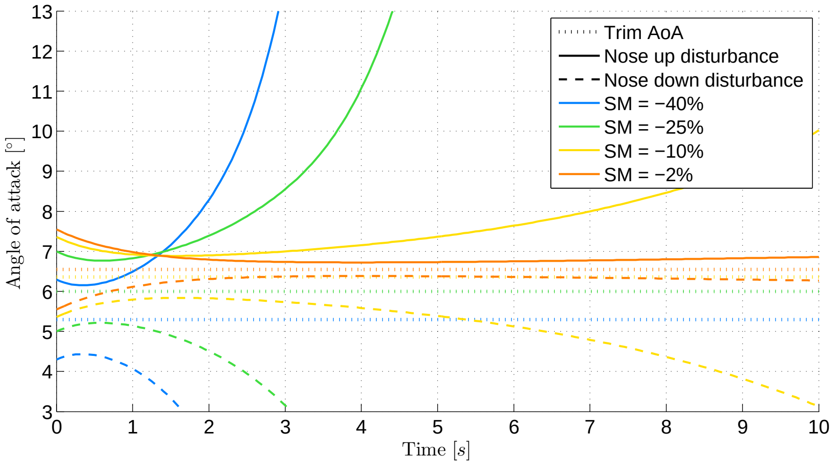

(b) Unstable CG locations

Figure 5.6: Effect of the CG location on the static stability at $V = 80\ m/s$

5.4.3. EFFECT OF CG LOCATION ON THE LONGITUDINAL EIGENVALUES

The phugoid and short period handling qualities are assessed by evaluating the eigenvalues of the system as was explained in Section 5.3.2. A typical way of visualizing the effect of a certain parameter on the frequency and damping parameters is by plotting these eigenvalues on the s-plane.

Figure 5.7a shows the longitudinal short period eigenvalues for a range of static margins between -25% and +40% MAC. The arrows indicate an aft shift of the center of gravity. The stable CG locations show eigenvalues that consist of an imaginary part, and are therefore oscillatory. Furthermore they all contain a negative real part, indicating stability (positive damping). When the static margin is approximately 0%, the critical damping ratio is reached ($\zeta_{sp} = 1$) and increases beyond this ratio as the CG is shifted even more aft. At this point the eigenvalues have lost their imaginary parts, and two real eigenvalues are obtained.

The same analysis has been performed on the much smaller eigenvalues of the phugoid motion. At a stable SM of +40%, the eigenvalues lie on $\pm 0.16j$, which means that the damping ratio is 0 (undamped). As the CG is shifted aft, the real part of the eigenvalues becomes positive resulting in an unstable phugoid. Between a static margin of 2% and -2%, the motion becomes stable again. Between -2% and -2.2% SM, the complex branches merge together on the real axis. Another branch can be seen around a static margin of -2.5%, where an aft shift in CG results in an oscillatory phugoid again.

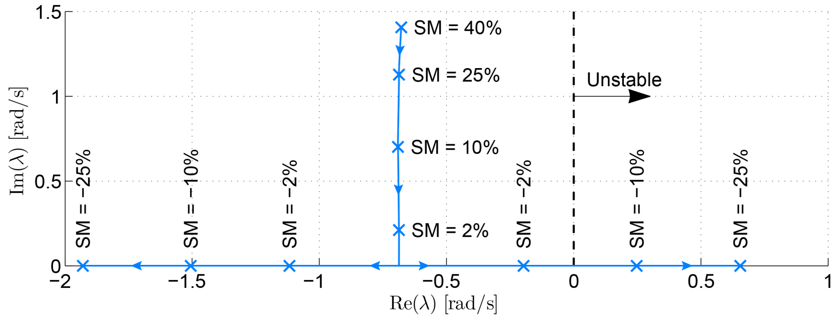

(a) Short period eigenvalues

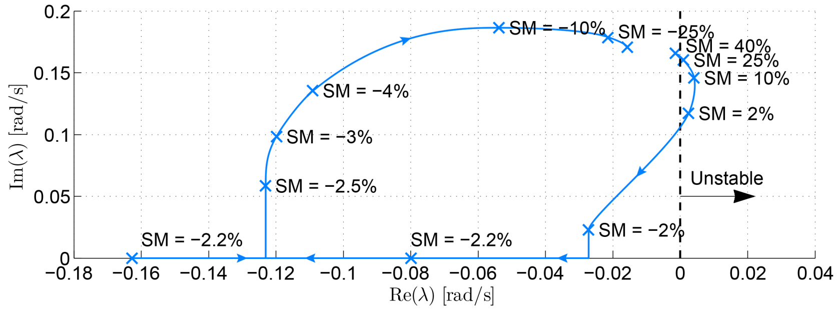

(b) Phugoid eigenvalues

Figure 5.7: Longitudinal eigenvalues for various CG locations at $V = 80\ m/s$

5.4.4. EFFECT OF CG LOCATION ON THE TAKE-OFF ROTATION

A range of step inputs is applied to the reduced longitudinal pitch transfer function, which corresponds to elevator deflections between -20 and 20 degrees. Figure 5.8a shows the instantaneous pitch acceleration that is a result of these step inputs for the stable static margin cases. The dashed line indicates a pitch acceleration of zero, hence no control input is applied. The points where the curves intersect this dashed line are thus the elevator trim angles. It is obvious that a higher elevator deflection results in a larger pitch acceleration, however the maximum quantity depends on the trimmed (initial) deflection as well. Consider a SM of 10% where the trim line is intersected at approximately $\delta_h = 0^\circ$. A point symmetric trend can be observed with the point of symmetry located in the origin. A maximum instantaneous pitch acceleration of about $\pm 15\ ^\circ/s^2$ is obtained where the sign depends on the direction of the elevator. A more forward CG location means a larger negative elevator trim angle. This reduces the maximum input that can be applied towards the -20 degree limit. However, the margin between trim angle and +20 degree limit increases, resulting in larger negative pitch accelerations that can be achieved. This relationship between static margin and maximum instantaneous pitch acceleration is derived from Figure 5.8a as an upward or downward shift in the curve.

The pitch accelerations for the unstable static margins are shown in Figure 5.8b. The curve keeps on shifting upwards as the CG shifts more aft. Larger pitch up accelerations can be achieved with unstable static margins, however nose-down accelerations are limited to somewhere between -10 and +10 $^\circ/s^2$.

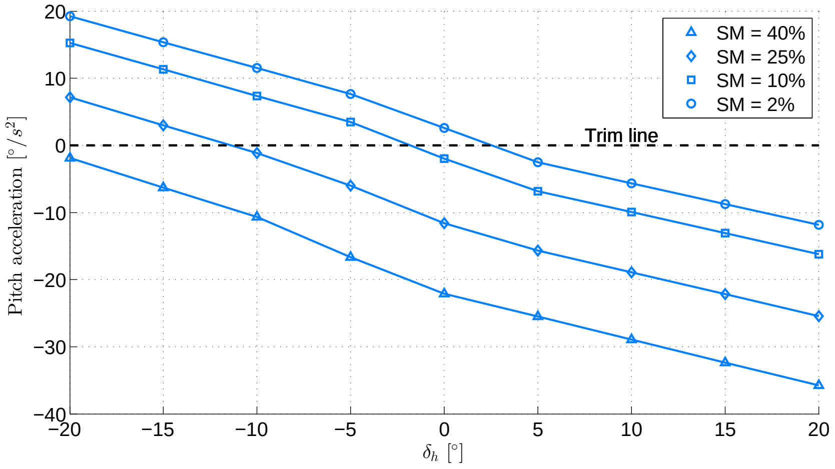

(a) Stable CG locations

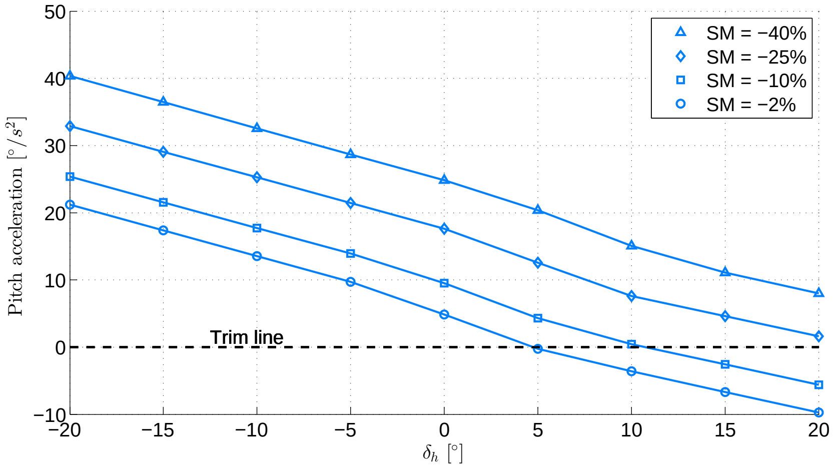

(b) Unstable CG locations

Figure 5.8: Effect of the CG location on the instantaneous pitch acceleration at $V = 80$ m/s

5.5. Effect of Inertia on Flight Mechanics

To investigate the effect of mass on the flying qualities, both the mass and inertia quantities have to be altered in the model. Here it is assumed that the geometry (lengths, areas) and the mass distribution remains the same, which means that a change in mass will also influence the mass moment of inertia. If a mass is for example scaled by a factor of 0.5 and its location remains the same, the mass moment of inertia will scale with the same factor of 0.5. This section will discuss the effect of this factor, denoted $mScale$, with the CG location fixed at $SM = 10\%$.

5.5.1. Effect of Inertia on the Trim Solution

As the weight of an aircraft increases, the lift required to trim in horizontal flight should increase as well. Since this study does not take high lift devices into account, the only option that PHALANX has is to increase the angle of attack. If this angle increases however, the weight component in body X-direction increases which is compensated for by providing more thrust. This in turn introduces a stronger nose down moment, resulting in a larger (negative) elevator deflection. The trim solution for a range of flight speeds can be inspected in

Figure 5.9, which confirms above reasoning.

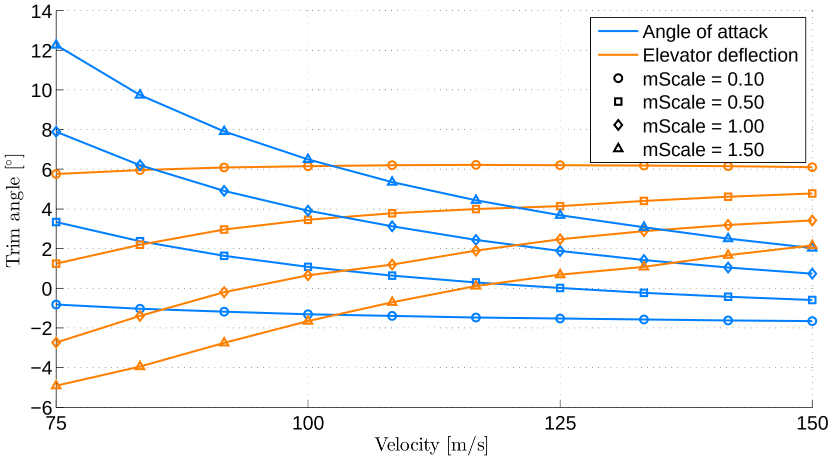

Figure 5.9: Effect of mass and inertia on the trim solution

5.5.2. EFFECT OF INERTIA ON THE LONGITUDINAL STATIC STABILITY

It was assumed that the mass distribution remains constant while changing the mass and inertia characteristics of the DUUC. This means that the center of gravity location and thus static margin stays 10% independent of $mScale$. Therefore the response to a nose up or nose down disturbance is stable for the complete range of mass scale factors as can be seen in Figure 5.10. The inertia does have an effect on the response time. The higher the mass and inertia of an aircraft, the slower its response is. From the figure it can be seen that the time it takes to return to the trim angle of attack after a one degree disturbance is in the order of tenths of a second for a very low mass, and in the order of seconds for heavy aircraft.

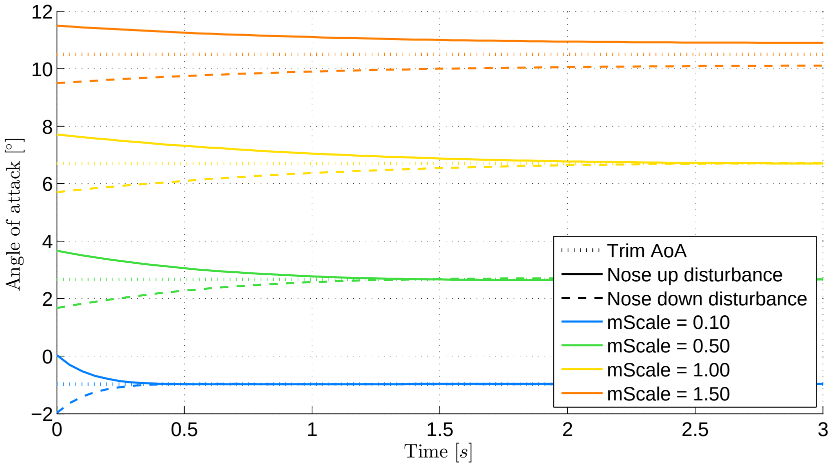

Figure 5.10: Effect of mass and inertia on the static stability at $V = 80\ m/s$

5.5.3. EFFECT OF INERTIA ON THE LONGITUDINAL EIGENVALUES

The longitudinal eigenvalues of the short period and phugoid modes are shown in Figure 5.11a and Figure 5.11b respectively. Both figures show a decrease in damping ratio as the mass scaling factor increases. The short period is close to being critically damped, with a damping ratio of 0.9969 for $mScale = 0.05$ and this damping ratio decreases to about $\zeta_{sp} = 0.80$ for $mScale = 1.25$. For this range of mass scales the short period is a stable mode. The phugoid eigenvalues on the other hand cross the instability border between $mScale = 0.50$ and $mScale = 1.00$. A lighter aircraft is thus found to be more stable, but the response is also faster which is derived from the frequency of the eigenvalues. This faster response was also found while considering the longitudinal stability.

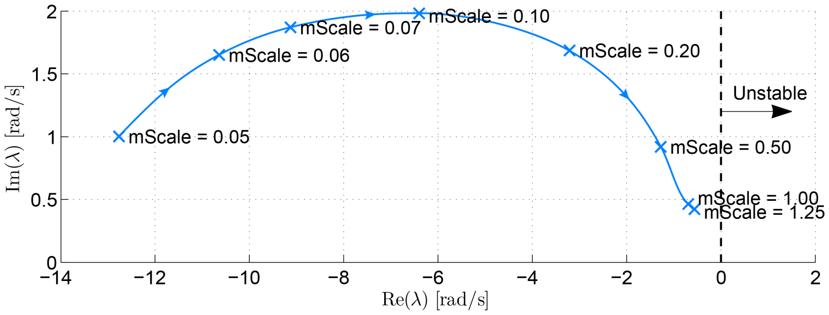

(a) Short period eigenvalues

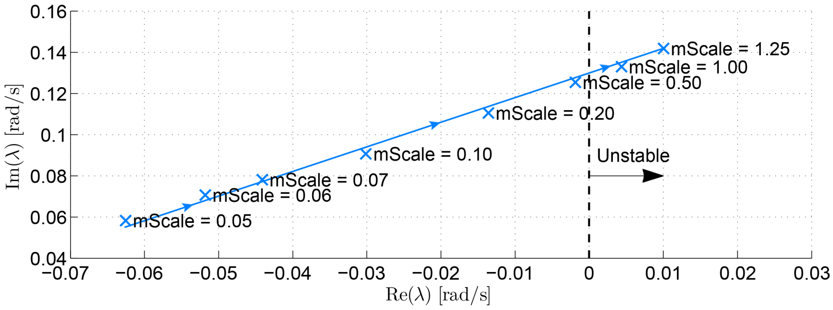

(b) Phugoid eigenvalues

Figure 5.11: Longitudinal eigenvalues for various mass scales at $V = 80\ m/s$

5.5.4. EFFECT OF INERTIA ON THE TAKE-OFF ROTATION

From previous results it was concluded that a decrease in mass and inertia results in a faster response to a disturbance or control input. The instantaneous pitch accelerations that arise from different control inputs are shown in Figure 5.12 for the various mass scales. The inertia has a very large effect on the pitch acceleration. A maximum pitch acceleration of about 7 degrees per squared second can be achieved with the heavy configuration, while the DUUC scaled by a mass factor of 10% can reach an acceleration up to 130 $^\circ/s^2$. The short period eigenvalues were found to be located on the stable side of the complex plane, however one can imagine that such high accelerations will cause the aircraft to quickly enter an unfavorable situation such as a deep stall.

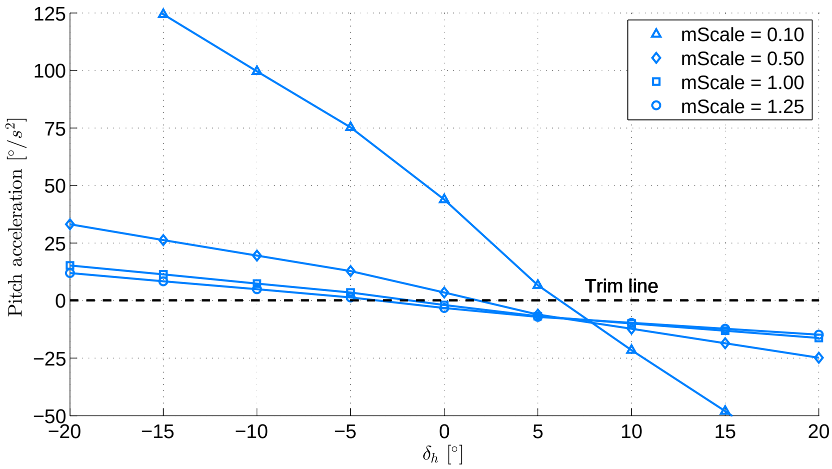

Figure 5.12: Effect of mass and inertia on the instantaneous pitch acceleration at $V = 80\ m/s$

5.6. EFFECT OF AIRCRAFT SCALING ON FLIGHT MECHANICS

In addition to the full-scale and subscale simulations, the scaling factor has been varied in order to examine a broader range of scale aircraft and the effect on the stability and control of the DUUC. However, the aerodynamics that have been obtained were for the 100% and 5.5% models only. Since the aerodynamics showed very similar behavior and according to the Froude scaling theory they should even be the same in terms of non-dimensional coefficients, a linear interpolation has been assumed between the two data sets.

The key parameters that are involved in the results of this section are mostly a function of velocity and/or time (frequency). Since these factors are therefore the most important scaling rules, they are stated again here:

$$V_s = V_f\sqrt{N} \tag{5.22}$$

$$t_s = t_f\sqrt{N} \tag{5.23}$$

5.6.1. EFFECT OF AIRCRAFT SCALING ON THE NEUTRAL POINT LOCATION

From the previous chapter it was found that the aerodynamics between the subscale and the full-scale DUUC showed minor discrepancies. This affects the neutral point of the aircraft, which should be taken into account when defining the CG position that corresponds to a desired static margin. The procedure explained in Section 5.2.2 has been performed for scaling factors between 2% and 100%. The resulting estimated neutral point location in terms of MAC percentage is displayed in Figure 5.13. A somewhat linear trend is observed, which is in correlation with the linear interpolation of the aerodynamic data. Furthermore it can be seen that the neutral point shifts aft as the aircraft scale increases, with a quantity between 52% and 58% MAC.

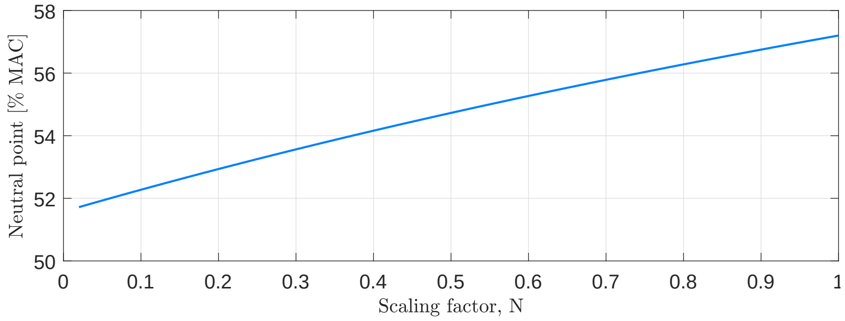

Figure 5.13: Effect of aircraft scaling on the neutral point location

5.6.2. EFFECT OF AIRCRAFT SCALING ON THE TRIM SOLUTION

A range of scaling factors between 2% and 100% has been investigated of which the trim angles are plotted in Figure 5.14. Note that the velocity V_f corresponds to the **full-scale** velocity and is scaled using Equation (5.22) depending on the scaling factor. The variation in angle of attack shows a linear trend with scaling factor, with the steepest slope at low velocities. The elevator trim angle of the scale models is slightly under-predicting the full-scale quantity, with a maximum error of about 2.5 degrees. Since this discrepancy is very marginal, it can be concluded that the trim solution of the full-scale DUUC can be estimated accurate enough using a scale model.

5.6.3. EFFECT OF AIRCRAFT SCALING ON THE LONGITUDINAL STATIC STABILITY

The effect of mass and inertia showed that the lighter the aircraft, the faster its response gets as was discussed in Section 5.5. This behavior is also found when dynamically scaling down the DUUC.

Again a range of scaling factors has been considered for which the same static stability analysis has been performed. The response has been scaled according to Equation (5.23) in order to see how closely the full-scale response can be estimated. From the curve corresponding to the full-scale case, it can be concluded that the trim aircraft returns to the initial trim angle after about 1.8 seconds followed by a small overshoot. Hereafter the AoA stabilizes around the 5 second mark. As N decreases, the first cross-over point shifts slightly to the right. However, it can be seen that the angle of attack stabilizes after 5-6 seconds for all scaling factors.

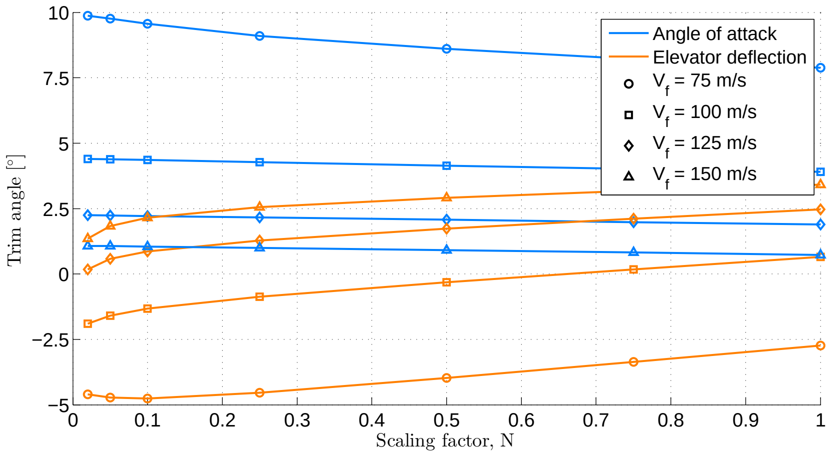

Figure 5.14: Effect of aircraft scaling on the trim solution

This indicates that the response to a certain disturbance in AoA can accurately be estimated using a dynamic scale model.

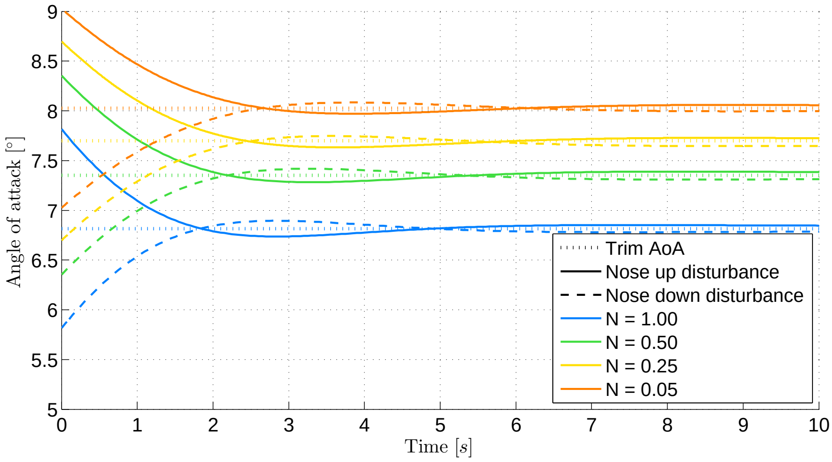

Figure 5.15: Effect of aircraft scaling on the static stability at $V_f = 80\ m/s$ and $SM = 0.10$

5.6.4. Effect of Aircraft Scaling on the Longitudinal Eigenvalues

The short period and phugoid characteristics are compared for different scales in Figure 5.16a and Figure 5.16b respectively for a **full-scale** airspeed of $V_f = 80\ m/s$ and the CG fixed at $SM = 0.10$. The short period eigenvalues are located on the negative (stable) side for the complete range of scaling factors. They are located on a straight line that goes through the origin. This makes sense because if the scaling factor goes to infinity, the aircraft's inertia will be infinite resulting in no response to a control input or disturbance. This observation can also be made when considering the phugoid eigenvalues.

The obtained eigenvalues of the scale models can be rescaled in order to predict the full-scale eigenmode characteristics. The short period eigenvalues are plotted versus scaling factor N in Figure 5.17, along with the corresponding dynamically scaled quantities (squares). The horizontal black dashed line indicates the frequency of the full-scale DUUC. It can be seen that estimates of the scale models are located below this line, meaning that the frequency is under-predicted. Furthermore it can be seen that as the scale reduces, the error becomes larger. This error is about 25% for the 2% scale model.

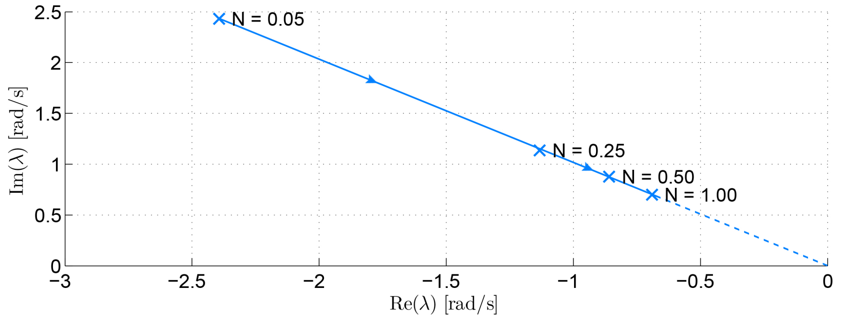

(a) Short period eigenvalues

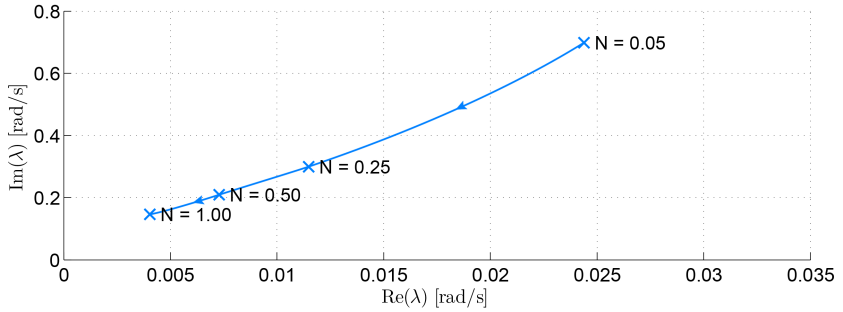

(b) Phugoid eigenvalues

Figure 5.16: Longitudinal eigenvalues for various scale factors at $V_f = 80\ m/s$

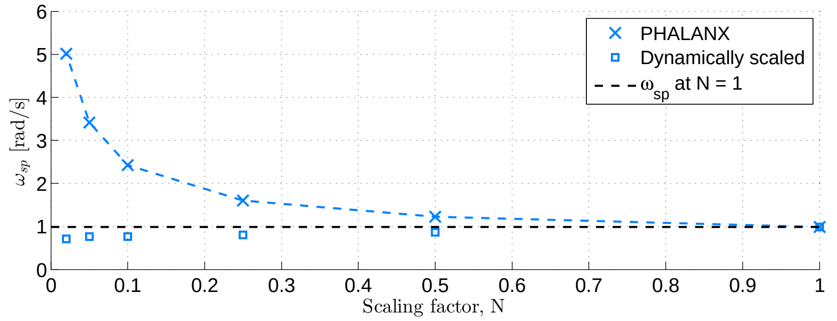

Figure 5.17: Short period frequency as function of scaling factor at $V_f = 80\ m/s$

The phugoid mode is found to be unstable for all scaling factors with an increasing frequency as N reduces. This frequency can be approximated using Equation (5.24), which is a function of flight speed.[28] Since each scale model is simulated at its scaled airspeed, Equation (5.24) can be rewritten to Equation (5.25) which is plotted in Figure 5.18 along with the results obtained with PHALANX. From this figure it can be concluded that the trend of the phugoid frequency is similar to the approximate function. The vertical offset depends on the airspeed at which the control input is initiated.

$$\omega_{ph} = \frac{g\sqrt{2}}{V} \tag{5.24}$$

$$\omega_{ph} = \frac{g\sqrt{2}}{V_f\sqrt{N}} = \frac{g\sqrt{2}}{80\sqrt{N}} \tag{5.25}$$

The squares in Figure 5.18 depict the dynamically rescaled phugoid frequencies for the various scale models, which are estimates of the full-scale ω_{ph}. It can be seen that this quantity can be estimated very closely.

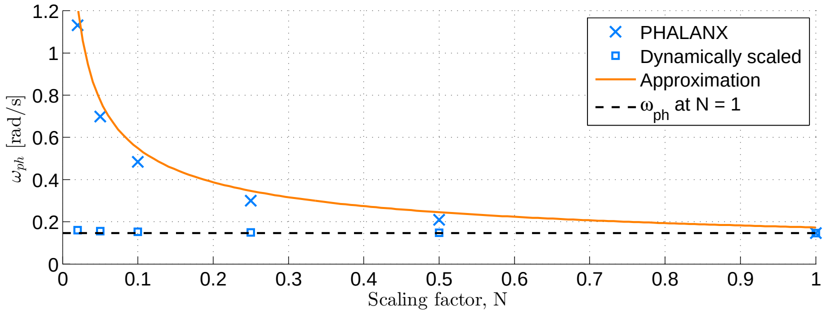

Figure 5.18: Phugoid frequency as function of scaling factor at $V_f = 80\ m/s$

5.6.5. EFFECT OF AIRCRAFT SCALING ON THE TAKE-OFF ROTATION

The effect of scaling factor on the pitch acceleration is similar to the effect of mass and inertia as was discussed earlier. In order to see how well the subscale DUUC can estimate the full-scale pitch acceleration, the following scaling factor is applied:

$$\dot{q}_f = \dot{q}_N N$$

The resulting pitch acceleration for the complete range of elevator deflection is shown in Figure 5.19. As the DUUC is scaled down, the discrepancy between dynamically rescaled data and the full-scale reference data becomes larger. The maximum variation in $\dot{q}$ is found to be about 3 deg/s^2. This means that the subscale results can be interpreted such that the suggested pitch acceleration of 6-8 deg/s^2 could be achieved at a larger elevator deflection than is actually required in reality (hence an under-prediction of $\dot{q}$).

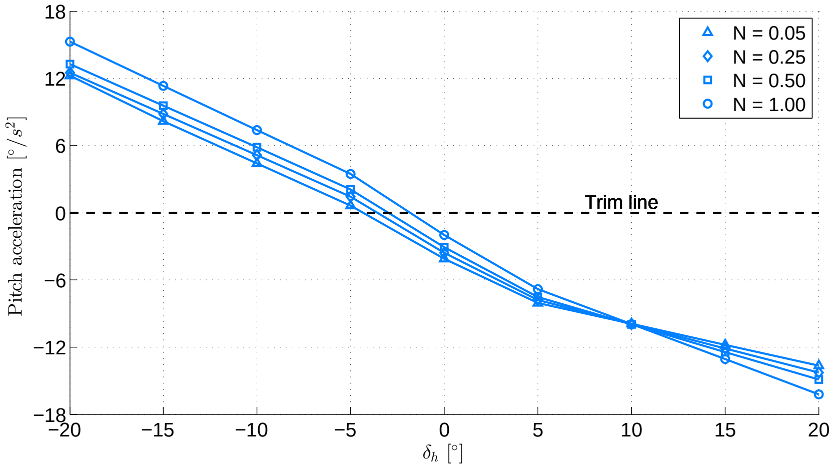

Figure 5.19: Effect of aircraft scaling on the instantaneous pitch acceleration at $V_f = 80\ m/s$

5.7. SKIN FRICTION DRAG CORRECTION SENSITIVITY

Since the FLUENT simulations are performed using an inviscid Euler solver, a drag correction had to be implemented to take into account the friction drag that is normally generated by the formation of the boundary layer. However, no actual data is available that can be used to assess the validity of the aerodynamic estimations. A drag factor (k_D) is implemented in PHALANX, which is a factor with which all the estimated friction drag coefficient are multiplied. This section discusses the sensitivity of this drag correction, which can still give insight in said validity.

The full-scale DUUC is trimmed at an airspeed equal to 80 m/s, from which a skin friction drag of 0.0213 is calculated in PHALANX. This value is compared to a reference case in order to see how accurate the approximation is. The skin friction drag of a reference B737-800 is obtained for a range of airspeeds between

Mach 0.2 - 0.9.[29] From this data, a coefficient of about 0.0218 is found for the DUUC's approach speed of Mach 0.226. By comparing the two results it can be concluded that the form factor approach gives an adequate approximation with an error of only 2%. Therefore, the C_{d_0} of the reference B737 corresponds to a k_D of 1.02. However, extreme and very unrealistic values for the drag factor (up to $k_D = 5$) are analysed in this study which confirms that the drag has a minor effect on the stability and control prediction.

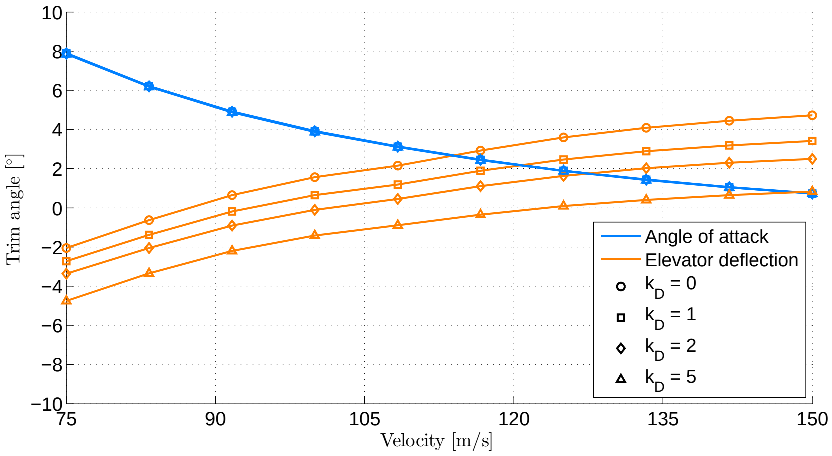

Figure 5.20: Sensitivity of the skin friction drag correction on the trim solution

The trim solutions for a range of k_D can be inspected in Figure 5.20. For the entire velocity range, the angle of attack at which the DUUC is trimmed does not change with a decrease or an increase in friction drag coefficient. As the trim velocity increases, the elevator has to be deflected more upward with higher drag values. The drag is mainly compensated for by increasing the thrust produced by the ducted fans. This causes a nose down pitching moment, which is in turn compensated by deflecting the horizontal vane further upwards. In Figure 5.21, this thrust coefficient is plotted from which it can indeed be concluded that the thrust increases as the drag factor becomes larger.

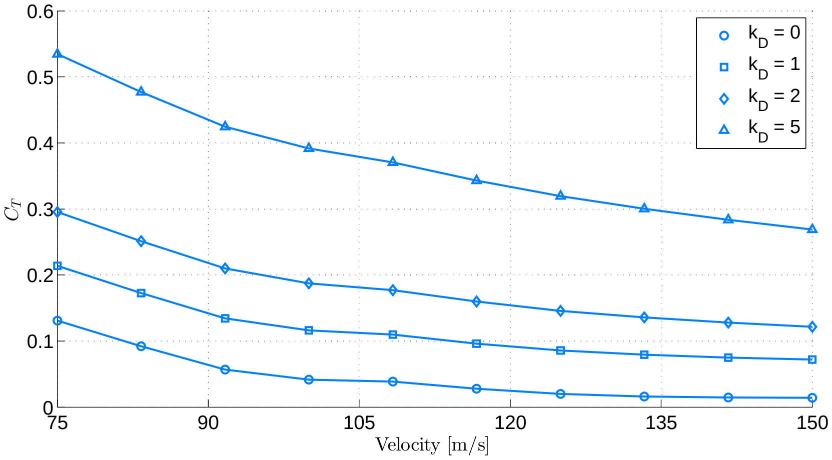

Figure 5.21: Sensitivity of the skin friction drag correction on the trim thrust coefficient

The short period and phugoid are simulated for this variety in k_D, of which the resulting eigenvalues are shown inFigure 5.22a and Figure 5.22b. In both figures the eigenvalue moves towards the left as k_D increases, indicated by the arrows. This doesn't affect the stability of the short period as this mode was already located in the stable region. The short period frequency increases if the drag increases, however this change is very minor. A frequency of 1.05 rad/s is found for $k_D = 5$, whereas the initial estimate of the full-scale DUUC was 0.98 rad/s. The phugoid mode changes from a slightly instable state to a stable one as the drag factor increases. The frequency of the motion is not affected significantly by the drag correction, however higher drag results in a slightly shorter period. A larger skin friction drag contribution causes the motion to damp out quicker, hence a higher damping ratio is obtained. An approximate solution for this quantity is presented in Equation (5.26), as function of the drag to lift ratio. For the derivation of this approximation, the reader is referred to Mulder et al.[28].

$$\zeta = \frac{1}{\sqrt{2}} \frac{C_D}{C_L} \tag{5.26}$$

An increase in drag will therefore contribute to an increase in drag to lift ratio, depending on the change in lift. As the thrust increases simultaneously with the drag factor to compensate for the addition in drag, the lift will also change to compensate for the increased moment due to thrust. Since the engines are located above the center of gravity, a higher thrust will enhance the nose down pitching moment and therefore the higher vane deflection (discussed earlier) will generate more downward lift. This means that the total lift decreases and therefore the drag to lift ratio increases even further.

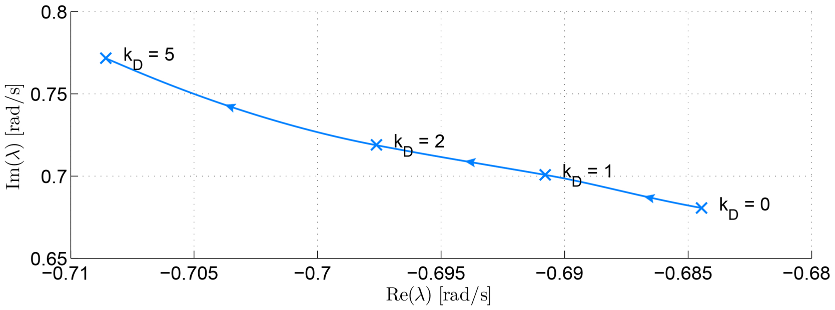

(a) Short period eigenvalues

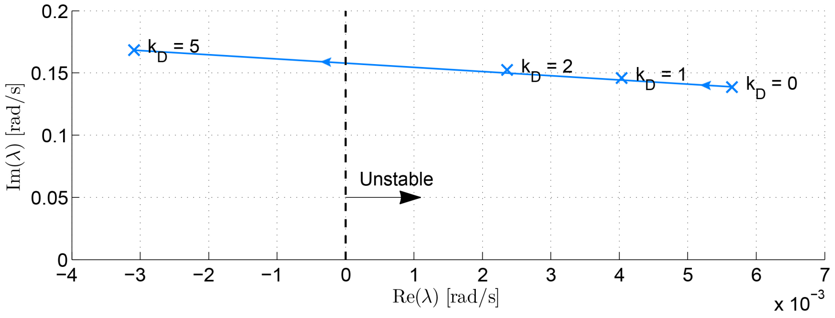

(b) Phugoid eigenvalues

Figure 5.22: Longitudinal eigenvalues for various skin friction drag correction factors at $V = 80\ m/s$ with $SM = 0.10$

5.8. Stability & Control Analysis of the DUUC

A more detailed analysis of the stability and control behavior of the DUUC is presented in this chapter, focussing on the full-scale case and the 5.5% scaled model.

5.8.1. Trim solution

In Figure 5.23a the trim solution for a variety of airspeeds is shown. The trends show an asymptotic behavior; as the velocity increases, the angle of attack and elevator deflection seem to level out at a certain angle. In the lower airspeed regime, it can be seen that in order to maintain trimmed at a flightpath angle of 0°, large elevator deflections are required. It is interesting to see that the minimum trim speed is not limited by the stall speed, but by these large vane deflections that will eventually be a mechanical constraint. Figure 5.23b shows the trimmed thrust coefficient (C_T) as function of velocity. This coefficient is a function of the thrust, flight speed, and the area of the actuator disk as shown in Equation (5.27). A similar asymptotic trend is seen with its value between 0.21 and 0.07. This corresponds to a thrust in the range of 9 to 13 kN per engine.

$$C_T = \frac{T}{0.5\rho V^2 A_{AD}} \tag{5.27}$$

The trim solution for the 5.5% scaled DUUC model is shown in Figure 5.24, for a velocity range of 20-35 m/s. This range corresponds to the full-scale range of 75-150 m/s using the Froude scaling relationship in Equation (5.22). Similar to the full-scale trim solution, the subscale shows an asymptotic trend as the velocity increases for both the angle of attack and elevator deflection. The required deflection to trim the scaled model is more negative for the complete velocity range in comparison to the full-scale. The angle of attack on the other hand is larger in magnitude. Figure 5.24b shows the thrust coefficient of the subscale DUUC, from which a similar trend is obtained as the full-scale. This parameter ranges between 0.35 and 0.12, corresponding to a trimmed thrust range of 2.4 - 3.7 N per engine. The magnitude of the trim thrust coefficient of the subscale simulation is almost twice as large as the full-scale C_T results. This also means that the thrust required to trim the full-scale aircraft will be estimated too large if the subscale data is considered. Such a difference between the two cases is a direct cause of the aerodynamics discrepancies. First of all the drag coefficients of the 5.5% DUUC were higher than the full-scale version. Secondly, the lift produces by the scaled model was found to be slightly lower, which means that the angle of attack should increase in order to make a horizontal steady flight possible. The increased lift on the wing produces a nose-up pitching moment, which is compensated for by increasing the throttle.

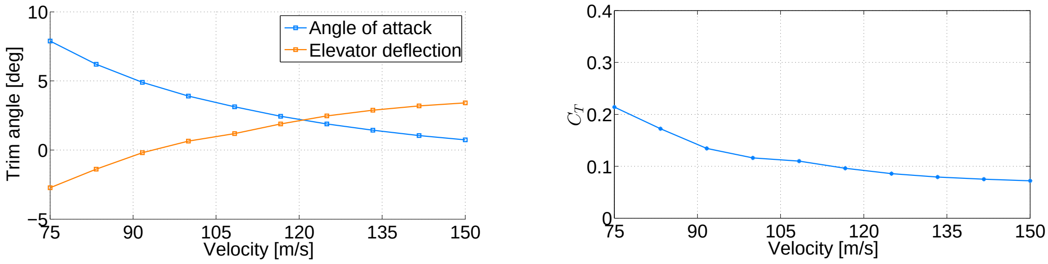

(a) Trim angles

(b) Thrust coefficient

Figure 5.23: Trim solution for the full-scale DUUC with $SM = 0.10$

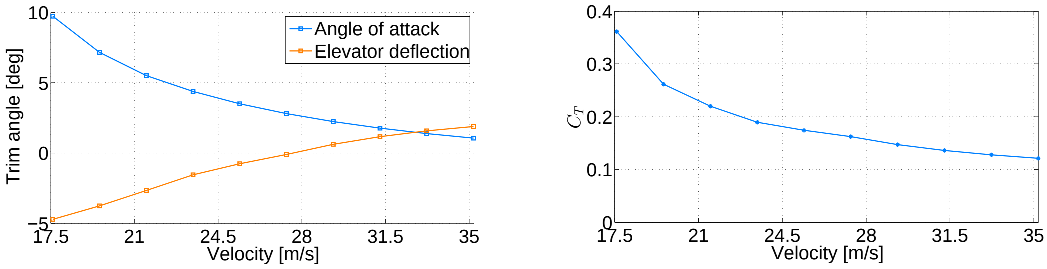

(a) Trim angles

(b) Thrust coefficient

Figure 5.24: Trim solution for the 5.5% scaled DUUC with $SM = 0.10$

5.8.2. LONGITUDINAL STABILITY

Longitudinal stability can be assessed in the following three categories: static stability, maneuver stability, and speed stability.

An aircraft is said to be statically stable if it returns to its initial state after a small disturbance, either nose up or nose down, is applied (i.e. $C_{m_\alpha} < 0$). This is simulated in PHALANX by applying a small $\Delta\alpha$ to the trimmed state, and simulating the response for a few seconds. Figure 5.25 shows the angle of attack for a nose up and nose down disturbance. If a nose up disturbance is applied, more lift will be generated with the center of pressure located behind the center of gravity. Therefore the aircraft will return to its original trimmed state over time. The same phenomenon can be seen in case of a nose down disturbance. Therefore the full-scale simulation results in a statically stable aircraft. The full-scale and subscale response to a 1 degree AoA disturbance is plotted in Figure 5.25. It can be seen that the subscale DUUC tends to return to the trimmed state much faster than the full-scale model.

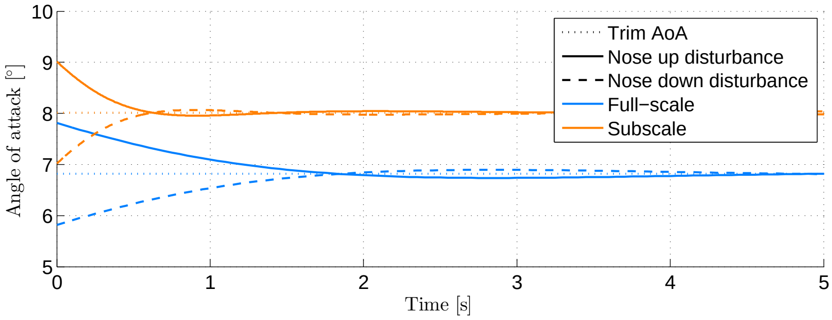

Figure 5.25: Comparison of the response to a 1 degree disturbance in AoA, between the full-scale and subscale DUUC at $V_f = 80\ m/s$ with $SM = 0.10$

Maneuver stability can be assessed in a similar way as static stability, however the disturbance is in this case related to a certain load factor that is introduced by a pitch rate (q). For a range of load factors, the required pitch rates can be determined according to Equation (5.28).[28]

$$q = \frac{g}{V}(n-1) \tag{5.28}$$

PHALANX will trim the model for the specified pitch rates, from which a elevator deflection (or stick force) is obtained. Maneuver stability is achieved when the $\Delta\delta_h$ is negative if Δn is positive, hence:

$$\frac{d\delta_h}{dn} < 0$$

The delta elevator deflection for load factors between -1 and 2.5 is plotted in Figure 5.26 for both cases. The slopes between the data points are negative for the largest part of the results and thus the aircraft possesses stability for such push-over and pull-up maneuvers. The analysis that is performed at a lower airspeed however, shows that for load factors below -0.5 and above 1.5 results in instability. The steepness of the curve is a measure for pitch control power. A large slope (low velocity) indicates that a lot of stick force is required to pull a maneuver, whereas a gradual slope (high velocity) requires less effort. This also means that at lower airspeeds, the stick limits will be reached at lower load factors in comparison to higher speed maneuvers. It can be seen that the subscale model can be used quite well for maneuvers below 1g for a variety of airspeed. For pull-up maneuvers above 1.5g, the scaled model tends to become unstable at low airspeeds and thus does not provide a correct estimate. As the velocity increases, the accuracy of the required $\Delta\delta_h$ increases.

The third longitudinal stability metric is called speed stability, which requires the aircraft to be controlled in a *logical sense* in case of an acceleration or deceleration. If the flight condition of an aircraft needs to be changed to another one at a lower flight speed, the aircraft should be rotated nose-up which increases the angle of attack and thus the elevator should be rotated trailing edge up to account for a moment balance. This stability can be assessed by looking at the elevator angle derivative with respect to the airspeed:[28]

$$\frac{d\delta_h}{dV} > 0$$

Hence, the pilot should pull the longitudinal stick to create a nose-up pitching moment. Figure 5.23a and Figure 5.24a already showed that the elevator deflection angle becomes less negative as the velocity increases, i.e. the full-scale and subscale DUUC possess speed stability.

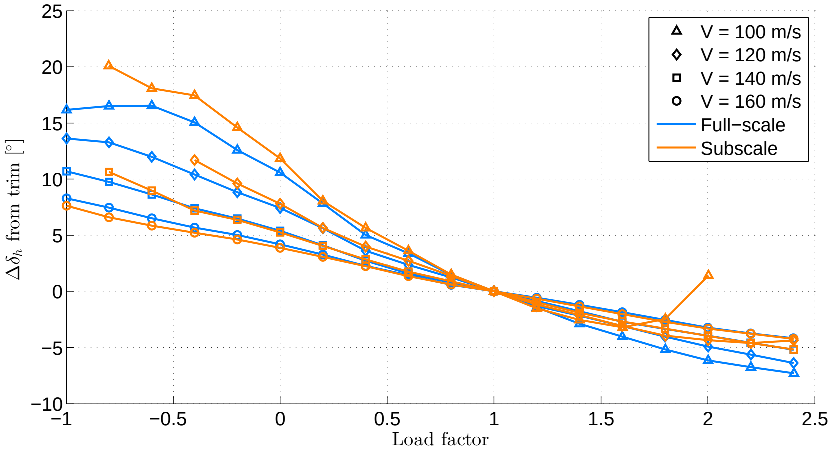

Figure 5.26: Required elevator deflection for different push-over and pull-up load factors at various flight speeds with $SM = 0.10$

5.8.3. LONGITUDINAL EIGENMODES

PHUGOID

The phugoid motions of the full-scale and subscale DUUC are plotted for a duration of 100 seconds in Figure 5.27. It can be seen that the oscillations are negatively damped and thus diverge over time. The full-scale motion has a period of about 43 seconds, whereas the subscale motion is much faster with a period of 9.5 seconds. By dynamically rescaling the subscale time response, a period of 40 seconds is found corresponding to the solid orange line in the figure. A damping ratio of -0.0276 and -0.0356 is found for the full-scale and subscale modes respectively. These quantities indicate a respective level 3 and level 4 phugoid of which the criteria are specified in MIL-F-8785C[30] as:

- Level 1: $\zeta_{ph} \geq 0.04$
- Level 2: $0 \leq \zeta_{ph} < 0.04$
- Level 3: $T_2 \geq 55\ s$
- Level 4: $T_2 < 55\ s$

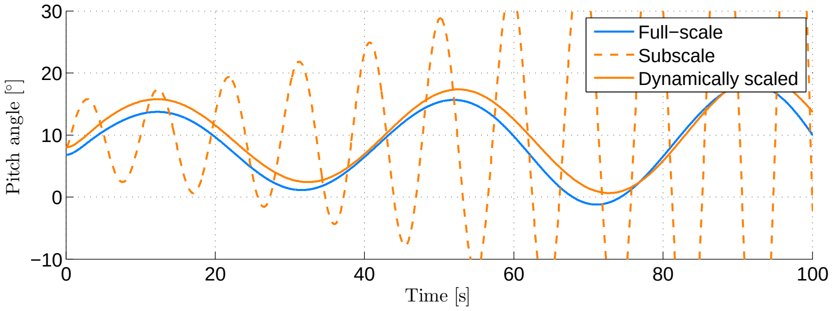

Figure 5.27: Comparison between the full-scale and subscale phugoid motion at $V_f = 80 m/s$ with $SM = 0.10$

SHORT PERIOD

The short period response to abrupt pitch control inputs has to meet certain requirements. Several levels are specified, for which the undamped natural frequency is limited for a range of the acceleration initiated by this abrupt input as shown in Figure 5.28. The response of the full-scale DUUC lies within the level 2 region, with a frequency of 0.98 rad/s and a damping ratio of 0.70. It can be seen that the subscale motion is significantly faster with a frequency of 3.25 rad/s, and therefore lies within the level 1 region. The rescaled motion has a frequency of 0.76 rad/s, which is positioned in the level 2 region again and thus forms a good estimate of the full-scale DUUC short period in terms of this criteria. The damping ratio of the subscale model is found to be 0.70 as well. This latter quantity is also well within the damping ratio limits corresponding to a level 1 short period response according to MIL-F-8785C[30]:

- Level 1: $0.35 \leq \zeta_{sp} \leq 1.30$
- Level 2: $0.25 \leq \zeta_{sp} < 0.35$ or $1.30 < \zeta_{sp} \leq 2.00$
- Level 3: $0.15 \leq \zeta_{sp} < 0.25$ or $\zeta_{sp} > 2.00$

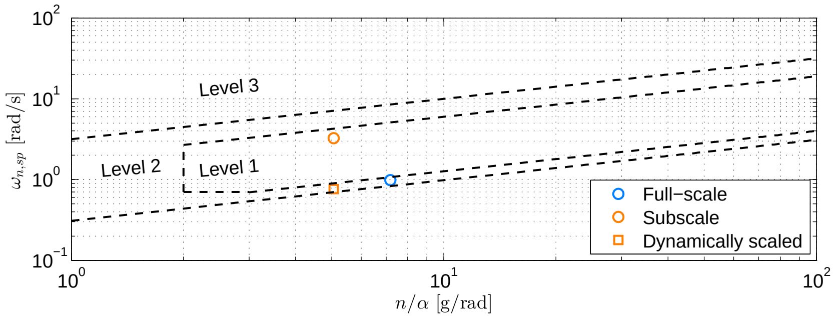

Figure 5.28: Short period response of the full-scale and subscale DUUC at $V_f = 80m/s$ with $SM = 0.10$

CONTROL ANTICIPATION PARAMETER (CAP)

The CAP is a parameter that describes the ratio of initial pitch acceleration over the steady state load factor. It is obtained using Equation (5.29), where T_{θ_2} is the time it takes to damp out the high frequency response to half its amplitude.[31], [32]

$$CAP = \frac{\Delta \dot{q}(0)}{\Delta n_{ss}} \approx \frac{g\omega^2_{n_{sp}} T_{\theta_2}}{V} \tag{5.29}$$

An aircraft is required to stay within certain limits of the CAP for an allowable range of short period damping ratios. A high CAP value is typically the cause of an undershoot in desired flight path, since the pilot will feel a large initial pitch acceleration. Such aircraft are described as fast, abrupt, and sensitive.[32] Figure 5.29 shows the CAP limits for different levels specified by MIL-STD-1797A[33]. A low CAP means that the pilot senses a low initial pitch acceleration. The lag between the initial pitch acceleration and the final steady-state normal acceleration causes the pilot to increase the input, which can lead to an overshoot in the desired flight path.

Figure 5.29 shows the CAP values of the full-scale and subscale DUUC. The scaled model is found to be in the level 1 region, whereas the full-scale DUUC is located just outside of this region. The orange square indicates the dynamically scaled quantity and results in an accurate prediction of the full-scale CAP.

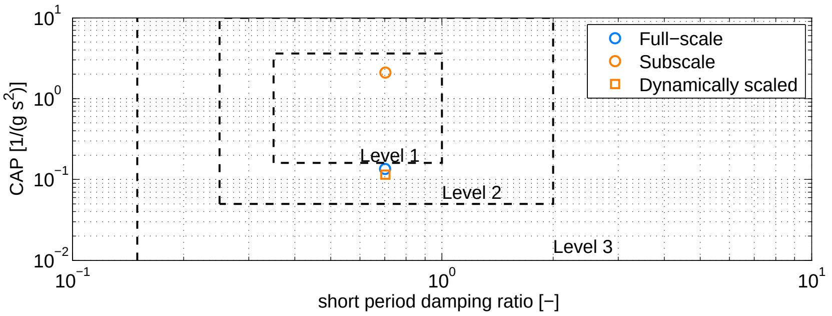

Figure 5.29: Control Anticipation Parameter of the full-scale and subscale DUUC at $V_f = 80\ m/s$ with $SM = 0.10$

5.8.4. MAXIMUM INSTANTANEOUS PITCH ACCELERATION

During take-off, an aircraft is recommended to have a certain pitch acceleration which results in a take-off rotation process of about 1-3 seconds. Roskam[34] states that this is achieved for large transport aircraft with a pitch acceleration of 6-8 $°/s^2$. In order to simulate a take-off rotation in PHALANX, a step input is applied on the elevator. The magnitude of this step input is derived from Figure 5.19, which showed that such a pitch acceleration is achieved by deflecting the vane approximately $-10°$ away from the trimmed state. The time history of the pitch acceleration ($\dot{q}$) is shown in Figure 5.30. A split second after the elevator is deflected (at $t = 1$), a pitch acceleration of 8.8 $°/s^2$ is achieved which gradually reduces back to zero after a few seconds. The subscale data, which is rescaled in this figure, shows an acceleration of about 8.2 $°/s^2$. The minor difference lies in the fact that the trim angles between the two scales slightly differ. However, PHALANX still provides a rather accurate prediction of the relation between elevator deflection and pitch acceleration that is required for a typical take-off rotation.

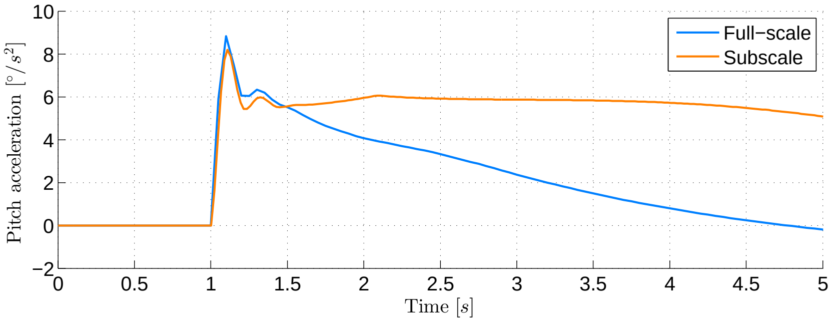

Figure 5.30: Take-off rotation of the full-scale and subscale DUUC at $V_f = 80\ m/s$ with $SM = 0.10$

5.8.5. PITCH CONTROL POWER

The elevator control power is defined as the change in moment coefficient induced by a certain vane deflection, shown in Equation (5.30). For conventional aircraft, this parameter is dependent on the Mach number since compressibility effects will result in a decrease in elevator effectiveness. In this study, compressibility effects are not taken into account as low subsonic speeds are considered only. However, the tail aerodynamics of the DUUC are unconventional due to the flow behavior entailed by the ducted fan engines. The thrust is not linearly related to the flight speed and thus it is interesting to look at the pitch control power for a range of trimmed conditions.

$$C_{m_{\delta_h}} = \frac{\partial C_m}{\partial \delta_h} \tag{5.30}$$

In order to find the pitch control power, a one degree step input has been applied to the trim conditions that were found for both aircraft for a **full-scale** velocity range between 75 m/s and 150 m/s. The initial moment coefficient is then subtracted from the one just after the elevator is deflected to find δC_m. Dividing this quantity by the one degree deflection results in the control power curves depicted in Figure 5.31. It can be seen that the subscale data does not form a good estimate for the full-scale DUUC. The subscale model shows an increase between -0.8 and -0.6 as the velocity increases, while the full-scale initially increases from -0.95 to -0.9, after which a slow decrease back to -0.95 can be observed. The discrepancy between the two is related to the aerodynamic differences that were found in Chapter 4.

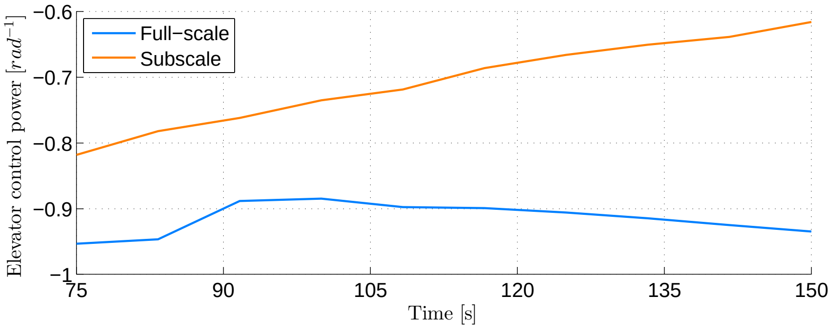

Figure 5.31: Elevator control power as function of airspeed with $SM = 0.10$

5.8.6. TIME-RESPONSE TO CONTROL INPUTS

A 2-3-1-1 control input is applied, which means that the elevator is rotated with an angle δ_h in alternating direction for two, three, one, and one second(s). This is usually done to evaluate the response to a long period control input, without entering any unfavorable attitude. A five degree deflection is selected as can be seen in the control input history in Figure 5.32.

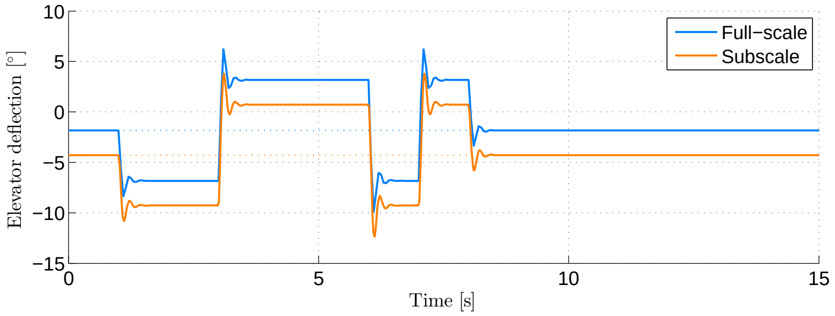

Figure 5.32: Elevator following a 2-3-1-1 control input with an amplitude of 5°

The full-scale and (dynamically rescaled) subscale time-responses to this 2-3-1-1 input are shown in Figure 5.33. Both the short period and phugoid modes can be distinguished from the figure. The velocity and pitch angle are dominated by the phugoid, whereas the angle of attack and pitch rate are dominated by the short period mode. Note that the pitch rate is plotted for only 15 seconds in Figure 5.33d. It can be seen that the subscale reaches a slightly higher pitch rate after the first two seconds of control input. This results in the discrepancy in angle of attack and pitch angle around the five second mark. Furthermore, the instability of the phugoid mode is again recognized. The magnitude of the flight speed gradually increases to about 10 m/s after two minutes of response. From these figures it can be concluded that the subscale DUUC can be used to predict the full-scale time-response to such 2-3-1-1 control inputs with significant confidence.

In addition to the elevator control input, the response to a 2-3-1-1 throttle input is analysed for both models. The selected input corresponds to a 1 kN deviation around the trimmed thrust per engine. Figure 5.34 presents the time-response of the vehicle. It can be seen that the effect of throttle is much less in comparison to the elevator deflection input. The velocity for example is only increased by about 0.5 m/s after two minutes. The trends however are the same as for the elevator control input response, in terms of the short period and phugoid modes. Furthermore, the subscale shows a slightly larger amplitude in the oscillations w.r.t. the full-scale model.

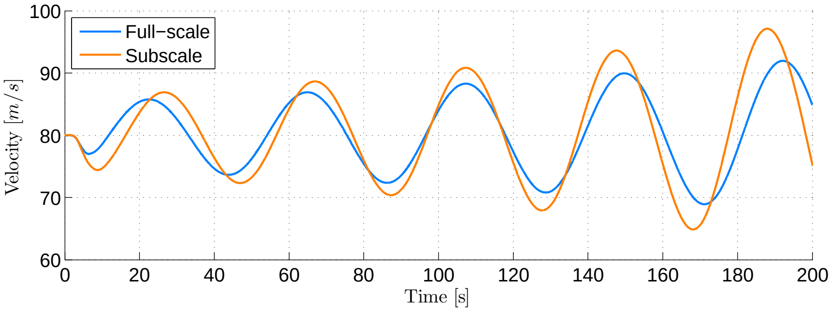

(a) Airspeed response

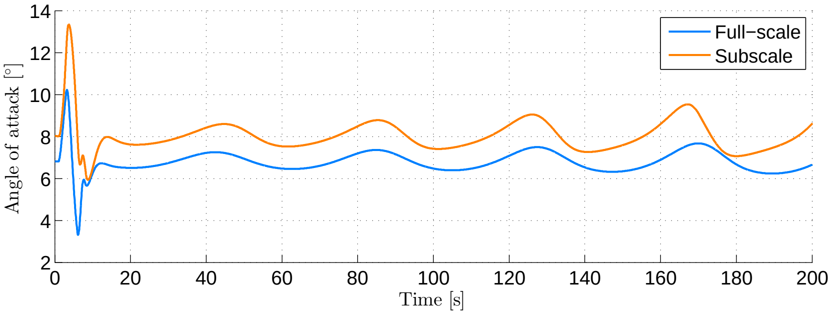

(b) Angle of attack response

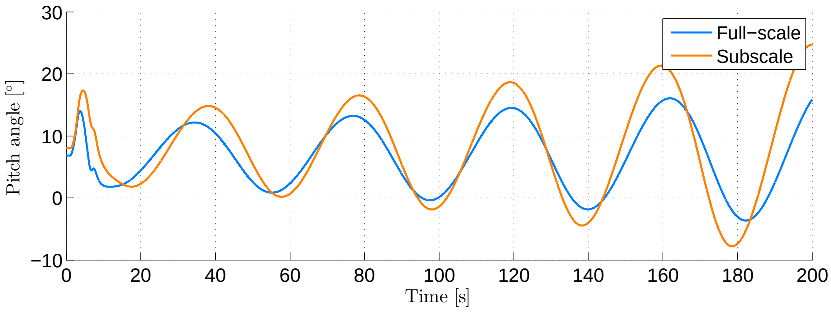

(c) Pitch angle response

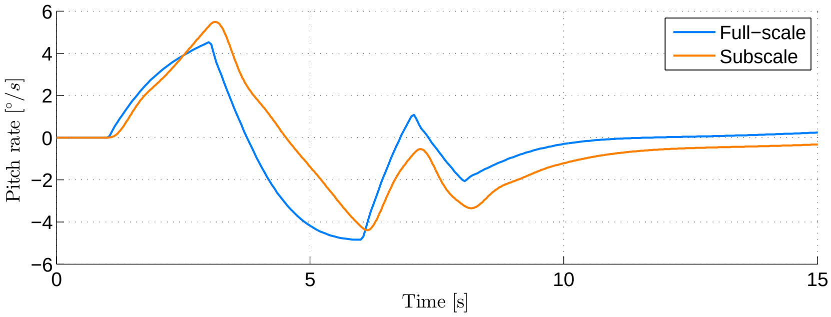

(d) Pitch rate response

Figure 5.33: DUUC response to a 5 degree 2-3-1-1 elevator input at $V_f = 80\ m/s$ with $SM = 0.10$

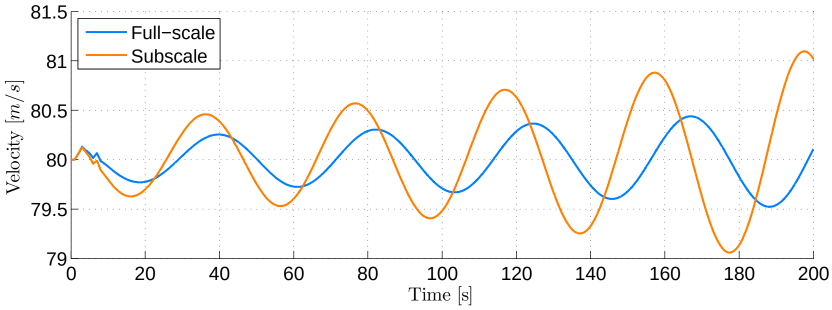

(a) Airspeed response

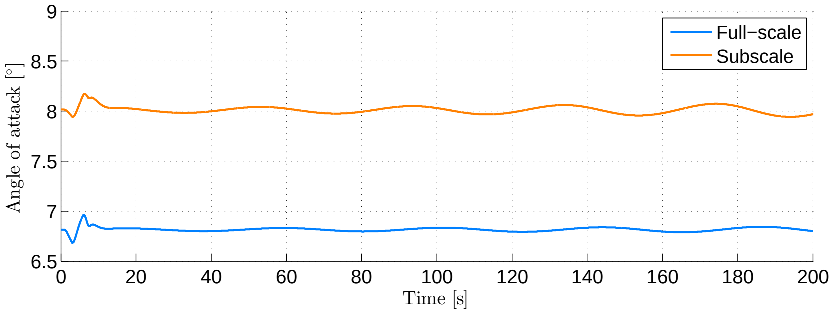

(b) Angle of attack response

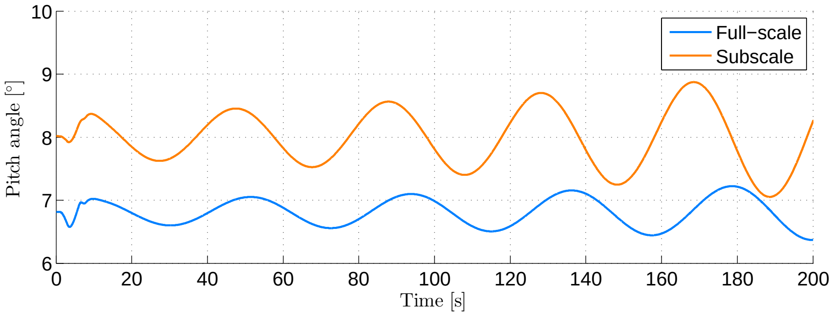

(c) Pitch angle response

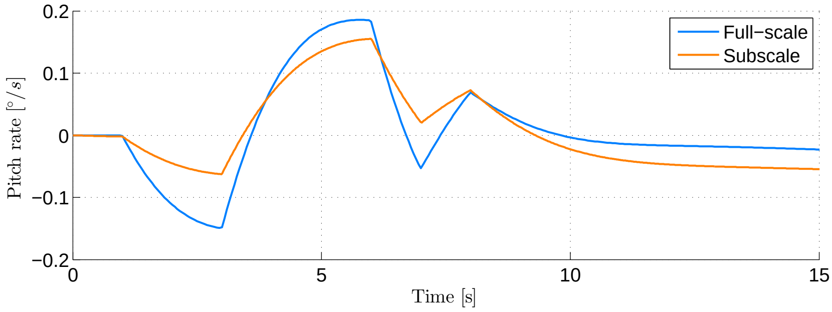

(d) Pitch rate response

Figure 5.34: DUUC response to a 2-3-1-1 single engine thrust of 1 kN input at $V_f = 80\ m/s$ with $SM = 0.10$

6

CONCLUSIONS AND RECOMMENDATIONS

Dynamically scaled flight testing is growing in attractiveness and shows to be promising in studies to novel aircraft concepts, as seen in the subscale BWB model named the X-48[6]. Since a scaled model of the DUUC is already developed and being tested, the stability and control analysis has been performed on both full-scale and subscale levels. Extrapolation rules can be extracted by comparing the two, which gives insight in the full-scale flight behavior and at the same time they will be helpful in further flight testing programmes of the DUUC. The subscale DUUC is based on a B737-700 model, with a geometric scaling factor of 5.5%. Since this aircraft features ducted fan engines, its mission is based on another turboprop aircraft with similar full-scale dimensions, namely the ATR-72. This lead to the low speed flight condition during the approach phase of the full-scale aircraft of 80 m/s, and the dynamically scaled equivalent of 19 m/s for the 5.5% scale model.

As a final chapter of this thesis, the key conclusions are summarized in Section 6.1. Further advice and recommendations are discussed in Section 6.2.

6.1. CONCLUSIONS

A parametric model of the DUUC has been created in the KBE software PARAPY, which allows for easy geometric changes. This program enables the user to export the geometry to for example IGES or STEP files, which can then be used in other applications. In this research, such a STEP file is created and imported in ANSYS FLUENT. An extensive CFD analysis is then performed, from which an aerodynamic data set is established that is used for flight mechanics simulation. The tool that is used for such simulations is the in-house toolbox PHALANX, which is Matlab / Simulink based and capable of assessing a diverse group of handling qualities.

Since this is only the start of research to dynamically scaled flight testing and the usage of the DUUC within this programme, the following research question is set for this thesis:

> Can the longitudinal stability and control behavior of the DUUC at low speed flight conditions accurately be predicted, by means of dynamically scaled flight testing?

DUUC aerodynamics

The total lift coefficient of the aircraft as function of angle of attack shows a typical linear trend, with a slope of 6.3 rad^{-1}. By deflecting the horizontal jet vane, no effect can be seen in the aerodynamics of the fuselage-wing combination. The components in and around the duct are significantly affected by such a deflection. An obvious result of deflecting the elevator downward is observed, namely a larger lift coefficient on the vane itself. The lift curve slope of the vane however is significantly smaller in comparison to for example the wing, since the flow in the duct tries to align with the duct walls. The duct produces more lift when the vane is deflected trailing edge up, due to the change in upper and lower pressure within the ring wing. A shift in lift curve is obtained, hence the gradient remains the same independent of the elevator deflection.

The drag curves for the lifting surfaces that are subjected to the free-stream flow show a typical parabolic trend with a minimum drag found at a slightly negative angle of attack. The elevator deflection has a significant effect on the drag coefficient of the duct, center body, vertical and horizontal vane. The drag coefficient of the horizontal vane and center body show a linear behavior as function of angle of attack with the slope depending on the elevator deflection. A trailing edge up deflection corresponds to a negative slope, hence an increase in angle of attack results in lower drag. Deflecting the vane trailing edge down shows an opposite trend.

Thrust has a significant effect on the DUUC's aerodynamics due to the positioning of the control vanes directly in the propeller slip stream. A higher thrust setting means that the components within the duct experience a higher velocity and thus more lift will be produced, which is either positive or negative depending on the vane deflection. This also holds for the drag of the horizontal jet vane. The vertical vane, duct, and center body however show a decrease in drag independent of the elevator deflection.

Handling qualities

The DUUC performs similarly to conventional aircraft when considering handling quality criteria. The center of gravity of the current model is located at approximately 18.1% MAC, based on the B737-700. However, the jet engines of this aircraft are located underneath and forward of the CG which causes a typical destabilizing effect. The DUUC features engines aft and above the CG line, and therefore contribute to a stabilizing effect. Linking this to the static margin defined in Equation (5.21), means that the actual neutral point of the DUUC is located more aft of the original one. The static margin is approximately 40%, which indicates an overly stable aircraft. In order to simulate a more realistic configuration, a static margin of 10% has been set. The elevator angle that is required to trim the aircraft at an approach speed of 80 m/s is -1.8°.

The short period mode is found to be stable while the phugoid is unstable, with frequencies of 0.98 and 0.15 respectively. The damping ratio of the short period is 0.70, whereas the phugoid is close to being critically damped with a ratio of 0.03. The longitudinal handling qualities can be assessed in terms of criteria specified in MIL-STD-1797A[33]. The short period and CAP criteria of the DUUC are found to be inside the **Level 2** region.

Static stability is investigated by applying a sudden nose up or nose down disturbance. With a 10% static margin, a 1 degree disturbance causes the DUUC to return to its trim angle in 2 seconds.

Finally the take-off rotation is studied by looking at the instantaneous pitch acceleration resulting from a maximum elevator deflection, initiated form a trimmed condition. According to Roskam[34], large transport aircraft should have a pitch acceleration of 6-8 $^\circ/s^2$. With a static margin of 10%, such an acceleration can be achieved by deflecting the horizontal vane from the trim angle to approximately 10 degrees.

Mass and inertia

The effect of mass and inertia has been studied for the full-scale DUUC with a static margin set at 10%. The weight of the DUUC has a direct influence on the lift that has to be produced as a counter force. This is achieved by flying at a different angle of attack, which in turn affects the thrust setting and elevator deflection angle. An increase in mass and inertia results in a larger AoA and a larger (more negative) δ_h.

By increasing the mass and thus inertia characteristics of the DUUC while keeping the geometry the same, the response of the vehicle becomes slower. This can be seen in both static and dynamic simulations. Moreover the longitudinal eigenmodes become less stable.

Due to the change in response speed, the maximum pitch acceleration that can be achieved is also affected significantly by mass and inertia. The maximum pitch acceleration corresponding to a $mScale$ of 1.25 is 7 $^\circ/s^2$, which can easily increase to over 100 $^\circ/s^2$ for a $mScale$ of 0.10.

Center of gravity

Shifting the CG location aft has a destabilizing effect, which is a typical result. The trim solution shows a significant decrease in elevator deflection magnitude and a minor decrease in AoA. As the flight speed increases, the elevator has to be set more trailing edge down in order to trim the DUUC. When the CG shifts behind the neutral point, an increase in velocity requires a more trailing edge up deflection of the elevator.

As the static margin decreases towards 0%, the initially stable short period becomes critically damped. An even further aft shift of the CG results in an unstable short periods, whereas the phugoid mode shows to become stable again.

The elevator was found to be positioned more trailing edge down if the static margin decreases, which means that a larger $\Delta\delta_h$ can be applied to initiate a nose up acceleration. The maximum achievable instantaneous pitch accelerations corresponding to static margins of 40%, 25%, 10%, and 2% are found to be -2, 7, 15, and 19 $^\circ/s^2$ respectively. The suggested value of 6-8 $^\circ/s^2$ can thus only be achieved within the elevator saturation limits if the CG is located aft of the $SM = 25\%$ position.

Scaling

The dynamically scaled model of the DUUC described above is also modelled and analysed in terms of aerodynamic performance and stability and control behavior. It was found that the trim solutions of the subscale and full-scale model show very high similarity. The response of the subscale model is much faster as expected. The frequency of the phugoid is found to be inversely proportional to the root of the scaling factor. This is in compliance with the approximate function that relates the frequency to the airspeed.

The change in response speed is also noticed in the take-off pitch acceleration, in a similar fashion as was seen for a variation in mass scale. A small aircraft achieves much higher rotational rates, but are therefore also more susceptible to disturbances.

Extrapolation rules

Besides the effect of scaling itself, an interesting aspect to investigate is how well subscale simulation can be used to determine full-scale flight behavior. Besides geometric and inertial scaling, it is important to scale flow characteristics in order to maintain similitude. The key parameters that are to be scaled are time and velocity. According to the Froude scaling theory, dimensionless parameters such as angles do not require any scaling factor. Trimming of the aircraft however, showed minor discrepancies in trim angle. The error becomes larger as the size of the aircraft reduces, but stays within 2.5 degrees for a 2% scaled model.

The short period and phugoid characteristics of the scale models can be rescaled to form estimates of the full-scale characteristics. Again this estimate deteriorates as the scale of the DUUC gets smaller. The short period frequency is under-predicted by about 10% for a scale model of 50%, which goes up to about 25% for scale models in the order of a few percentage . The phugoid frequency is estimated quite well within 5% for scaling factors above 0.10. This discrepancy raises towards an 10% over-prediction for the 2% scale model.

Rescaling of the scaled simulated pitch accelerations for take-off resulted in a fairly good estimate of the actual full-scale quantity. The error increases once again with decreasing scaling factor due to the discrepancy in aerodynamic coefficients. A 5.5% scale model of the DUUC underestimates the instantaneous pitch acceleration by about 3 $^\circ/s^2$. This error reduces if smaller elevator inputs are applied.

Above listed conclusions aid in formulating a general conclusion that answers the main research question stated in the beginning of this section. The DUUC shows to behave similar to conventional aircraft, with the exception of a stabilizing effect of the engine due to its placement. A typical B737-700 has its CG located at approximately 20% MAC, whereas the DUUC's CG has to be located at 48% MAC for a typical static margin of 0.10. All in all, the propulsive empennage proves to be capable of taking over the job of a conventional tail configuration. The jet vanes are small but powerful enough to maneuver the aircraft without extreme deflection angles. This is demonstrated with both a free-flying scale model, as well as simulation on subscale and full-scale levels. Furthermore the scaled simulations show that the full-scale flight behavior can be estimated with adequate accuracy, however the error increases as the scale model gets smaller.

6.2. RECOMMENDATIONS

Since this thesis only presents work that could be performed within a certain time window, some recommendations can be made for future research. These are summarized in this section, regarding the following categories: PARAPY model, aerodynamic analysis, stability and control analysis, and dynamically scaled flight testing of the DUUC.

PARAPY MODEL

- **Implement high lift devices** The parametric model that represents the DUUC consists of a B737-700 wing shape in clean configuration. More detail could be implemented in this model by generating parametric high lift devices. These can then be set at the desired settings for further aerodynamic or structural analysis.
- **Volume mesh generation** The integrated SALOME mesher in PARAPY can be used to generate volume meshes of the DUUC model. This will form a link between geometric modeling and CFD analysis that can increase the level of automation.

AERODYNAMIC ANALYSIS AND STABILITY AND CONTROL

- **Improve on the actuator disk model** The actual effect of the propeller aerodynamics on the propulsive empennage is simplified by using an actuator disk model. ANSYS FLUENT is capable of modeling propeller flows, by means of a sliding mesh method. A time-dependent simulation will be required, which significantly increases the number of elements in the mesh as well as computation times.
- **Perform RANS analysis** In current study, the effect of boundary layer formation is ignored by the Euler solver. A more accurate prediction can be done by including this boundary layer using a turbulence model. The full aircraft model should most likely be replaced by an isolated duct model to maintain a fairly useful mesh size.
- **Lateral and directional analysis** In the aerodynamic analysis presented in this thesis, only the angle of attack and horizontal vane deflection is varied. The effect of sideslip and vertical vane deflection is to be included in order to study lateral and directional motions or one engine inoperative conditions.
- **Investigate the aerodynamics of high lift devices** A clean wing approach phase is assumed in this study, however the effect of scaling on the performance of high lift devices is interesting to analyse as it represents a more realistic case.
- **Study different flight conditions** The simulations described in this thesis are mainly performed at low speed flight conditions at sea-level. It is suggested to investigate the effect of altitude and compressibility effects at high speed.
- **Moving mass during flight** PHALANX has the capability of accounting for a shift in mass (e.g. fuel) during a simulation. The effect of such a shift can be studied in future research, which may lead to more efficient trim solutions as it will allow for active control of the static margin during flight.

DYNAMICALLY SCALED FLIGHT TESTING OF THE DUUC

- **Validation** The obtained results with PHALANX should be compared to actual flight test data in order to see how well the flight mechanics are simulated.
- **Duct design optimization** It is much easier to adapt a small scale model in comparison to the full-scale version. Various design parameters of the ducted fan can be studied in this way, from which the design can be optimized depending on its mission.
- **Control vane design** More complex control surface shapes can be installed to study its effect on the flight behavior of the DUUC.

BIBLIOGRAPHY

[1] Chambers J. R. *Modeling Flight: The Role of Dynamically Scaled Free-Flight Models in Support of NASA's Aerospace Programs*. US National Aeronautics and Space Admininistration, 2009.

[2] Jordan T. L. and Bailey R. M. *NASA Langley's AirSTAR Testbed – A Subscale Flight Test Capability for Flight Dynamics and Control System Experiments*. AIAA Guidance, Navigation and Control Conference and Exhibit, AIAA Paper 2008-6660, August 2008.

[3] Conner M. *NASA Armstrong Fact Sheet: Prototype-Technology Evaluation and Research Aircraft (PTERA)*. Retrieved August 17, 2016, from `https://www.nasa.gov/centers/armstrong/news/FactSheets/FS-108-AFRC.html`, October 2015.

[4] Eveleens L. C. and Bremmers F. *Free Flying Scale Model Flight Testing: Future or Fiction?* NLR-TP-2016-191, May 2016.

[5] Schmollgruber P., Jentink H. W., and Tuinstra M. *IEP: A Multidisciplinary Flying Testbed for New Aircraft Concepts*. Proceedings of the 27th International Congress of the Aeronautical Sciences (ICAS), September 2010.

[6] Gibbs Y. *X-48B Blended Wing Body*. Retrieved August 17, 2016, from `http://www.nasa.gov/centers/dryden/research/X-48B/index.html`, February 2016.

[7] Yarf-Abbasi A. and Fielding J. P. *Design Integration of the Eclipse and Demon Demonstrator UAV's*. AIAA 2007-7725. 7th AIAA Aviation Technology, Integration and Operations Conference (ATIO), Belfast, UK, September 2007.

[8] Lundström D. and Amadori K. *RAVEN - A Subscale Radio Controlled Business Jet Demonstrator*. Proceedings of the 26th International Congress of the Aeronautical Sciences (ICAS), 2008.

[9] Jouannet C. et al. *Personal Jet - A Student Project*. 4th CEAS Air & Space Conference, 2013.

[10] Conner M. *X-56A Multi-Utility Technology Testbed*. Retrieved August 17, 2016, from `http://www.nasa.gov/centers/armstrong/research/X-56/index.html`, July 2015.

[11] Richards J. et al. *Design for Flight Test of a Scaled Joined Wing SensorCraft*. 52nd AIAA/ASME/ASCE/AHS/ASC Structures, Structural Dynamics and Materials Conference, Denver, Colorado, USA, April 2011.

[12] La Rocca G., Krakers L., and van Tooren M. J. L. *Development of an ICAD Generative Model for Blended Wing-Body Aircraft Design*. 9th AIAA/ISSMO Symposium on Multidisciplinary Analysis and Optimization. Atlanta, Georgia, September 2002.

[13] La Rocca G. and van Tooren M. J. L. *Development of design and engineering engines to support multidisciplinary design and analysis of aircraft*. Eindhoven University of Technology, 2005.

[14] Koning J. H. *Development of a KBE application to support aerodynamic design and analysis*. MSc thesis. Delft University of Technology, 2010.

[15] Wei J. H. *Parametric Modelling for Determining Aircraft Stability & Control Derivatives*. MSc thesis. Delft University of Technology, 2016.

[16] Burnette T. *Python*, volume 39 of *Computerworld*. May 2005.

[17] van Dijk R. E. C. and Baan Y. M. *ParaPy Tutorial - Introduction to ParaPy: Classes, Methods, and Object-Oriented Programming*. ParaPy B.V., 2016.

[18] ParaPy B.V. *Platform Features*. Retrieved September 9, 2016, from `https://www.parapy.nl`, 2016.

[19] Filippone A. *Advanced Aircraft Flight Performance*, volume 34 of *Cambridge Aerospace Series*. Cambridge University Press, December 2012.

[20] ANSYS Inc. *Fluent 6.3 User's Guide*. September 2006.

[21] Stipa L. *Experiments with Intubed Propellers*. National Advisory Committee for Aeronautics, Washington, DC, USA, January 1932.

[22] Fletcher H. S. *Experimental Investigation of Lift, Drag, and Pitching Moment of Five Annular Airfoils*. National Advisory Committee for Aeronautics, Langley Field, VA, USA, October 1957.

[23] Nicoud F. *Unsteady Flow Modeling and Computation*. Available at `http://www.math.univ-montp2.fr/~nicoud/PDF/notes_Nicoud_1and2.pdf`, November 2007.

[24] Prabhu R. K. *An Inviscid Computational Study of Three '07 Mars Lander Aeroshell Configurations Over a Mach Number Range of 2.3 to 4.5*. National Aeronautics and Space Administration, Washington, DC, USA, 2002.

[25] Raymer D. P. *Aircraft Design: A Conceptual Approach*. AIAA education series, Washington, USA, August 1992.

[26] LTH. *Luftfahrttechnisches Handbuch*. Available at `https://www.lth-online.de/`, 2015.

[27] Chris Brady. *The 737 Information Site*. Available at `http://www.b737.org.uk/techspecsdetailed.htm`, 1999.

[28] Mulder J. A. et al. *AE3202 Flight Dynamics - Lecture Notes*. Faculty of Aerospace Engineering, Delft University of Technology, March 2013.

[29] Raymer D. P. et al. *Advanced technology subsonic transport study: N+3 technologies and design concepts*. National Aeronautics and Space Administration, Glenn Research Center, 2011.

[30] Anon. *Military Specification - Flying Qualities of Piloted Airplanes. MIL-F-8785C*. Department of Defense, USA, November 1980.

[31] Stengel R. F. *Flight Dynamics*. Princeton University Press, 2004.

[32] Kivioja D. A. *Comparison of the Control Anticipation Parameter and the Bandwidth Criterion During the Landing Task*. Applied Computational Fluid Dynamics. Master Thesis, Air Force Institute of Technology, March 1996.

[33] Anon. *Military Standard - Flying Qualities of Piloted Aircraft. MIL-STD-1797A*. Department of Defense, USA, January 1990.

[34] Roskam J. *Airplane Design Part VII: Determination of Stability, Control and Performance Characteristics*. DARcorporation, 1985.

[35] Wolowicz C. H., Bowman J. S., and Gilbert W.P. *Similitude Requirements and Scaling Relationships as Applied to Model Testing*. NASA technical paper. National Aeronautics and Space Administration, Scientific and Technical Information Branch, August 1979.

[36] ANSYS Inc. *ANSYS CFX Reference Guide*. Release 15.0, November 2013.

[37] Lombard J. *Introduction to Structured Grid Generation for Aeronautics*. Swiss Institute of Technology Lausanne, September 2011.

[38] Bakker A. *Lecture 11 - Boundary Layers and Separation*. Applied Computational Fluid Dynamics. Retrieved December 20, 2016, from `http://www.bakker.org/dartmouth06/engs150/11-bl.pdf`, October 2015.

[39] Hoerner S. F. *Fluid-Dynamic Drag*. Hoerner Fluid Dynamics, 1965.

A

IMAGES OF RELEVANT PROJECTS

NACRE

Photo taken by Marcin Szender for the article at:
http://www.samolotypolskie.pl/samoloty/14770/126/NACRE-IEP2

X-48

Photo taken by Tony Landis. Used for the article *X-48B on Rogers Dry Lakebed* at:
http://www.nasa.gov/centers/dryden/multimedia/imagegallery/X-48B/ED06-0198-50.html

Boeing Phantom Works
NASA
X-48B

PTERA

Photo used for the article *Modular, Adjustable: A Test Plane for Any Occasion* at:
`http://www.technology.org/2016/06/10/modular-adjustable-a-test-plane-for-any-occasion/`

AREA-I
AREA-I
NASA

AIRSTAR

Photo taken by Denise Lineberry for an article at:
`http://www.nasa.gov/centers/langley/news/researchernews/snapshot_ghowland.html`

DEMON

Photo used on for a database of UAV data at:
`http://www.uavglobal.com/bae-systems-demon/`

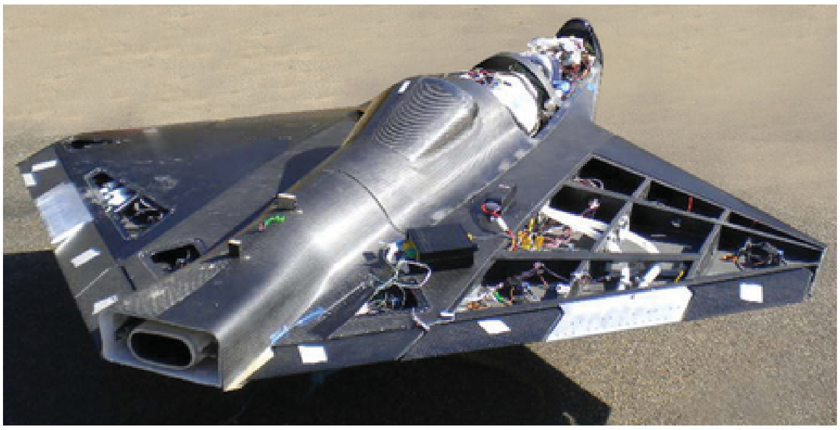

SMARD

Front page image of the technical report:
Eveleens L.C. and Bremmers F. *Free Flying Scale Model Flight Testing: Future or Fiction?* NLR-TP-2016-191, May 2016.

NLR
PH-SMARD

RAVEN

Photo used on the Linköping University website:
`https://www.iei.liu.se/flumes/aircraft-design/raven/raven_homepage?l=en`

MIDJET

Photo taken by David Lundström. Used on a RC aircraft hobbyist forum:
`http://www.rcuniverse.com/forum/rc-jets-120/11602839-behold-midjet.html`

MUTT

Photo taken by Jim Ross. Used for the article *X-56A Completes Envelope Clearance Flights* at:
`www.nasa.gov/centers/armstrong/features/X-56A_milestone.html`

JWSC

Image used in the article:
Richards J. et al. *Multidisciplinary Design for Flight Test of a Scaled Joined Wing SensorCraft.* AIAA 2010-9351. 13th AIAA/ISSMO Multidisciplinary Analysis Optimization Conference, September 2010.

B

DERIVATION OF SCALING FACTORS

The geometric scaling law is derived in Appendix B.1. Appendix B.2 presents the scaling laws that ensures inertia similitude. The three different scaling methods that can be used in aircraft scaling are Froude, Mach, and Reynolds scaling for which the scaling laws are derived in Appendix B.3, Appendix B.4, and Appendix B.5 respectively. The subscale and full-scale model will be denoted by the subscript letters s and f respectively.

B.1. GEOMETRIC SCALING LAWS

Geometry is linearly scaled and the scaling factor relating the characteristic length of model and prototype is denoted as N as shown in Equation (B.1).

$$\frac{l_s}{l_f} = N \tag{B.1}$$

Thus if a model has an overall length of 5 times smaller than the prototype aircraft, N is equal to $^1/_5$. Subsequently, an area is scaled by N^2 and a volume by N^3.

B.2. INERTIA SCALING LAWS

B.2.1. FLUID DENSITY

Fluid density is a parameter that plays a huge role in aerodynamics, and returns in important parameters such as the Reynolds number and lift coefficient. The density ratio between both systems will simply be denoted as σ.

$$\frac{\rho_s}{\rho_f} = \sigma \tag{B.2}$$

B.2.2. MASS

The fluid density ratio above can be used to define the mass scaling factor. The dimension of mass (M) can be rewritten, by introducing the length dimension (L) as is done here:

$$[m] = M = \frac{M}{L^3} L^3 \tag{B.3}$$

In Equation (B.3), the unit of fluid density is recognized in the first term of the right hand side. The second term is simply a geometric volume scaling, therefore Equation (B.4) results as mass scaling law.

$$m_s = m_f \sigma N^3 \tag{B.4}$$

B.2.3. MASS MOMENT OF INERTIA

Analysis of the units can also be applied for the mass moment of inertia, which has unit ML^2. This is equivalent to the mass scaling factor multiplied by another N^2, which is shown in Equation (B.5).

$$I_s = I_f \sigma N^5 \tag{B.5}$$

B.3. FROUDE SCALING

Froude scaling ensures that the flow velocity over the model and full-scale aircraft are similar compared to their respective characteristic lengths, hence equal Froude number:

$$\begin{gathered} Fr_s = Fr_f \\ \left(\frac{V}{\sqrt{gl}}\right)_s = \left(\frac{V}{\sqrt{gl}}\right)_f \end{gathered} \tag{B.6}$$

From this similitude criteria, scaling factors can be found for the following parameters: velocity, Froude number, Mach number, Reynolds number, dynamic pressure, time, and lift and moment coefficients.

B.3.1. VELOCITY

It is obviously impossible to change the gravitational field around either the model or the prototype, however for the sake of completeness the ratio of g is kept in the equation. Therefore Equation (B.6) can be rewritten to obtain the scaling relation as shown in Equation (B.7).

$$V_s = V_f \sqrt{\frac{g_s}{g_f}\frac{l_s}{l_f}} = V_f \sqrt{\frac{g_s}{g_f}}\sqrt{N} \tag{B.7}$$

B.3.2. MACH NUMBER

Equation (B.7) can be transformed to a relationship between both Mach numbers as such:

$$M_s = \frac{V_s}{a_s} = \frac{V_f\sqrt{\frac{g_s}{g_f}N}}{a_s} = M_f \frac{a_f\sqrt{\frac{g_s}{g_f}N}}{a_s} \tag{B.8}$$

The ratio between velocity of sound for model and prototype can be written as

$$\frac{a_s}{a_f} = R_{V_s}$$

resulting in a Mach number scaling relation as shown in Equation (B.9).

$$M_s = M_f \frac{\sqrt{\frac{g_s}{g_f}N}}{R_{V_s}} \tag{B.9}$$

B.3.3. DYNAMIC PRESSURE

Dynamic pressure is defined as the kinetic energy per unit volume of a fluid:

$$q = \frac{1}{2}\rho V^2$$

Therefore the ratio of dynamic pressures becomes

$$\frac{q_s}{q_f} = \frac{{}^1\!/_2 \rho_s V_s^2}{{}^1\!/_2 \rho_f V_f^2} \tag{B.10}$$

Substitution of Equation (B.2) and Equation (B.7) in Equation (B.10) results in the following scaling relationship between dynamic pressures.

$$q_s = q_f \sigma \frac{g_s}{g_f} N \tag{B.11}$$

B.3.4. REYNOLDS NUMBER

By reintroducing the kinematic viscosity term $\nu = \frac{\mu}{\rho}$ in the Reynolds number equation, the ratio of Reynolds number between model and aircraft can be found for Froude scaling as shown in Equation (B.12).

$$\frac{Re_s}{Re_f} = \frac{\frac{V_s l_s}{\nu_s}}{\frac{V_f l_f}{\nu_f}} = \frac{V_s l_s}{\nu_s} \frac{\nu_f}{V_f l_f} \tag{B.12}$$

Equation (B.12) can be rewritten in terms of the geometric scaling factor N as shown in Equation (B.13)

$$Re_s = Re_f \left(\frac{\nu_f}{\nu_s}\right) N^{3/2} \sqrt{\frac{g_s}{g_f}} \tag{B.13}$$

B.3.5. TIME

The time it takes for an aircraft to fly a certain distance can be obtained when dividing this distance by the flight velocity. This is shown in term of dimensions in Equation (B.14).

$$[t] = T = \frac{L}{LT^{-1}} \tag{B.14}$$

Since the velocity and length scaling ratios have readily been established, the time scaling factor can be derived as shown in Equation (B.15).

$$t_s = t_f \frac{N}{\sqrt{\frac{g_s}{g_f} N}} = t_f \sqrt{\frac{g_f}{g_s}} \sqrt{N} \tag{B.15}$$

B.3.6. LIFT, DRAG, AND MOMENT COEFFICIENTS

An interesting aerodynamic parameter to consider is the lift force and its corresponding coefficient. A Froude scaled model however, shows that the ratio of lift coefficients between model and aircraft is equal to 1 which is proven in Equation (B.16) and Equation (B.17).

$$C_{L_s} = C_{L_f} \left(\frac{m_s g_s}{m_f g_f}\right) \left(\frac{q_f S_f}{q_s S_s}\right) \tag{B.16}$$

Substitution of the mass, dynamic pressure, and surface area scaling factors into Equation (B.16), results in the cancellation of all parameters as shown in Equation (B.17). The drag coefficient is similar as shown in Equation (B.18).

$$C_{L_s} = C_{L_f} \left(N^3 \sigma \frac{g_s}{g_f}\right) \left(\frac{1}{\sigma \frac{g_s}{g_f} N N^2}\right) = C_{L_f} \tag{B.17}$$

$$C_{D_s} = C_{D_f} \tag{B.18}$$

The ratio of moment coefficients is obtained with Equation (B.19). Since a moment is defined as a force multiplied by a length and at the same time the chord length is introduced, both lengths cancel each other out. Therefore the moment coefficient ratio can be described with the same scaling factor as the lift coefficient which is 1 in this case.

$$C_{M_s} = C_{M_f} \left(\frac{M_s}{M_f}\right)\left(\frac{q_f S_f c_f}{q_s S_s c_s}\right) = C_{M_f} \tag{B.19}$$

B.4. MACH SCALING

A second scaling method that can be considered is where Mach similarity plays a key role. Wolowicz et al.[35] concludes that this method does not accurately model the dynamic stability and control derivatives that are sensitive to the angle of attack and aeroelastic effects. The starting equation is shown in Equation (B.20), expressed in flight velocity and speed of sound.

$$\begin{gathered} M_s = M_f \\ \left(\frac{V}{a}\right)_s = \left(\frac{V}{a}\right)_f \end{gathered} \tag{B.20}$$

B.4.1. VELOCITY

From Equation (B.20), a relationship between model and aircraft flight velocity can easily be established. This ratio is equal to the ratio of speed of sound (R_{V_s}), stated in Equation (B.21).

$$V_s = V_f \frac{a_s}{a_f} = V_f R_{V_s} \tag{B.21}$$

B.4.2. DYNAMIC PRESSURE

Equation (B.21) can then be used in the dynamic pressure equation. Equation (B.22) presents the Mach scaled relationship between both dynamic pressures.

$$q_s = q_f \frac{{}^1\!/\!_2 \rho_s V_s^2}{{}^1\!/\!_2 \rho_f V_f^2} = q_f \sigma R_{V_s}^2 \tag{B.22}$$

B.4.3. FROUDE NUMBER

In order to derive the scaling factor for Froude number, its definition is squared to get rid of the root for simplicity as can be seen in Equation (B.23). Ratios of velocity, gravitational acceleration, and geometry can then be inserted to obtain the scaling factor as shown.

$$Fr_s = Fr_f \frac{V_s^2}{g_s l_s} \frac{g_f l_f}{V_f^2} = Fr_f \left(\frac{M_s a_s}{M_f a_f}\right)^2 \frac{g_f}{g_s} \frac{1}{N} = Fr_f \frac{g_f}{g_s} R_{V_s}^2 \frac{1}{N} \tag{B.23}$$

B.4.4. REYNOLDS NUMBER

The relationship of Reynolds number between aircraft and its subscale model is shown in Equation (B.24). In comparison to the one obtained for Froude scaling, this relationship does not include the gravitational parameter but instead the ratio of speed of sound.

$$Re_s = Re_f \frac{V_s l_s}{\nu_s} \frac{\nu_f}{V_f l_f} = Re_f \frac{\nu_f}{\nu_s} R_{V_s} N \tag{B.24}$$

B.4.5. TIME

A similar approach as was shown in the previous section is used to determine the time scaling factor. By looking at the terms that correspond to the dimensions L, and LT^{-1}, the scaling ratio in Equation (B.25) is found.

$$t_s = t_f \frac{N}{R_{V_s}} \tag{B.25}$$

B.4.6. LIFT, DRAG, AND MOMENT COEFFICIENTS

Since Froude number dissimilarity is present in a Mach scaling approach, discrepancy in lift coefficient is seen between model and full-scale aircraft. Equation (B.26) shows the derivation of this scaling factor. Similarity in aerodynamic coefficients can be obtained however, when a specific combination of the parameters in the scaling term is selected. In general the ratio ${}^{g_s}/_{g_f}$ is 1, which means that equal lift coefficients is achieved when N is equal to $R_{V_s}^2$.

$$C_{L_s} = C_{L_f}\left(\frac{m_s g_s}{m_f g_f}\right)\left(\frac{q_f S_f}{q_s S_s}\right) = C_{L_f} N^3 \sigma \frac{g_s}{g_f}\frac{1}{\sigma R_{V_s}^2 N^2} = C_{L_f}\frac{N}{R_{V_s}^2}\frac{g_s}{g_f} \tag{B.26}$$

Likewise, the drag and moment coefficients are found as shown in Equation (B.27) and Equation (B.28) respectively.

$$C_{D_s} = C_{D_f}\frac{N}{R_{V_s}^2}\frac{g_s}{g_f} \tag{B.27}$$

$$C_{M_s} = C_{M_f}\frac{N}{R_{V_s}^2}\frac{g_s}{g_f} \tag{B.28}$$

B.5. Reynolds Scaling

The final option in aircraft similitude is Reynolds scaling. The relation that correspond to this scaling method is presented in Equation (B.29). The remaining section will again present the derivations of all the interesting parameters.

$$\begin{gathered} Re_s = Re_f \\ \left(\frac{Vl}{\nu}\right)_s = \left(\frac{Vl}{\nu}\right)_f \end{gathered} \tag{B.29}$$

B.5.1. Velocity

Since the velocity term is already present in the Reynolds number equation, a relationship between model and full-scale aircraft can readily be established shown in Equation (B.30).

$$V_s = V_f \frac{l_f}{l_s}\frac{\nu_s}{\nu_f} = V_f \frac{\nu_s}{\nu_f}\frac{1}{N} \tag{B.30}$$

B.5.2. Mach

Division of the velocity scaling factor by the speed of sound ratio results in the Mach scaling ratio as was also seen in the Froude scaling. The resulting equation relating both Mach numbers is shown below:

$$M_s = M_f \frac{V_s}{a_s}\frac{a_f}{V_f} = M_f \frac{\nu_s}{\nu_f}\frac{1}{N}\frac{1}{R_{V_s}} \tag{B.31}$$

B.5.3. Dynamic Pressure

The dynamic pressure is obtained in a similar fashion. Equation (B.32) provides the derivation of this quantity.

$$q_s = q_f \frac{{}^1/_2 \rho_s V_s^2}{{}^1/_2 \rho_f V_f^2} = q_f \sigma \left(\frac{\nu_s}{\nu_f}\right)^2 \frac{1}{N^2} \tag{B.32}$$

B.5.4. Froude Number

The gravitational acceleration is again introduced with the Froude number similarity. The ratio of Froude number between subscale model and full-scale counterpart is derived in Equation (B.33) in which the kinematic viscosity ratio has a squared influence and the geometric scaling factor has a cubed influence.

$$Fr_s = Fr_f \frac{V_s^2}{g_s l_s}\frac{g_f l_f}{V_f^2} = Fr_f \frac{g_f}{g_s}\frac{1}{N}\left(\frac{\nu_s}{\nu_f}\right)^2\frac{1}{N^2} = Fr_f \frac{g_f}{g_s}\left(\frac{\nu_s}{\nu_f}\right)^2\frac{1}{N^3} \tag{B.33}$$

B.5.5. Time

The geometric scaling factor N, divided by the velocity scaling factor obtained in Equation (B.30) results in the time relation shown in Equation (B.34).

$$t_s = t_f N^2 \frac{\nu_f}{\nu_s} \tag{B.34}$$

B.5.6. LIFT, DRAG, AND MOMENT COEFFICIENTS

Finally the lift, drag, and moment coefficient scaling factors can be obtained. This derivation can be found in Equation (B.35) - Equation (B.37). For the Reynolds scaling method it can again be concluded that a specific combination of the involved parameters can result in similarity of lift coefficients. The ratio of gravitational accelerations is again assumed to be unity. A subscale model implies that N is smaller than 1, thus the ratio of kinematic viscosity should be larger than 1 for equal lift and moment coefficients. This requirement can be met by flying the model at a different altitude or in an alternative medium.

$$C_{L_s} = C_{L_f}\left(\frac{m_s g_s}{m_f g_f}\right)\left(\frac{q_f S_f}{q_s S_s}\right) = C_{L_f} N^3 \sigma \frac{g_s}{g_f}\left(\frac{\nu_f}{\nu_s}\right)^2 N^2 \frac{1}{\sigma N^2} = C_{L_f} N^3 \frac{g_s}{g_f}\left(\frac{\nu_f}{\nu_s}\right)^2 \tag{B.35}$$

$$C_{M_s} = C_{M_f} N^3 \frac{g_s}{g_f}\left(\frac{\nu_f}{\nu_s}\right)^2 \tag{B.36}$$

$$C_{M_s} = C_{M_f} N^3 \frac{g_s}{g_f}\left(\frac{\nu_f}{\nu_s}\right)^2 \tag{B.37}$$

C

CLUSTER SETUP

Solving of the RANS/Euler equations by Fluent takes quite some time, especially when a large mesh is used such as the one for this study with over 30 million elements. A good convergence requires about 1500 to 2000 iterations, which comes down to about 2 days of computation time on a quad-core computer. Furthermore, each combination of angle of attack and elevator (vane) deflection has to be simulated. For example, if an AoA range of $-15° \leq \alpha \leq 15°$ is to be evaluated for a range of elevator deflections of $-21° \leq \delta \leq 21°$, this means that (with a step size of 3°) the number of required simulations can easily reach up to 11 x 15 = 165. Multiplying the amount of simulations by the time it takes for 1 simulation to converge, which was found to be 2 days, results in 11 months of computation time. This is obviously not feasible for this research, however the Delft University of Technology has a computation cluster available for these purposes.

This cluster consists of over 1500 cores, divided across 68 nodes. The operating system of the cluster is Linux, and all the nodes are linked to the so-called master computer, the HPC12. An overview of the node types and corresponding specifications can be seen in Table C.1. The CFD calculations can thus be performed with for example 48 cores instead of a typical quad-core desktop pc. This will decrease the computation time by roughly a factor 10. Moreover it is possible to submit multiple jobs to the cluster at the same time, which reduces the total computation time even further.

Type	**Number of nodes**	**Cores / node**	**Core speed w.r.t. typeD**	**Total cores**	**Total mem [GB]**	**CPU**	**Clockspeed [GHz]**
typeD	8	16	1.000000	128	512	AMD Opteron™ Processor 8354	2.2
typeE	12	8	2.069321	96	288	Intel® Xeon® CPU E5520	2.27
typeF	6	32	2.161804	192	768	AMD Opteron™ Processor 6136	2.4
typeG	10	48	0.979010	480	1920	AMD Opteron™ Processor 6234	2.4
typeH	12	20	3.523777	240	1536	Intel® Xeon® CPU E5-2670 v2	2.5
typeI	20	20		400	2560	Intel® Xeon® CPU E5-2660 v3	2.6
Total	68			1536	7584		

Table C.1: Delft University of Technology cluster specifications for the different nodes

Linux is based on a low-level assembly language, which is very time efficient because no resources are required for graphical interfaces as seen on a Microsoft Windows or macOS system. This also means that communication with the cluster has to be done in a command-line based manner. ANSYS products feature the capability to be configured and executed through command lines, using the MS-DOS command prompt window. Fluent is executed in a similar manner on the cluster by invoking an input file, consisting of all the commands that have to be performed.

An example input file can be seen in Figure C.1, in which 4 blocks are marked that show a typical input structure. First of all, a Fluent case file has to be created by the user (Section 4.3) after which it is uploaded to the cluster and imported via a simple *read-case* command. The second step is optional, if certain settings are desired to be changed in the case file. The example of Figure C.1 demonstrates how one of the boundary conditions can be altered as well as solver settings (pressure/momentum discretization schemes). This block can either be empty or stacked with commands, depending on the situation. Hereafter, the flow is initialized and the calculation is started by defining the amount of iterations. When convergence is obtained or the number of iterations is achieved, the data is stored to the location specified in the last block.

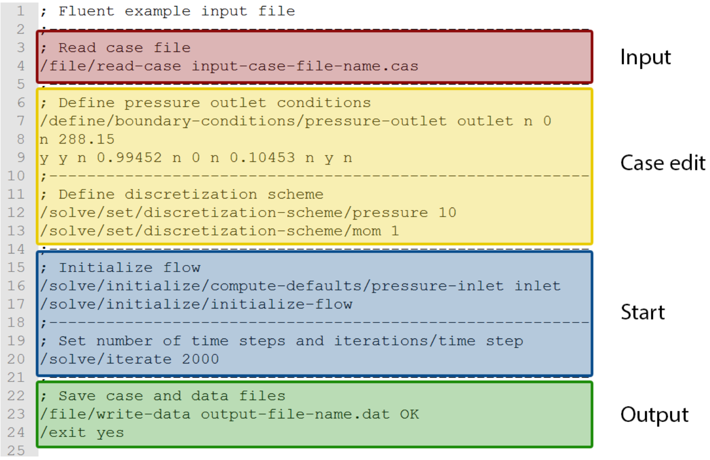

```
; Fluent example input file
;--------------------------------------------------------
; Read case file
/file/read-case input-case-file-name.cas
;--------------------------------------------------------
; Define pressure outlet conditions
/define/boundary-conditions/pressure-outlet outlet n 0
n 288.15
y y n 0.99452 n 0 n 0.10453 n y n
;--------------------------------------------------------
; Define discretization scheme
/solve/set/discretization-scheme/pressure 10
/solve/set/discretization-scheme/mom 1
;--------------------------------------------------------
; Initialize flow
/solve/initialize/compute-defaults/pressure-inlet inlet
/solve/initialize/initialize-flow
;--------------------------------------------------------
; Set number of time steps and iterations/time step
/solve/iterate 2000
;--------------------------------------------------------
; Save case and data files
/file/write-data output-file-name.dat OK
/exit yes

```

Figure C.1: Example input file to be invoked by ANSYS Fluent

In order to be able to communicate with the cluster, a pc has to be linked to the HPC12 by means of a Secure Shell (SSH). Through a simple user interface, files can be uploaded and downloaded to and from the server. Besides the input file described above, a Portable Batch System file (.pbs) has to be uploaded to the server. Technical inputs are described in this file, such as how many nodes and processors are to be allocated to the calculation. An example of such a script is presented in Figure C.2. In the SSH command window the whole process is started with the *qsub* command, submitting the job to the computation node.

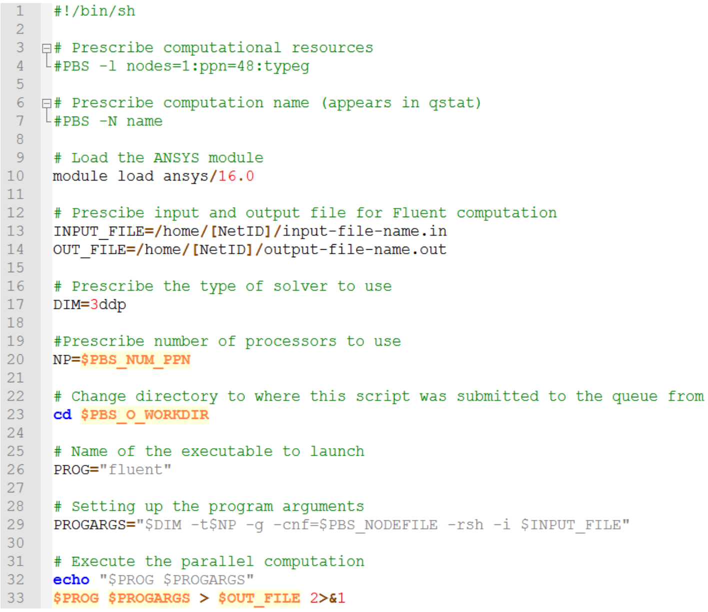

```
#!/bin/sh

# Prescribe computational resources
#PBS -l nodes=1:ppn=48:typeg

# Prescribe computation name (appears in qstat)
#PBS -N name

# Load the ANSYS module
module load ansys/16.0

# Prescibe input and output file for Fluent computation
INPUT_FILE=/home/[NetID]/input-file-name.in
OUT_FILE=/home/[NetID]/output-file-name.out

# Prescribe the type of solver to use
DIM=3ddp

#Prescribe number of processors to use
NP=$PBS_NUM_PPN

# Change directory to where this script was submitted to the queue from
cd $PBS_O_WORKDIR

# Name of the executable to launch
PROG="fluent"

# Setting up the program arguments
PROGARGS="$DIM -t$NP -g -cnf=$PBS_NODEFILE -rsh -i $INPUT_FILE"

# Execute the parallel computation
echo "$PROG $PROGARGS"
$PROG $PROGARGS > $OUT_FILE 2>&1
```

Figure C.2: Example .pbs file that instructs the HPC12 to execute ANSYS Fluent

D

MESHING TERMINOLOGY

The purpose of a mesh is to split the computational domain of the model into a large amount of smaller volumes. The Euler equations can then be solved in a discretized fashion.

D.1. GENERAL

Three types of meshes can be created: structured, unstructured, and hybrid. The basic cell geometries that are used for 3D meshing are drawn in Figure D.1.

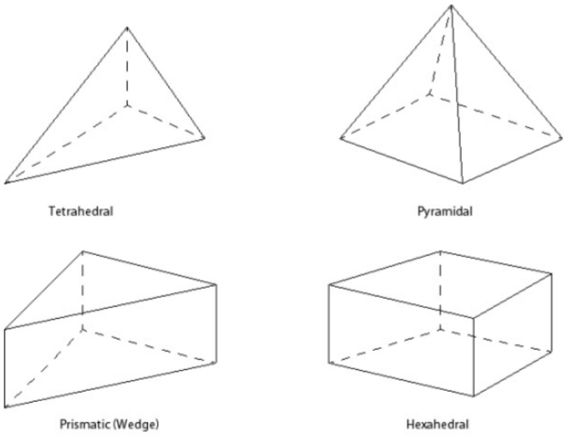

Figure D.1: Typical 3D mesh elements[36]

Structured mesh

This type of mesh is the most accurate of the three, however it also requires a lot of time to create such a mesh in case of complex geometries. A structured mesh uses quadrilateral elements for 2D models, which are transformed into hexahedral elements in 3D models as can be seen in Figure D.2. Because of the conformal structure, two adjacent points in the real space correspond to two adjacent points in the computational space. This enables fast accessing of the cells by using indices. The quadrilateral / hexahedral structure also requires less cells in comparison to triangular / tetrahedral to fill the same area or volume. Memory usage is therefore more efficient, which can for example be used for local refinement in area's of interest (e.g. the boundary layer).

Unstructured mesh

Figure D.3 shows an unstructured mesh around an airfoil, with local refinement around the leading and trailing edges. Unstructured meshes generally consist of triangular elements in 2D, and tetrahedral / prismatic elements in 3D. Complex models can easily be meshed automatically with this type of mesh, however on cost of prediction accuracy. Furthermore, a larger number of cells are required in comparison to the structured type mesh to obtain the requirement mesh refinement. This increases the time required to solve the Navier-Stokes equations.

Hybrid mesh

It is also possible to combine the accuracy of a structured mesh with the rapid automated grid generation of an unstructured mesh. Such a hybrid structure can be seen around an airfoil with a high lift device in Figure D.4. Hexahedral elements are used to accurately capture complex flows in for example the boundary layer, where a combination of tetrahedral, prismatic, and pyramidal elements are used to discretize the rest of the computational domain.

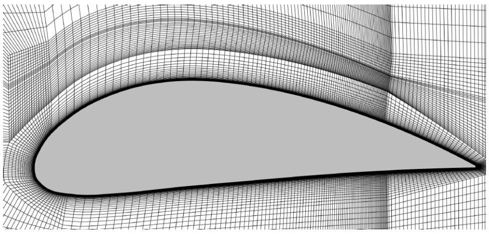

Figure D.2: Structured mesh around a 2D airfoil[37]

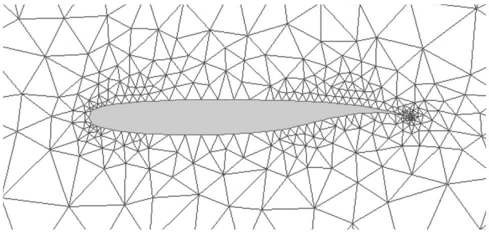

Figure D.3: Unstructured mesh around a 2D supercritical airfoil [37]

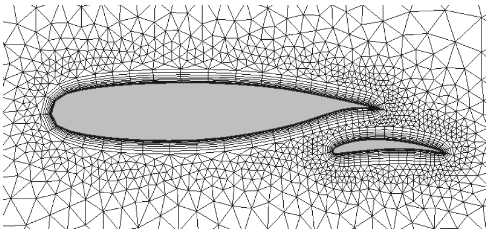

Figure D.4: Hybrid mesh consisting of quadrilateral elements in the boundary layer area and triangular elements which extend the mesh into the far field[37]

The ducted fan on the DUUC features complex geometries, which requires a good mesh quality to accurately predict the flow behavior in that vicinity. The mesh module in ANSYS is capable of automatically creating an unstructured mesh in the provided computational domain. Therefore, hybrid meshes are used in this study.

D.2. MESH QUALITY

An important aspect of the generated mesh is its quality, which can be expressed in several terms. This quality is needed to minimize solution errors and to ensure faster convergence. Table D.1 shows an overview of the different qualitative parameters, which will be discussed below.

Element quality

This metric defines the ratio of the element volume to the sum of its edge lengths. A value of 1 indicates a perfect element, whereas 0 means that the volume of the element is either zero or negative. The element quality is obtained using Equation (D.1), where C varies depending on the element type according to Table D.2.

$$Quality = C\left(\frac{\text{cell volume}}{\sqrt{\left(\sum\left(\text{edge length}\right)^2\right)^3}}\right) \tag{D.1}$$

Skewness

ANSYS uses the skewness parameter as default measure for the mesh quality. Skewness can be measured by two methods: equilateral-volume-based and normalized-equiangular-based. The first method

Parameter	**Good**	**Poor**
Skewness	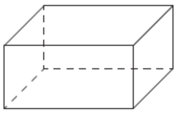	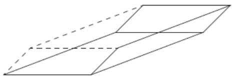
Orthogonality	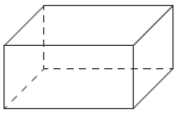	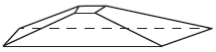
Smoothness	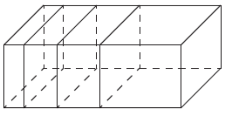	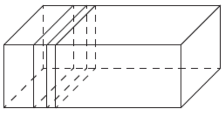
Aspect ratio	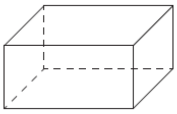	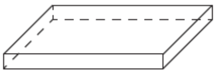
Positive cells	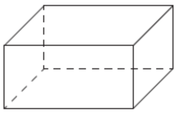	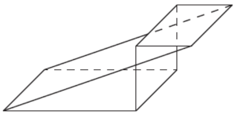
Boundary layer	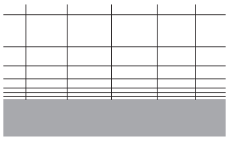	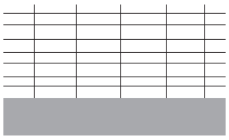

Table D.1: Mesh quality considerations

applies to tetrahedral cells only, whereas the second one can be used on all cell geometries. Since the unstructured grid around the DUUC will mostly be tetrahedral, the first method will briefly be explained. Equation (D.2) is used by ANSYS to quantify the skewness of each cell in the range of 0-1, where 0 indicates an equilateral cell (i.e. best quality).

$$Skewness = \frac{\text{Optimal cell size} - \text{Actual cell size}}{\text{Optimal cell size}} \tag{D.2}$$

The optimal cell size is obtained by measuring the volume of an equilateral tetrahedron with the same circumcircle as the actual cell, visualized in Figure D.5. ANSYS defines the following cell quality categories:

Skewness	0	>0 - 0.25	0.25 - 0.5	0.5 - 0.75	0.75 - 0.9	0.9 - <1	1
Quality	equilateral	excellent	good	fair	poor	bad	degenerate

Orthogonality

This quantity is determined by measuring the angles between several sets of vectors, which should ideally be parallel (i.e. non-orthogonal). The vectors of interest are the face normal vectors, the vectors connecting the centroid with the centroids of adjacent cells, and the vectors from the centroid of the cell to the centers of the cell's faces. These vectors are illustrated in Figure D.6.

In vector algebra, the dot product of two vectors is defined as the magnitudes of these vectors multi-

Element type	**C**
Triangle	6.92820323
Quadrangle	4.0
Tetrahedron	124.70765802
Hexagon	41.56921938
Wedge	62.35382905
Pyramid	96.0

Table D.2: Constant value of C used for the element quality metric

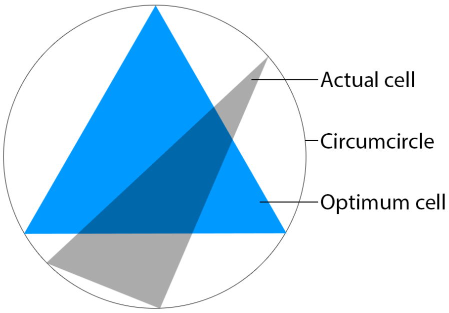

Figure D.5: Optimum equilateral cell geometry

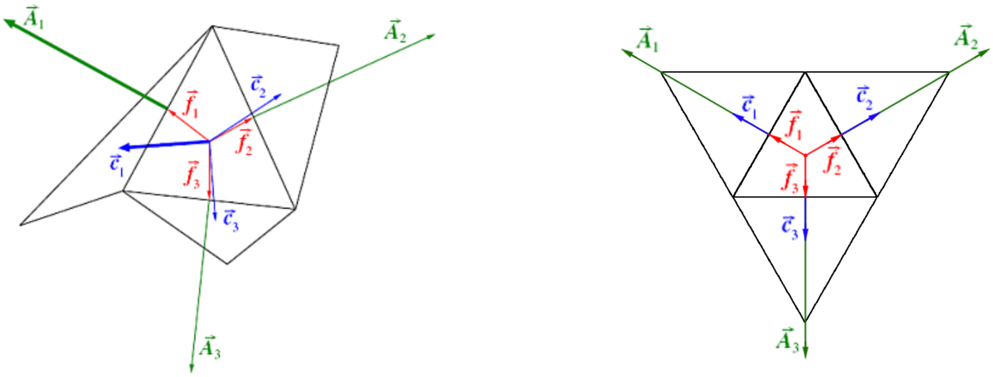

Figure D.6: Definition of the vectors used to measure cell orthogonality

plied by the angle between them. These angles are of interest in order to be able to say something about the orthogonal quality of the cells. For an equilateral case, the angles between f_i and A_i are zero as well as the angles between c_i and A_i as can be seen on the right in Figure D.6. ANSYS determines all angles and defines the orthogonality of a cell by Equation (D.3). Orthogonal quality ranges from 0 to 1, with 1 indicating an equilateral mesh:

Orthogonality	0	>0 - 0.15	0.15 - 0.2	0.2 - 0.7	0.7 - 0.95	0.95 - <1	1
Quality	degenerate	bad	poor	fair	good	excellent	equilateral

$$orthogonality = \min\left(\frac{\vec{A}_i \cdot \vec{f}_i}{|\vec{A}_i| \cdot |\vec{f}_i|}, \frac{\vec{A}_i \cdot \vec{c}_i}{|\vec{A}_i| \cdot |\vec{c}_i|}\right) \tag{D.3}$$

Smoothness

It is important to have a gradual change in size between adjacent cells. If this change is too abrupt, the computation will be erroneous because the differential equations that are solved assume smoothness and continuity in cell growth. An example of a good and poor smoothness is shown in Table D.1. ANSYS recommends a volume expansion ratio between 1 and 1.5.

Aspect ratio

Aspect ratio is defined as the ratio of the longest edge length to the shortest edge length, which is equal to 1 in an equilateral case. Especially in the regions with high transverse gradients (e.g. boundary layer), the aspect ratio of the cells should be minimized.

Positive cells

When prismatic and/or hexahedral elements are being used in the mesh, it is possible for those cells to have a negative volume. An example of such a hexahedron is shown in Table D.1. Solving the equations in a mesh containing such negative cells can result in behavior that is physically not possible.

Boundary layer

The boundary layer is a region in which a lot of flow phenomena may happen, which requires a sufficient fine grid to ensure an accurate prediction. In Table D.1 it can be seen what such a mesh looks like close to a wall. The near-wall grid element size can be calculated by using the dimensionless wall distance, called y-plus (y^+). This principle is explained in Appendix D.3.

D.3. BOUNDARY LAYER MODELING

The boundary layer can be divided into an inner and outer layer, of which the former is again build up from three layers: the viscous sublayer, buffer layer, and log-layer. These sublayers are shown in Figure D.7, along with the velocity profile in the boundary layer. The free stream velocity is denoted by U_0 and the boundary layer thickness is called δ. According to the law of the wall (Equation (D.4)), the velocity profile in the boundary layer can be written as a function of the non-dimensional wall distance (y^+):

$$U^+ = f(y^+) \tag{D.4}$$

where the non-dimensional velocity U^+ and wall distance y^+ are defined as:

$$U^+ \equiv \frac{U}{U_\tau} \quad \text{and} \quad y^+ \equiv \frac{U_\tau y}{\nu} \tag{D.5}$$

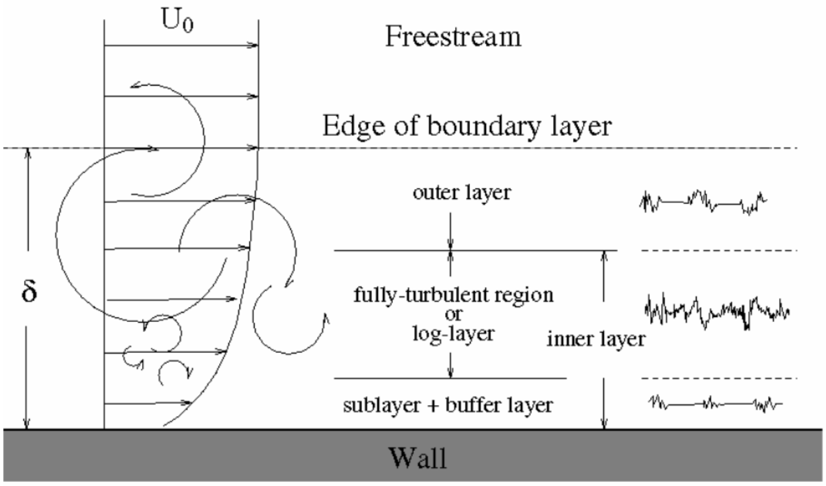

Figure D.7: Different layers in the turbulent boundary layer[38]

The layers that defined the boundary layer in Figure D.7 are based on this y^+ value. The viscous sublayer is the region where $y^+ \leq 5$ and the log-law region is defined as $y^+ \geq 30$ as long as $\frac{y}{\delta} < 0.3$. The region between these two layers is the buffer layer as shown in Figure D.8. From this figure it can be observed that in the viscous sublayer the velocity can be approximated with $U^+ = y^+$. On the other hand, in the log-law layer the logarithmic relationship applies as an accurate representation. Furthermore it can be seen that neither of the two approximations hold in the buffer region. Therefore a proper near-wall treatment should be applied when constructing a grid that represents the boundary layer. The $k-\omega$ turbulence model in ANSYS FLUENT makes use of two methods depending on the mesh size: *two-layer modeling* is used when the mesh near the wall is fine enough, while *wall functions* are used otherwise. However, how does FLUENT know when a mesh is "fine enough"? Here the y^+ value comes in, which is calculated by using the thickness of the first inflation layer (Δy_1). The relationship between this layer thickness and the y^+ value is shown in Equation (D.6):

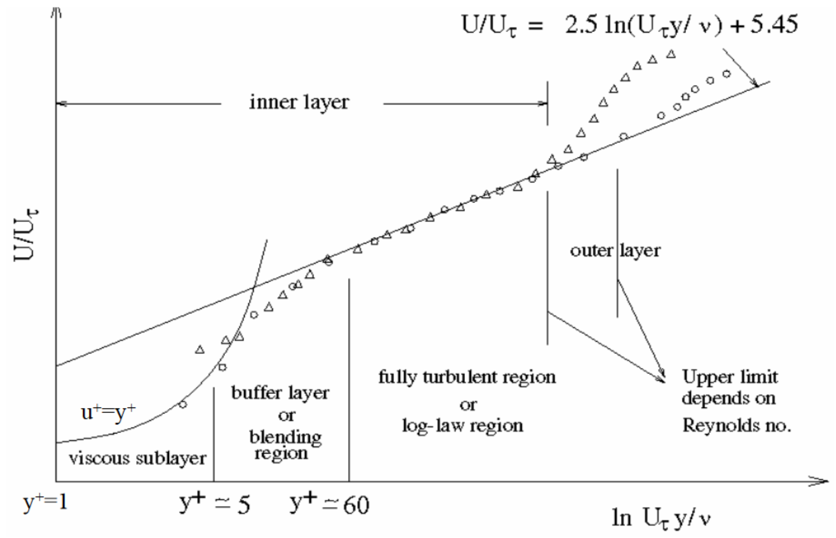

Figure D.8: Different layers in the turbulent boundary layer[38]

$$\Delta y_1 = \frac{y^+ \mu}{\rho U_\tau} \tag{D.6}$$

where U_τ represents the frictional velocity that can be written in terms of wall shear stress (τ_w) and the fluid density as shown in Equation (D.7).

$$U_\tau = \sqrt{\frac{\tau_w}{\rho}} \tag{D.7}$$

The wall shear stress is obtained from the friction coefficient:

$$\tau_w = {}^1\!/\!_2 C_f \rho U^2 \tag{D.8}$$

There are many approximation models that relate the friction coefficient with the Reynolds number for turbulent boundary layers. Hoerner[39] states the most important ones and mentions the Schoenherr curve as a valid approximation for the skin friction coefficient at a wide range of Reynolds numbers as can be seen in Figure D.9. An approximation for the Schoenherr line within ±2% is given in Equation (D.9).

$$C_f = (3.46 \log Re - 5.6)^{-2} \tag{D.9}$$

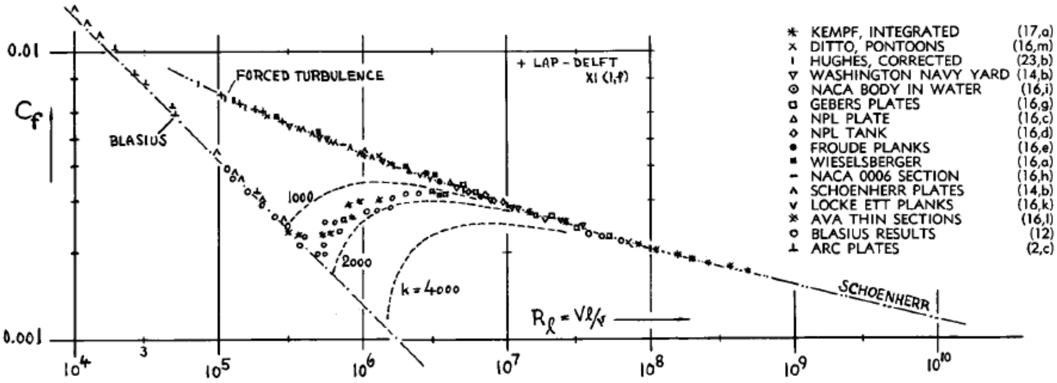

Figure D.9: Skin friction coefficient as function of Reynolds number[39]

E

Sizes and Results of the Meshes Used in Mesh Convergence Study

For both the full-scale and subscale mesh convergence studies, six meshes are generated with increasing mesh density. A detailed description of the surface and volume sizing settings is provided in this section. The grid independence study is performed at an angle of attack of zero degrees with no vane deflection, for which the resulting lift and drag data is provided as well. Appendix E.1 discusses the full-scale meshes that were used and Appendix E.2 lists the subscale convergence study results.

E.1. Full-scale

The six meshes, denoted by **Mesh F1** - **Mesh F6**, are related to each other by a certain scaling factor for the element sizes. These settings are listed in Table E.1 where **Mesh F3** is selected as a baseline. Each sizing is then scaled by for example 1.5, resulting in **Mesh F2**. The settings listed in Table E.2 are constants and are kept the same for each mesh configuration.

		Mesh F1	**Mesh F2**	**Mesh F3**	**Mesh F4**	**Mesh F5**	**Mesh F6**
Default settings	Minimum size	0.01125	0.0075	0.005	0.00417	0.00370	0.00333
	Maximum face size	6.75	4.5	3	2.5	2.22222	2
	Maximum size	6.75	4.5	3	2.5	2.22222	2
Volume sizing	Outer domain	6.75	4.5	3	2.5	2.22222	2
	Inner domain	0.3375	0.225	0.15	0.125	0.11111	0.1
Face sizing	Horizontal vane	0.0675	0.045	0.03	0.025	0.02222	0.02
	Vertical vane	0.0675	0.045	0.03	0.025	0.02222	0.02
	Duct	0.23625	0.1575	0.105	0.0875	0.07778	0.07
	Center body	0.10125	0.0675	0.045	0.0375	0.03333	0.03
	Pylon	0.10125	0.0675	0.045	0.0375	0.03333	0.03
	Fuselage	0.3375	0.225	0.15	0.125	0.11111	0.1
	Wing	0.3375	0.1125	0.075	0.0625	0.05556	0.05
	Actuator disk	0.0675	0.045	0.03	0.025	0.02222	0.02

Table E.1: Mesh sizing settings used for the mesh convergence study (all units are in m)

The number of total elements that are obtained for these mesh settings are within 20 to 39 million, for which the lift and drag coefficients can be found in Table E.4 and Table E.5 respectively. For the lift coefficients, the reference area of the corresponding lifting surface is selected, whereas the drag is scaled by the wing area. These quantities are shown in Table E.3 for both the full-scale and 5.5% subscale case. Note that these areas should by doubled to obtain the aerodynamic forces of the complete aircraft, since the CFD model consists of only half of the DUUC.

	TE sizing (f / s)	**Inflation (full-scale / subscale)**		
	Element size $[m]$	First layer height $[m]$	Maximum layers	Growth rate
Horizontal vane	0.0025 / 0.0001375	0.00025 / 0.00071	20 / 20	1.25 / 1.25
Vertical vane	0.0025 / 0.0001375	0.00025 / 0.00071	20 / 20	1.25 / 1.25
Duct	0.0025 / 0.0001375	0.00025 / 0.00071	20 / 20	1.25 / 1.25
Pylon	0.0025 / 0.0001375	0.00025 / 0.00071	20 / 20	1.25 / 1.25
Center body	- / -	0.00025 / 0.00071	20 / 20	1.25 / 1.25
Fuselage	0.1 / 0.0055	0.0005 / 0.00141	10 / 10	1.35 / 1.35
Wing	0.005 / 0.000275	0.0005 / 0.00141	10 / 10	1.35 / 1.35

Table E.2: Mesh constants used for the mesh convergence study

Component	**Reference area** $[m^2]$	
	Full-scale	**Subscale**
Horizontal vane	2.7475	0.0083
Duct	10.6812	0.0323
Pylon	1.1973	0.0036
Wing	51.76	0.1566

Table E.3: Reference areas used in the mesh convergence study

E.2. Subscale

The mesh settings of the subscale meshes are shown in Table E.6. Note that the units are in mm and not m as was the case for the full-scale meshes. Due to the lower airspeed at which the scale model is analyzed, the flow is easier to predict and mesh convergence is obtained with lower elements w.r.t. the full-scale case. This number of elements ranges from about 14 to 32 million as can be seen in Table E.7. The lift coefficients are also listed in this table. Table E.8 summarizes the pressure drag coefficients of the subscale meshes.

	Mesh F1	**Mesh F2**	**Mesh F3**	**Mesh F4**	**Mesh F5**	**Mesh F6**
N	20,246,701	22,296,827	27,051,305	31,037,714	34,722,260	38,830,864
$C_{L_{vane_h}}$	0.5669	0.5761	0.5792	0.5774	0.5790	0.5783
$C_{L_{duct}}$	-0.2361	-0.2436	-0.2354	-0.2330	-0.2321	-0.2313
$C_{L_{pylon}}$	-0.0931	-0.0858	-0.0699	-0.0677	-0.0686	-0.0669
$C_{L_{wing}}$	0.1171	0.1516	0.1750	0.1746	0.1745	0.1719

Table E.4: Lift coefficients for different mesh densities

	Mesh F1	**Mesh F2**	**Mesh F3**	**Mesh F4**	**Mesh F5**	**Mesh F6**
N	20,246,701	22,296,827	27,051,305	31,037,714	34,722,260	38,830,864
$C_{D_{vane_h}}$ x10^{-3}	0.4947	0.4161	0.4051	0.4032	0.3943	0.3971
$C_{D_{duct}}$	-0.0116	-0.0117	-0.0117	-0.0117	-0.0118	-0.0118
$C_{D_{pylon}}$ x10^{-3}	-0.3949	-0.3871	-0.3669	-0.3658	-0.3691	-0.3674
$C_{D_{wing}}$	0.0040	0.0039	0.0036	0.0034	0.0033	0.0032
$C_{D_{cb}}$	-0.0043	-0.0044	-0.0045	-0.0045	-0.0046	-0.0046
$C_{D_{vane_v}}$ x10^{-3}	-0.4563	-0.5037	-0.5113	-0.5199	-0.5235	-0.5260
$C_{D_{fuselage}}$	0.0044	0.0036	0.0031	0.0030	0.0029	0.0029
$C_{D_{total}}$	-0.0079	-0.0091	-0.0100	-0.0104	-0.0106	-0.0108

Table E.5: Pressure drag coefficients for different mesh densities

		Mesh S1	**Mesh S2**	**Mesh S3**	**Mesh S4**	**Mesh S5**	**Mesh S6**
Default settings	Minimum size	0.6875	0.415	0.33	0.18425	0.143	0.12375
	Maximum face size	412.5	247.5	198	110.55	85.8	74.25
	Maximum size	412.5	247.5	198	110.55	85.8	74.25
Volume sizing	Outer domain	412.5	247.5	198	110.55	85.8	74.25
	Inner domain	30.9375	18.5625	14.85	8.29125	6.435	5.56875
Face sizing	Horizontal vane	4.125	2.475	1.98	1.1055	0.858	0.7425
	Vertical vane	4.125	2.475	1.98	1.1055	0.858	0.7425
	Duct	14.4375	8.6625	6.93	3.86925	3.003	2.59875
	Center body	6.1875	3.7125	2.97	1.65825	1.287	1.11375
	Pylon	6.1875	3.7125	2.97	1.65825	1.287	1.11375
	Fuselage	20.625	12.375	9.9	5.5275	4.29	3.7125
	Wing	10.3125	6.1875	4.95	2.76375	2.145	1.85625
	Actuator disk	4.125	2.475	1.98	1.1055	0.858	0.7425

Table E.6: Mesh sizing settings used for the mesh convergence study of the subscale model (all units are in mm)

	Mesh S1	**Mesh S2**	**Mesh S3**	**Mesh S4**	**Mesh S5**	**Mesh S6**
N	13,878,272	14,735,094	15,391,603	20,456,759	26,311,589	31,670,024
$C_{L_{vane_h}}$	-0.0163	-0.0235	-0.0254	-0.0268	-0.0272	-0.0270
$C_{L_{duct}}$	-0.1371	-0.1465	-0.1520	-0.1575	-0.1573	-0.1561
$C_{L_{pylon}}$	-0.0673	-0.0876	-0.0967	-0.0991	-0.0998	-0.0985
$C_{L_{wing}}$	0.0730	0.0890	0.1020	0.1336	0.1434	0.1466

Table E.7: Lift coefficients for different mesh densities of the subscale model

	Mesh S1	**Mesh S2**	**Mesh S3**	**Mesh S4**	**Mesh S5**	**Mesh S6**
N	13,878,272	14,735,094	15,391,603	20,456,759	26,311,589	31,670,024
$C_{D_{vane_h}}$ x10^{-3}	0.1090	-0.0676	-0.0753	-0.0998	-0.1281	-0.1564
$C_{D_{duct}}$	-0.0080	-0.0084	-0.0085	-0.0086	-0.0086	-0.0086
$C_{D_{pylon}}$ x10^{-3}	-0.2864	-0.3385	-0.3605	-0.3672	-0.3709	-0.3700
$C_{D_{wing}}$	0.0069	0.0064	0.0061	0.0053	0.0050	0.0048
$C_{D_{cb}}$	-0.0038	-0.0039	-0.0040	-0.0041	-0.0041	-0.0041
$C_{D_{vane_v}}$ x10^{-3}	0.0701	-0.0900	-0.0935	-0.1193	-0.1463	-0.1746
$C_{D_{fuselage}}$	0.0042	0.0036	0.0035	0.0032	0.0031	0.0031
$C_{D_{total}}$	-0.0007	-0.0028	-0.0034	-0.0047	-0.0053	-0.0056

Table E.8: Pressure drag coefficients for different mesh densities of the subscale model